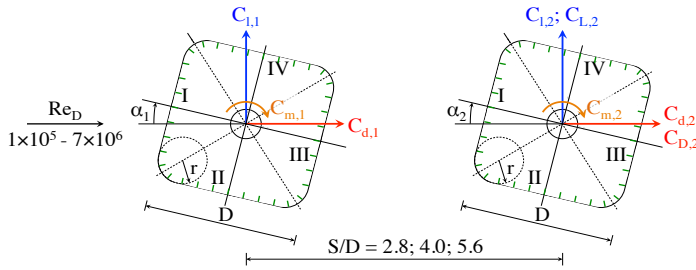


Graphical Abstract

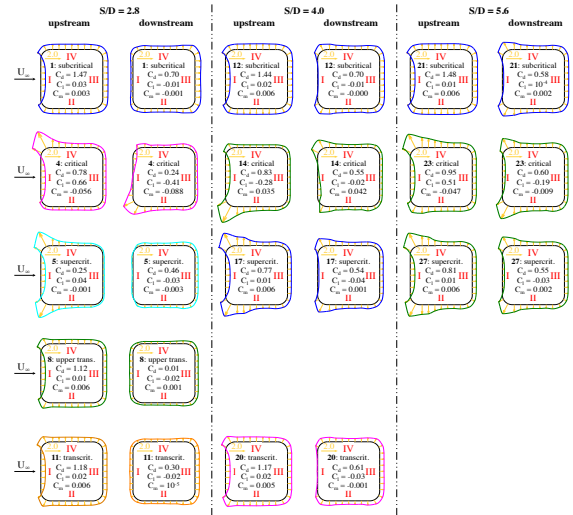
Two identical tandem square prisms with rounded edges and hard marine fouling at incidence in cross-flow: effect of spacing and Reynolds number on unsteady fluid dynamics

Nils Paul van Hinsberg



For $\alpha = 0^\circ$ and 45° at $S/D = 2.8, 4.0,$ and 5.6 :

- Two inline square-section prisms with edge roundness of $r/D = 0.16$
 - Mean sectional drag, lift, and pitch moment on both prisms
 - Mean and fluctuating global drag and lift on downstream prism
- Frequency and strength of shed vortices in wake of downstream prism
 - Mean sectional surface pressures on both prisms



Highlights

Two identical tandem square prisms with rounded edges and hard marine fouling at incidence in cross-flow: effect of spacing and Reynolds number on unsteady fluid dynamics

Nils Paul van Hinsberg

- Experiments on unsteady loading on two tandem square prisms with rounded edges
- Extensive analysis of forces, vortex shedding, and surface pressure at $\alpha=0^\circ$ and 45°
- Large mutual interference at centre-to-centre spacing values of $S/D=2.8$ and 4
- Thrust force on second prism, low vortex strength and Strouhal number for $S/D=2.8$
- Reynolds-number independency and highest lift fluctuations at $S/D=5.6$ and $\alpha=45^\circ$

Two identical tandem square prisms with rounded edges and hard marine fouling at incidence in cross-flow: effect of spacing and Reynolds number on unsteady fluid dynamics

Nils Paul van Hinsberg^{a,*},¹ (Researcher)

^aInstitute of Aeroelasticity, German Aerospace Center, Bunsenstrasse 10, 37073 Göttingen, Germany

ARTICLE INFO

Keywords:

tandem rounded square prism
marine fouling
high Reynolds number
interference effect
negative drag
unsteady force


ABSTRACT

Because of their long submerged columns, deep-draft semi-submersible floating structures are particularly susceptible to vortex-induced motions. This paper focuses on the steady and unsteady forces that act on such a column pair, as well as on the frequency and strength of the shed vortices behind the downstream column. Wind tunnel experiments were performed on two rounded and lightly rough square-section prisms in cross-flow for Reynolds numbers from 100,000 up to 7 million. They are arranged inline at centre-to-centre distances of $S/D = 2.8, 4,$ and 5.6 and at 0° or 45° incidence angle. The trend of the drag curve for the upstream prism deviates at $S/D = 2.8$ and 4 sharply from that for a single prism. The drag force on the downstream prism strongly depends on both S/D and α . At $S/D = 2.8$, a thrust force occurs either in certain ($\alpha = 0^\circ$) or in all ($\alpha = 45^\circ$) flow states. Larger spacing values lead to an overall higher drag and a flattening of the $C_{d2}(Re_D)$ curve. The highest fluctuating lift forces on the downstream prism are obtained at $\alpha = 45^\circ$. Regarding the vortex shedding frequency, differences between both incidence angles occur at $S/D = 5.6$ only.

1. Introduction

Isolated streamlined bodies (e.g. a rotor blade of a wind turbine, an aero- or hydrofoil) or bluff bodies (like, for example, a prismatic or a circular structure) can undergo fluid-structure interactions when mounted elastically in a uniform flow. The resultant fluctuating pressure forces experienced by the element can be of considerable magnitude, as a result of which the structure can experience different types of flow-induced vibration, e.g. vortex-induced vibrations (VIV, characterised by a high frequency and a limited amplitude), flow interference, turbulence-induced vibrations (hence, buffeting), galloping (a motion-induced vibration at a low frequency and no limitation in its amplitude), static divergence, and flutter (Moe and Henriksen, 1999; Blevins, 2006). When placing another body or multiple bodies in its vicinity within the flow field the fluid-dynamic interference between those bodies may induce an altering of the fluctuating surface pressures that act on them, of the resultant time-mean and fluctuating lift and drag forces and fluid-dynamic moments, as well as of the flow structures both around the bodies and in their separate or common wake. These changes in the flow characteristics lead to modifications in the induced vibrations associated with the flow around two or more streamlined or bluff structures, such as shear-layer impingement and reattachment, quasiperiodic vortices, wake galloping, VIV, or resonance.

*Corresponding author

 nils.vanhinsberg@dlr.de (N.P. van Hinsberg)

 <https://www.dlr.de/ae/en/desktopdefault.aspx/tabid-9763/>

16748_read-65853/, nils.vanhinsberg@dlr.de (N.P. van Hinsberg)

ORCID(s): 0000-0001-7411-333X (N.P. van Hinsberg)

1.1. VIM of multi-column deep-draft floating structures

Multiple cylindrical or prismatic structures are widely encountered in many practical situations such as chimney stacks, overhead power-line bundles, bridge pylons and decks, tube bundles in heat exchangers, skyscrapers in modern cities, pipelines, risers, and fixed and floating offshore wind turbines. In particular floating offshore structures can experience a large drift in the same order of magnitude as that of the transversal cross-sectional dimension of the structure. Since this drift occurs at low frequencies close to the transverse eigenfrequency of the structure, we speak in this case from vortex-induced motions (VIM), a particular case of VIV. This large structural motion can reflect in large maximum and low minimum tendon forces on the mooring lines, which may result in a considerable reduction of their fatigue life (Huang et al., 2003; Cheng et al., 2011). Research on VIM of multi-column, semi-submersible structures, such as deep-draft semi-submersible platforms, wind turbines, and TLPs, is still quite recent. For these floating structures, VIM was only noticed due to an upscaling in the dimensions of their columns, i.e. an increase of their draft, to improve the platform's heave motion performance. Because of their long submerged columns and large projected area to the current – hence, a large effective excitation length – these deep-draft offshore constructions are particularly susceptible to in-line drag forces and transverse vortex-induced lift forces. The large mean and fluctuating forces in flow- and cross-flow direction may induce considerable pitch, sway, and/or yaw motions of the complete construction. Through field measurements on deep-draft semi-submersibles Rijken and Leverette (2009) and Ma et al. (2013) observed the occurrence of VIM on this kind of floating structures. Waals et al. (2007) conducted model

tests in a towing tank to examine the effect of draft and mass ratio on the VIM behaviour of two kinds of multi-column floaters, i.e. a semi-submersible and a TLP. Their results showed that the largest motions occurred at a towing direction of 45 degrees, as a result of which an increased drag coefficient was measured. They furthermore found that the amount of column immersion influenced the magnitude of VIM response of the complete structure. Gonçalves et al. (2011, 2012b,c, 2013) conducted multiple test series to study the effect of the current incidence angle, surface waves, external damping level, hull appendages, and draft conditions on the VIM response of a semi-submersible platform with four columns having square cross sections and sharp edges. They found not only that the VIM behaviour is strongly influenced by the aspect ratio H/L (H and L being the immersed length and the width of each column, respectively), but also that for current incidences of 30 degrees and 45 degrees the largest transverse amplitudes are about 40% of the column width, whereas the largest yaw motions occur at 0 degrees current incidence.

1.2. Influence of columns' cross-sectional shapes on VIM of multi-column deep-draft floating structures

With the constant further scientific development of deep-draft multi-column floating platforms and wind turbines, the focus of numerical and experimental studies has, among others, transferred to the effect of the columns' geometric parameters on the VIM response of the structure as well (e.g. Rijken (2014); Gonçalves et al. (2015); Chen and Chen (2016); Liu et al. (2017); Li et al. (2018)). At present, the cross-sectional shapes of the columns are either circular, squared with sharp edges, or a combination of both extremes, hence squared with rounded edges. Among these three possible cross-sections, the squared-section columns with rounded edges and in particular the impact of the edge roundness on the VIM behaviour of floating structures have been the least investigated to date. Rijken (2014) performed numerical simulations to study the effect of the column shape (square, rectangular, and five-sided) on the VIM response of a semi-submersible platform. His results showed that the occurrence of VIM is independent of the selected cross section and is the result of the pressure forces that act on the immersed section of each column. Chen and Chen (2016) carried out numerical simulations on a semi-submersible with four square columns with various values of edge roundness. The floating platform was subjected to a current with an impact angle of 45 degrees and its elastic mounting allowed surge, sway, and yaw motions. They observed not only that their deep-draft semi-submersible with rounded square columns experiences larger sway motions than its counterpart with sharp edges, but also that the maximum amplitude in sway increases for larger edge roundness values. Towing tank measurements on two different elastically mounted, four-column deep-draft semi-submersibles have been conducted by Gonçalves et al. (2015) to investigate the effect of two types of columns, i.e. ei-

ther with a circular or with a rounded square cross section. Three angle of incidences with respect to the oncoming current were tested for each model, namely 0, 22.5 and 45 degrees, at reduced velocities between $U_r = 4$ and 25, corresponding to a Reynolds-number range of 7,000 up to 80,000. They found that whereas the maximum VIM amplitude in transverse direction – the sway motion – was highly independent of the column's cross section, the incidence angle of the platform at which these maximum amplitudes occurred changed from 0 degree for the platform with cylindrical columns to 45 degrees for the one with rounded square columns. Concerning the yaw motions of the floating structure, a continuous increase in amplitude, independent of the heading, was found for the semi-submersible with rounded square columns, whereas for its counterpart with cylindrical columns a maximum was measured for 22.5 and 45 degrees around $U_r = 8$.

A quite recent numerical study by Liu et al. (2017) focussed on the VIM performance of various four-column semi-submersibles with different edge roundness values for both the columns and the pontoon. They pointed out that whereas for the floating platforms with circular or sharp-edged square columns the largest transverse amplitudes occur at a current heading of 0 degrees, the semi-submersible with rounded square columns experiences more significant transverse motions at 45 degrees current heading. The latter motions furthermore show a rapid increase with larger column edge roundness in the range of $r/D < 0.1$ (with r and D the dimensional edge roundness and the width of the column, respectively), a roughly constant peak value for $0.1 \leq r/D \leq 0.2$, and a decreasing trend with increasing r/D -value for $r/D > 0.3$. They attributed this VIM behaviour to the influence of the column edge roundness on the boundary-layer separation points on the columns' surfaces and the strength of the shed vortices (hence, the resultant fluctuating lift forces), both of which induce changes in the flow field characteristics. These trends of the sway motion with varying column edge roundness were later confirmed in a numerical study by Li et al. (2018) for a deep-draft semi-submersible at 45 degrees current heading. They observed that transverse amplitudes of the floating platform increase for larger r/D -values in the range of $0 \leq r/D \leq 0.5$, whereas the largest non-dimensional sway amplitude of $A_y/D \approx 0.46$ occurs when using cylindrical columns.

1.3. Two square-section prisms with finite edge roundness arranged in tandem

With the exception of possible "exotic" designs, the columns of multi-column (deep-draft) semi-submersible structures and wind turbines are generally arranged in (combinations of) tandem, side-by-side, or staggered pairs. Similarities between the VIM behaviour of such floating platforms and that of (small) groups of cylinders or prisms tangent to the flow or in cross-flow are thus to be expected. As has been mentioned before, deep-draft floating offshore constructions are particularly susceptible to in-line drag forces and trans-

verse vortex-induced lift forces, whereby the maximum amplitude in sway – induced by the alternating out of plane pressure changes on both side surfaces of each foundation column as a result of the periodic vortex shedding in its wake – increases with increased column's edge roundness. A robust prediction modelling of the structural response to (highly) unsteady flows is challenging though, as Pesce et al. (2021) nicely pointed out: "*VIM is a complex phenomenon that requires nonlinear dynamic models to be constructed and simulated, either through highly computationally demanding CFD approaches or by making use of reduced-order models (ROM) based on phenomenological schemes to emulate the vortex wake dynamics*". Either way, a fruitful application of those numerical codes or reduced-order models to estimate the VIM responses accurately requires precise statistical validation data that are obtained by well-defined experiments beforehand.

Despite the obvious advantages of using a water towing tank, e.g. high Reynolds-number flows at low towing velocities, equality of Froude number between model-scale and full-scale, realistic boundary conditions and ratio of structural to displaced fluid masses, as well as the high forces and moments that act on the model, these validation experiments are nevertheless closely associated with several major challenges. Those involve, among other things, the limited measurement time in which stable conditions are present due to the finite basin length, the introduction of undesired mechanical vibrations of the towing carriage that are transferred to the test rig and the mounted model while moving on the tracks, and nonlinear deviations between the actual and the desired velocity of the towing carriage, as well as dynamic surface waves at the air-water interface and a seiche with a settling time of several hours to even multiple days, secondary flow effects and turbulence intensity levels that all introduce a significant waiting time between subsequent measurements to minimise their influence on the measurement data. In contrast, parametric validation studies in a closed-loop water or wind tunnel do not only have the advantage of an unlimited measurement time and the absence of a waiting time in between subsequent test cases. They can also be conducted at well-defined boundary conditions that can be nicely reproduced at any time. However, a problem that can arise in wind and water tunnel tests is the large blockage of the oncoming free stream in the test section when placing a large-scale model of the complete offshore structure inside to simulate a high Reynolds-number flow. To avoid large blockage ratios or models that are too small to integrate the required measurement sensors, the current parametrical validation study focuses in a first step on the fluid-dynamic behaviour of merely two prismatic columns with rounded edges in a tandem or in-line arrangement in cross-flow to describe the physics behind the fluid-mechanical phenomena that occur due to the mutual interference between the columns of a floating offshore structure. To preserve a Reynolds-number equality with model tests in a towing tank, the current wind

tunnel tests have been performed in a high-pressure wind tunnel at Reynolds numbers – defined herein as $Re_D = U_\infty D/\nu$ with U_∞ the free-stream velocity and ν the kinematic viscosity of air – as high as 10^7 .

Whereas a large amount of studies have been performed in the past regarding the fluid-dynamic behaviour of two 2D (i.e. "infinite") smooth circular cylinders (Zdravkovich, 1977; Okajima, 1979; Igarashi, 1981; Pearcy et al., 1982; Arie et al., 1983; Igarashi, 1984; Zdravkovich, 1985, 1987; Meneghini et al., 2001; Alam et al., 2003; Zhou and Yiu, 2006; Alam and Zhou, 2007; Carmo et al., 2010; Sumner, 2010; Alam and Meyer, 2011; Alam, 2014; Griffith et al., 2017; Alam et al., 2018; Schewe and Jacobs, 2019; Hosseini et al., 2021; Schewe et al., 2021) or sharp-edged prisms with square cross sections (Reinholds et al., 1977; Shiraishi et al., 1986; Kareem, 1987; Sakamoto et al., 1987; Sakamoto and Haniu, 1988; Luo, 1989; Luo and Teng, 1990; Ohya et al., 1989; Luo and Teng, 1990; Takeuchi and Matsumoto, 1992; Tatsutani et al., 1993; Hangan and Vickery, 1999; Luo et al., 1999; Alam et al., 2002; Liu and Chen, 2002; Kim et al., 2008; Yen et al., 2008; Sohankar and Etminan, 2009; Etminan et al., 2011; Choi et al., 2012; Sohankar, 2012; Duchaine et al., 2014; Sohankar, 2014; Alam et al., 2016b; Du et al., 2019a,b; Shang et al., 2019; Du et al., 2021) placed one behind the other, only a very limited number of numerical and experimental investigations are available on the flow topology around and the fluid forces on a pair of inline square-section prisms with rounded edges. Because the latter cross-sectional shape can be seen as a transition geometry between the aforementioned two extreme cases (hence, circular or sharp-edged square), it is to be expected that the behaviour of the flow around two rounded square-section prisms in tandem arrangement is a mixture of both extremes, whereby the amount of edge roundness plays an important role. To the best of the author's knowledge, the only numerical or experimental published studies that deal with the influence of the edge roundness r/D and centre-to-centre spacing between the prisms S/D on the aerodynamic behaviour of and flow over two "infinite" tandem square-section prisms are very recent and performed at Reynolds numbers of $Re_D = 100$ (Adeeb et al., 2018; Datta et al., 2019; Zhang et al., 2019; Adeeb and Sohn, 2021) and $3000 < Re_D < 4000$ (Virkam et al., 2020), hence, well below typical Reynolds numbers found in many maritime applications.

1.4. Objective of the present study

The obvious lack of experimental validation data concerning the flow interference of two tandem square-section prisms with edge roundness at very to ultra-high Reynolds numbers is thus the motivation for the current experimental study. This flow interference is responsible for changes in the pressure distribution and fluid loads on both prisms, as well as in the strength and frequency of the shed vortices and the flow patterns in the gap between both prisms and in the wake of the downstream prism. From single

isolated smooth and (slightly) rough square section prisms with rounded edges it is well known that, owing to the partially rounded surface shape, the positions of characteristic points of the surface boundary layers and free shear layers – i.e. the transition from laminar to turbulent, the primary and secondary boundary layer separation on the prism’s surface, and the reattachment of the turbulent free shear layers onto its surface – do meander with changing Reynolds number, e.g. Delany and Sorensen (1953); Polhamus (1958); Bokaian and Geoola (1984); Tamura et al. (1998); Tamura and Miyagi (1999); Dalton and Zheng (2003); Hu et al. (2006); Carassale et al. (2013, 2014); van Hinsberg et al. (2017, 2018); van Hinsberg (2021a). As this behaviour induces large effects on the mean and fluctuating loading experienced by the single prism, as well as on the characteristics of the vortex shedding in its wake, it is expected that a change in Reynolds number also has a significant effect on both the ensuing aerodynamic interferences between the two tandem rounded square-section prisms and the value of the critical spacing between them.

In order to address the open points mentioned above, the current wind tunnel study focuses on the systematic description of the (un-)steady forces and pitch moment that act on both rounded square-section prisms in cross-flow, as well as the characteristics, hence strength and frequency, of the shed vortices. For that purpose, the surface pressure distributions, the base pressure C_{pb} , the sectional and

spanwise-integrated mean and fluctuating fluid loads (C_d , C_l , C_m , C_D , C_L , C_D' , C_L'), and the Strouhal number St_L were measured as function of both the Reynolds number and the centre-to-centre spacing. The sectional lift and drag forces and pitch moment acting on each prism were obtained through intergration of the surface pressure distributions, whereas the spanwise-integrated mean and fluctuating aerodynamic loads, the power spectral densities (PSD) of the fluctuating lift forces, and the main Strouhal number(s) of the downstream prism were measured using piezoelectric platform dynamometers. The two square-section prisms had equal non-dimensional edge roundness values of $r/D = 0.16$. All surfaces of each prism were roughened to simulate a light coverage by hard marine fouling (van Hinsberg, 2021a). Based on the research data on semi-submersibles with four square columns that were described in section 1.2, two angles of incidence, i.e. $\alpha = 0^\circ$ and 45° , were selected. For both incidence angles, three spacing values, namely $S/D = 2.8, 4.0$, and 5.6 , were chosen and examined, see Figure 1, thereby covering parts of both the *reattachment* and the *co-shedding* flow state (see section 2.2 for a detailed explanation of these two flow states). For each possible combination of α and S/D , the effect of the Reynolds number on the aerodynamic characteristics of the tandem prism configuration was studied for $1 \times 10^5 \leq Re_D \leq 7 - 8 \times 10^6$, hence, all Reynolds-number flow regimes from subcritical up to transcritical (see section 2.1) were covered.

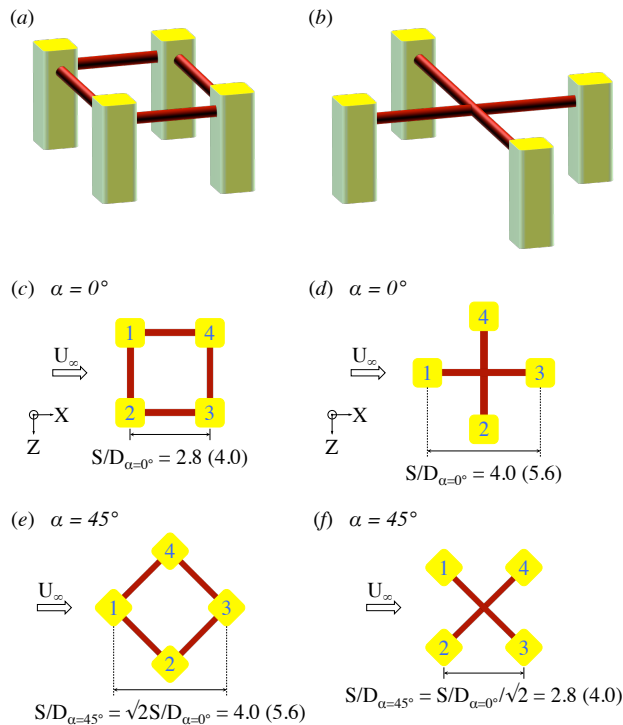


Figure 1: Two possible column arrangements of a four-column deep-draft semi-submersible with the respective column-to-column spacing distances at 0° (c, d) and 45° (e, f) angle of incidence with respect to the oncoming flow.

2. Terminology of the various Reynolds-number flow regimes and flow states of 2D prismatic bodies in cross-flow

A brief overview of two different classification schemes of the flow around a single and two cylindrical or prismatic structures, the latter in a tandem configuration, is given hereafter. The first of these two schemes illustrates the main characteristics of the four different Reynolds-number flow regimes. The categorisation is mainly based on the Reynolds-number-dependent behaviour of the mean drag coefficient and the Strouhal number and can be applied both to single isolated and two in-line cylinders or prisms. In contrast, the second presented classification scheme can only be applied to studies with at least two bluff bodies, since it uses the non-dimensional distance S/D between them as the classification parameter. In this case, the actual designation of the combined global flow field around the bluff bodies to one of the various flow states now depends on the interaction of the free shear layers from the upstream bluff body with the downstream one(s) and the resultant mean drag coefficient and Strouhal number of each of them.

2.1. Reynolds-number flow regimes of 2D square-section prisms with rounded edges in cross-flow

The behaviour of the surface boundary layer, the locations of its separation from the prism, as well as the possible occurrence of a reattachment of the free shear layers and the locations of the resultant secondary separation points characterise the four main high-Reynolds-number flow regimes of a two-dimensional square-section prism with rounded edges in cross-flow: subcritical, critical, supercritical with upper transition, and transcritical (van Hinsberg et al., 2017, 2018; van Hinsberg, 2021a).

The first of these four main high-Reynolds-number flow regimes, the *subcritical flow regime*, is characterised by a surface boundary layer that remains laminar from the stagnation point up to its separation at both windward-directed edges of the rounded square-section prism at $\alpha = 0^\circ$. The two laminar free shear layers that are formed upon separation experience a transition to turbulence at a certain location downstream of the prism's base, its exact position being Reynolds-number dependent. Hence, as no shear-layer reattachment takes place yet, both the two side surfaces and the base of the prism experience a suction force, that results in a high mean drag coefficient, its value being relatively independent of the exact subcritical Reynolds number (van Hinsberg et al. (2017, 2018); van Hinsberg (2021a)). Moreover, the dimensionless frequency with which the vortices are shed in the prism's near wake has a constant value of 0.14 in this flow state.

In the following *critical Reynolds-number flow regime*, a moderate up to strong decrease and a very steep increase of, respectively, the mean drag coefficient (i.e. the "drag crisis") and the Strouhal number take place as the Reynolds number increases. The laminar/turbulent transition wanders upstream along each free shear layer in the direction of the prism's surface. The velocity, with which this transition occurs, does not necessarily has to be equal on both free shear layers. Within a small Reynolds-number range in this flow regime, a bistable state can therefore appear: at one of both side faces the transition point has shifted upstream somewhat faster and thus lies already such close to that side surface that a reattachment of the thicker turbulent free shear layer on this face can occur, thereby forming a recirculating bubble. The attached turbulent boundary layer separates from the surface near the downstream-directed rounded edge, denoted hereafter as the "secondary separation". Since in this limited flow state a separation bubble appears only at one of both side surfaces, an asymmetric surface pressure distribution is formed on the prism that is translated not only in the occurrence of a steady mean lift force, but also in a lower negative mean base pressure and a smaller wake width, i.e. a lower mean drag force on the prism, as well as in a higher Strouhal number. The flow around the prism is furthermore clearly three-dimensional and a hysteresis in the flow phenomena between increasing

and decreasing Reynolds numbers can occur. At the end of this flow regime, the critical Reynolds number is reached. This point is marked by the presence of two separation bubbles, hence, one on each side face of the prism, as well as a secondary separation of the turbulent boundary layer at each downstream-directed rounded edge. The reappearance of a symmetric pressure distribution on the prism's surface results in a sudden cancellation of the steady lift force, whereas the secondary separation of the boundary layer close to the base of the prism leads to a narrow base region and thus a low mean drag coefficient.

A low and relatively constant value of the mean drag coefficient, in combination with a high Strouhal number, define the *supercritical flow regime*. The change from supercritical to transcritical occurs in the upper transition and is accompanied by a gradual decrease of the mean base pressure and a steady increase of the mean drag coefficient. These changes are induced by an upstream motion of the separation point of the turbulent boundary layer, a steady shrinkage of both separation bubbles, and the associated lateral expansion of the wake behind the prism. In the *transcritical flow state*, the transition to turbulence occurs in the vicinity of the stagnation point, hence far upstream of the primary boundary layer separation locations. A steady turbulent flow is formed on the prism and in its wake, thereby inducing a large independency on the Reynolds number of the mean base pressure, the mean and fluctuating aerodynamic force coefficients, and the Strouhal number. With the exception of the fluctuating lift and drag, the values of the various aerodynamic coefficients regain in this flow regimes subcritical levels.

2.2. Flow states for two 2D cylinders in cross-flow in tandem arrangement at subcritical Reynolds numbers

Although the following description of the various flow states is based on measurements on two tandem circular cylinders in cross-flow, exactly the same terminology can also be applied to the current case of two square-section prisms with rounded edges. The reason for this is that in both cases the finite edge curvature allows a smooth transition of the primary (and secondary) boundary layer separation points along the curved surfaces of both bodies.

For a very small centre-to-centre spacing of $1 \leq S/D \leq 1.2 - 1.8$ Zdravkovich (1987) or $1 \leq S/D \leq 2$ Zhou and Yiu (2006) - the exact range being dependent on the value of Re_D - between two tandem cylinders, the free shear layers that have separated from the upstream one overshoot and thus wrap around the downstream cylinder without reattachment. As a result, the unsteady flow and the formation of the Kármán vortices both occur in the wake of the downstream cylinder only. Because the vortex shedding from the upstream cylinder is completely suppressed, the flow in the gap between both tandem cylinders is in this *extended-body regime* or *Mode I* practically stagnant and the two cylinders

act as a single streamlined elliptical structure with a periodic vortex shedding in its wake. Since the vortex formation length is shorter than that for a single isolated cylinder, the Strouhal number of the cylinder pair is found to be higher.

At an increased cylinder-to-cylinder spacing of $1.2 - 1.8 \leq S/D \leq 3.4 - 3.8$ Zdravkovich (1987) or $2 \leq S/D \leq 5$ Zhou and Yiu (2006) a formation and shedding of eddies in the gap between both cylinders takes place. Since the distance between the cylinders is still smaller than the vortex formation length of the upstream one, the free shear layers from the upstream cylinder reattach on the downstream cylinder and thus once again have no possibility to roll up into completely formed distinct vortices. This implies that, similar to the former *extended-body regime*, in the current so-called *reattachment regime* proximity effects still dominate: the vortex shedding from the upstream cylinder is still suppressed at these spacing values and thereupon only one common Kármán vortex street is formed in the wake of the downstream cylinder. Hence, also this regime is marked as *Mode I*. In contrast to the *extended-body regime*, the vortices behind the downstream cylinder are now shed with a lower frequency than that of a single isolated cylinder. Zhou and Yiu (2006) observed that for $S/D = 2 - 3$ the reattachment of the free shear layers separated from the upstream cylinder occurred more often on the leeward side of the downstream cylinder, whereas for $S/D = 3 - 5$ the reattachment mostly took place on the windward side. In the former case, this led to a strong influence on the development and separation of the downstream cylinder's boundary layer, as a result of which weaker and smaller vortices were shed behind the downstream cylinder, whereas in the latter case the Kármán vortices were stronger. Since the spacing between the two tandem cylinders is in both flow regimes relatively small, the presence of the downstream cylinder and the induced flow modification are fed back to the upstream cylinder. The drag force that is experienced by the latter cylinder is therefore in both the *extended-body* and the *reattachment flow regime* lower than that of a single isolated cylinder, whereas the drag force on the downstream cylinder is – depending on the combination of S/D and Re_D – either negative, hence it experiences a thrust force, or close to zero.

In the final *co-shedding regime* ($S/D \geq 3.4 - 3.8$ or $S/D \geq 5$ according to Zdravkovich (1987) and Zhou and Yiu (2006), respectively), which is also denoted as *Mode II*, the downstream cylinder is placed sufficiently far behind the upstream one to allow the free shear layers from the latter cylinder to roll up into distinct vortices in the gap between both cylinders. As a result, the downstream cylinder experiences a periodic vortex impingement. Because the vortex shedding process behind the downstream cylinder is triggered by the arrival of the vortices shed by the upstream cylinder, a synchronisation of both the frequencies and the phases with which the vortices are shed oc-

curs between the two cylinders (Igarashi, 1981, 1984; Alam et al., 2003; Alam, 2016; Wang et al., 2017) and, for very large S/D -values, their values even approach those of a single isolated cylinder. The effect of a combination of vortex impingement on the downstream cylinder and an elevated turbulence intensity of and streamwise structures in the approaching flow leads to a lower spanwise coherence of the wake behind the downstream cylinder (Wu et al., 1994). Zhou and Yiu (2006) furthermore showed that the vortices shed by the downstream cylinder are larger, but at the same time weaker in the current *Mode II* compared to those in *Mode I*, since in the *co-shedding regime* they are formed closer to the base of the downstream cylinder. The drag force experienced by the upstream cylinder nears the value for a single isolated cylinder, whereas a positive drag now acts on the downstream cylinder. However, since the downstream cylinder is exposed to the wake velocity of the upstream cylinder with $u_{wake} < U_\infty$, the drag force on the downstream cylinder is still (much) smaller than that of the upstream one. Depending on the Reynolds number of the undisturbed oncoming flow, the boundary between the *reattachment* and the *co-shedding regime* varies between $S/D = 3.5$ and 5 (Zdravkovich, 1987; Xu and Zhou, 2004; Zhou and Yiu, 2006). It is characterised by the so-called critical or bistable flow spacing S/D_{cr} , at which both flow regimes appear intermittently on either side of S/D_{cr} (Igarashi, 1981; Xu and Zhou, 2004). At the critical spacing a drag inversion takes place: for increasing S/D -values a jump in the drag force on the downstream cylinder from a small negative to a large positive value occurs at S/D_{cr} due to the transition from *Mode I* to *Mode II*. This jump in C_D is coupled with a simultaneous jump in the Strouhal number to a higher value.

3. Experimental approach

The wind tunnel, the test setup instrumentation, and the model instrumentation were similar to those already described in detail in van Hinsberg et al. (2017, 2018); van Hinsberg (2021a,b). The in-house, closed-circuit High Pressure Wind Tunnel is a low subsonic ($U_{\infty,max} \approx 35$ m/s, i.e. incompressible flow with $M_{\infty,max} \leq 0.1$) test facility in which the air can be pressurised up to 10 MPa. In that way maximum Reynolds numbers of 10^7 – based on the width D of the prism – can be achieved in model-scale tests. Its order of magnitude thus approaches that of realistic Reynolds numbers associated with the flow around the columns of multi-column (deep-draft) semi-submersibles. The test section of the wind tunnel has a square cross-section of 0.6×0.6 m² and measures 1 m in length, Figure 2. The free stream turbulence intensity (T.I.) in the test section shows a slight increase with increasing Reynolds number from T.I. = 0.15% up to a maximum value of about T.I. = 0.8%, whereas the relative dynamic pressure variation across the working section at the position of the downstream prism lies below 0.3%.

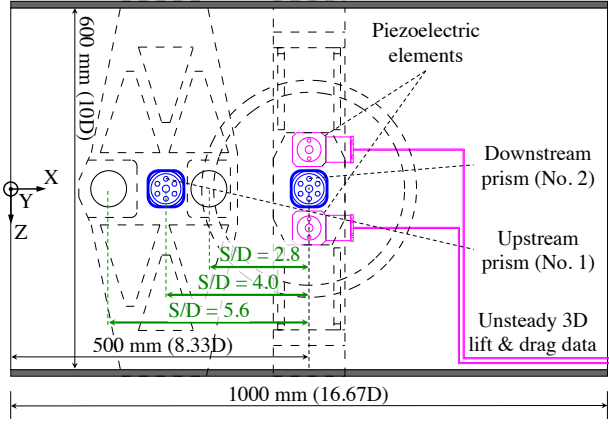


Figure 2: Sketch of the side view of the test section with positions of wind tunnel models and piezoelectric platform dynamometers.

Each square-section prism has a span of $L = 600$ mm and common side lengths of $D = 60$ mm, resulting in an aspect ratio of $AR = L/D = 10$. Both prisms were fabricated through the assemblage of two stainless steel, partially hollow half models. They were then joined together with multiple screws and the heads of the screws were removed by milling. The four spanwise edges of each prism were thereupon rounded to obtain non-dimensional edge curvatures of $r/D = 0.16$, see Figure 3. Each prism side surface was thereafter carefully polished by hand to reduce geometrical imperfections and then covered with a plasmatic metal coating to obtain a non-dimensional equivalent sand-grain surface roughness – based on the algorithm by Adams et al. (2012) – of $k_s/D = 4.5 \times 10^{-4} \pm 2 \times 10^{-5}$, meaning both prisms can be classified as slightly rough. This

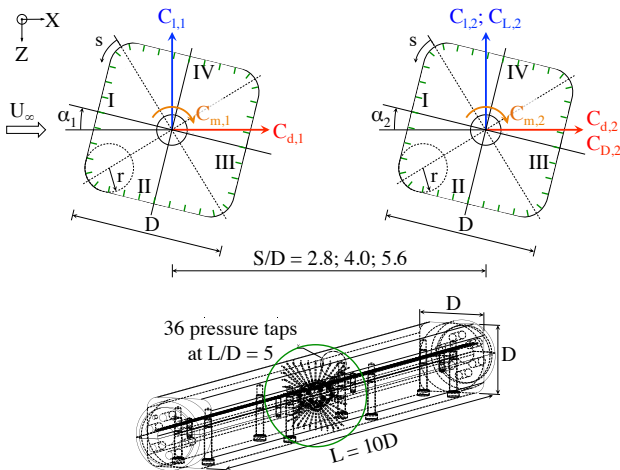


Figure 3: Definition of the positive sectional and spanwise-integrated aerodynamic force vectors, sectional pitch moment coefficients, incidence angles, and surface coordinate s , as well as the numeration of the side surfaces of both prisms (I-IV) and the locations of the 36 pressure taps (green short lines) at each prism's mid-section at $L/D = 5$.

roughness value represents a simulated light coverage of the foundation columns of semi-submersibles by hard marine fouling like oysters, tubeworms, and mussels after a certain time period upon placement in the ocean. Nonetheless, the author is aware, that the characterisation of hard marine fouling by a single parameter k/D (or k_s/D) is not the most suitable solution, since other parameters – such as the limitation of roughness scaling to model sizes, the percentage of coverage, and the axial distribution – have been shown to have a larger influence on the hydrodynamic loading and thus on the resultant fluid-structure interactions (Theophanatos, 1988).

Per prism thirty-six static pressure taps, each with a diameter of 0.3 mm, were equally spaced over the model's mid-span cross-section at $y/D = 5$, see Figure 3. They were connected through small stainless steel and plastic polyester tubes to a temperature-compensated electronic differential pressure measurement unit, having a range of ± 100 kPa. Their positions on the prism surface are given by the non-dimensional circumferential coordinate s/D with $s/D = 0$ at the midpoint of the rounded edge between the surfaces I and IV according to Figure 3. Each pressure tap was furthermore shifted in spanwise direction by a relative amount of 1.65 mm ($y/D = 0.0275$) with respect to its closest neighbours to avoid an interference of the local flow over a tap hole with the wakes generated by the pressure holes located upstream. In the present study only the time-mean surface pressure distributions were obtained with an uncertainty below ± 150 Pa ($= 0.15\%$ FS). Based on the mean surface pressure distribution, the mean sectional pressure drag, lift and pitch moment coefficients could be determined for each prism separately according to

$$C_{l_{1,2}} = \frac{1}{D} \int_s C_{p_{1,2}} n_Z ds = \frac{1}{D} \sum_{i=1}^{36} C_{p_{1,2}} n_{Z,i} ds_i \quad (1a)$$

$$C_{d_{1,2}} = \frac{1}{D} \int_s C_{p_{1,2}} n_X ds = \frac{1}{D} \sum_{i=1}^{36} C_{p_{1,2}} n_{X,i} ds_i \quad (1b)$$

$$C_{m_{1,2}} = \frac{1}{D^2} \int_s C_{p_{1,2}} n_X r ds = \frac{1}{D^2} \sum_{i=1}^{36} C_{p_{1,2}} n_{X,i} r_i ds_i \quad (1c)$$

with $ds_i = (s_{i+1} - s_{i-1})/2$ in which s_i equals the circumferential position of pressure tap i measured along the peripheral of each prism according to Figure 3, n the local normal vector on the prism's surface at the position of pressure tap i , X and Z the downstream and upward directed axes, respectively, with respect to the centre of the prism, r_i the distance from the longitudinal centre axis up to the position of pressure tap i of the respective prism, and $C_{p_{1,2}}$ the pressure coefficient at the pressure tap i , defined as $C_{p_{1,2}} = (p_{i,1,2} - p_\infty)/q_\infty$ with $p_{i,1,2}$ the measured static pressure at pressure tap i , p_∞ the static pressure of the free-stream flow, and q_∞ the free-stream dynamic pressure. The subscripts 1 and 2 correspond to the upstream and downstream

prism, respectively. The mean base pressure coefficients $C_{pb_{1,2}}$ for $\alpha = 0^\circ$ were determined by taking the average of the pressure coefficients obtained with nine taps located on surface III between $s/D = 1.91$ and $s/D = 2.74$, whereas 16 taps on the surfaces III and IV, hence at $2.02 \leq s/D \leq 3.57$, were used to determine $C_{pb_{1,2}}$ at $\alpha = 45^\circ$. The dynamic calibration of the static pressure taps of both prisms showed an upper cut-off frequency of about 860 Hz.

Through surface-oil visualisations on a single square-section 2D prism with equal edge roundness and a smooth surface the author has shown in a previous study (van Hinsberg et al., 2018) that the influence of the limited aspect ratio of $L/D = 10$ on the two-dimensionality of the flow over the prism, and thus on the measured global aerodynamic loading, is relatively small. At both model ends, a small area in cross-flow direction from the wind tunnel wall up to about $y/D = 0.6 - 0.9$ was found in which the flow over the prism was three-dimensional, induced by the boundary layer on the side walls of the test section. Because of the equal position in the test section and comparable boundary conditions, a similar flow distribution is expected around the downstream prism close to both side walls in the current study. The extent of the three-dimensional flow in cross-flow direction on the upstream prism is most likely smaller, since the wall boundary layer is assumed to be thinner at locations further upstream. Because in the current test setup the surface pressure taps are located at mid-span of each prism, the pressure data – and the sectional aerodynamic forces and pitch moment derived therefrom – are obtained in a strictly two-dimensional flow. This implies that the influence of the limited aspect ratio on the measured aerodynamic parameters is thus negligible.

The two prisms were mounted horizontally in a tandem arrangement in the test section and both spanned the complete test-section width from one side wall to the other. The author is aware, that the actual lengths of the columns of semi-submersible floating structures are finite though, as sketched in Figure 1. As the separated flow over these submerged free column ends interacts with the vortex shedding from the sides of the columns, a strongly three-dimensional and highly complex flow field does appear (e.g. Uffinger et al. (2013)). This aspect has nevertheless not been included in the current study to assure a perfect comparison of the current results with those reference measurements on a single 2D prism with equal cross-sectional dimensions and surface roughness height that were conducted in the same wind tunnel, see van Hinsberg (2021a). Both ends of each prism passed through the side walls of the test section. To minimise the amount of flow leakage through the small ring gaps between the model and the side walls labyrinth seals were used. Both model ends of the downstream prism were furthermore connected to rigid piezoelectric platform dynamometers (Figure 2) to obtain the time series of the global, i.e. spanwise integrated, lift $L_2(t)$ and drag $D_2(t)$ forces on this prism. The uncertainty of the recorded dynamometer signals lay below 2%. The there-

upon calculated global time-mean lift and drag coefficients of the downstream prism are defined as $C_{L_2} = \overline{L_2(t)}/(q_\infty DL)$ and $C_{D_2} = \overline{D_2(t)}/(q_\infty DL)$ with $\overline{L_2(t)}$ and $\overline{D_2(t)}$ the mean values of, respectively, the time-dependent lift and drag forces. The PSDs of the fluctuations of the lift force were used to determine the main vortex shedding peaks and corresponding shedding frequencies f_{L_2} . The resulting Strouhal numbers are defined as $St_{L_2} = f_{L_2} \bar{D}/U_\infty$.

Two angles of incidence, $\alpha_{1,2} = 0^\circ$ and 45° , were investigated, whereby for each test run both prisms had the same incidence angle. The resultant geometric wind tunnel blockage ratio was either 0.10 ($\alpha_{1,2} = 0^\circ$) or 0.13 ($\alpha_{1,2} = 45^\circ$). The data presented hereafter for both the tandem configuration and the respective rounded square-section single-prism reference (van Hinsberg, 2021a) have not been corrected for any wall interference effects. The investigated non-dimensional distance S/D between both tandem prisms, i.e. their centre-to-centre spacing, was $S/D = 2.8, 4.0$, and 5.6 (Figure 3). A spacing variation was obtained through a repositioning of the upstream prism, whereas the location of the downstream prism remained fixed at the position of the piezoelectric platform dynamometers, Figure 2. By varying both the free-stream velocity in the range of $U_\infty = 4 - 35$ m/s and the total air pressure inside the wind tunnel, p_0 , between atmospheric and 6 MPa, a Reynolds-number range between 100,000 and 7 to 8 million could be covered. Per measurement point a constant integration time of $T = 30$ s was selected for all recorded signals, as it was demonstrated in a previous study (van Hinsberg et al., 2018) that this time span was sufficient to obtain well-converged mean and fluctuating aerodynamic coefficients. The spanwise-integrated aerodynamic forces were thereby scanned with a sampling frequency of $f_{scan} = 5$ kHz at a resolution of 16 bit.

4. Experimental results

The measurements were performed for $S/D = 2.8, 4.0$, and 5.6 over a large range of Reynolds numbers covering all flow states from subcritical up to high transcritical. The measured values of the sectional mean drag, lift, and pitch moment coefficients (C_d , C_l , and C_m), the spanwise-integrated fluctuating drag and lift coefficients ($\sqrt{\overline{(C'_d)^2}}$ and $\sqrt{\overline{(C'_l)^2}}$), the mean base pressure coefficient C_{pb} , and the Strouhal number St_L are presented hereafter for the two incidence angles of 0° or 45° . Whereas all of these parameters were obtained for the downstream prism, only the sectional aerodynamic coefficients and the base pressure coefficient were measured for the upstream one. The values of their single isolated counterpart with equal surface roughness (van Hinsberg, 2021a), obtained in the same wind tunnel under equal boundary conditions, are considered as reference and therefore also included in the following presentation and discussion of the results.

4.1. Variation in prism-to-prism spacing for 0° angle of incidence

In this section it is demonstrated that a change in the centre-to-centre distance between both prisms at $\alpha = 0^\circ$ has a very distinct influence on the Reynolds-number-dependent behaviour of each of the previously mentioned aerodynamic parameters up to the beginning of the transcritical ($S/D = 2.8$ and 4.0) or supercritical ($S/D = 5.6$) flow regime. A further increase in the Reynolds number towards 10^7 has barely any additional effect on the aerodynamic behaviour of both prisms. Roughly speaking, a larger spacing value induces a reducing mutual interference between both tandem prisms. This is mirrored both by the disappearance of a thrust force (*mode I*) that acts on the downstream prism, in combination with jumps in C_d from positive (*mode II*) to negative (*mode I*) and visa versa in the critical flow regime between $S/D = 2.8$ and 4.0 and by a gradual convergence of multiple aerodynamic coefficients of each prism towards the values of an isolated prism. A change in S/D from 2.8 to 4.0 results furthermore in the cancellation of the upper transition, whereas at $S/D = 5.6$ the transcritical flow regime vanishes as well.

4.1.1. Mean aerodynamic loading

The sectional, hence local, mean drag coefficients of both prisms $C_{d_{1,2}}$, obtained by the circumferential integration of the mean surface pressures in the mid-span cross-section of each prism according to equation (1b), are presented in Figure 4 as function of the Reynolds number for the three investigated prism-to-prism spacing values. For comparison reasons, the reference curves of the sectional mean drag coefficient of the isolated rounded square-section prism by van Hinsberg (2021a) have been included in Figure 4.

Focussing first on the Reynolds-number dependency of the mean drag coefficient of the upstream prism, the values of C_{d_1} for subcritical Reynolds numbers of $Re_D < 3 \times 10^5$ coincide at all three spacing values very well with the drag coefficients belonging to the single prism. The subsequent decrease of C_{d_1} in the critical Reynolds-number flow regime, i.e. the "drag crisis", is for the smallest spacing value of $S/D = 2.8$ steeper than for its single isolated counterpart and continues up to a somewhat larger Reynolds number of $Re_D = 4.5 \times 10^5$ (Figure 4a). The resultant drag coefficient at this critical Reynolds number, which marks the crossover from the critical to the supercritical flow regime, is therefore more than twice as low: $C_{d_1} = 0.25$ compared to $C_{d_{single}} = 0.63$, the latter at $Re_{D_{cr}} = 4 \times 10^5$. In contrast to the single isolated prism, for which a more or less constant drag coefficient of $C_{d_{single}} = 0.6 - 0.8$ is present for supercritical Reynolds numbers up to $Re_D = 10$ million, the upstream of both tandem prisms possesses a limited supercritical Reynolds-number regime with constant drag coefficients of $C_{d_1} \approx 0.25$. This is followed by a rather long and steady increase in the mean drag coefficient over a Reynolds-number range of $7.0 \times 10^5 \leq Re_D \leq 2.23 \times 10^6$,

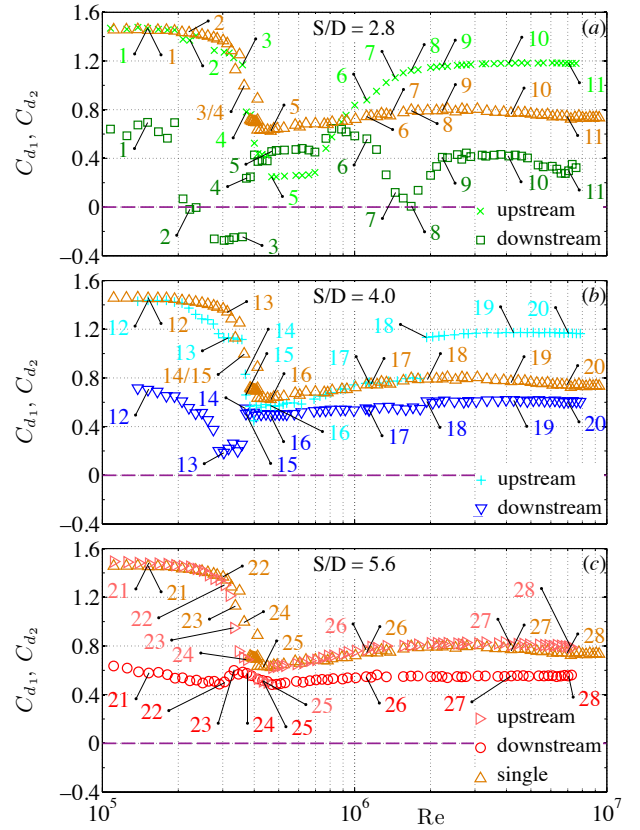


Figure 4: Sectional mean drag coefficient, C_d , as function of the Reynolds number Re_D for both tandem 2D square prisms with rounded edges of $r/D = 0.16$ at $\alpha = 0^\circ$. C_{d_1} : upstream prism; C_{d_2} : downstream prism. (a): $S/D = 2.8$, (b): $S/D = 4.0$, and (c): $S/D = 5.6$. \triangle : single isolated reference prism by van Hinsberg (2021a). The selected data points 1 to 28 are listed in Appendices A1 and A2.

i.e. the upper transition flow regime, and a second nearly constant plateau of C_{d_1} for Reynolds numbers larger than 2.23 million. In this latter transcritical flow state the mean drag force on the upstream prism has a value of $C_{d_1} \approx 1.18$ that lies at a level of about 83% of its mean subcritical value. Interesting to note at this point is the similarity between the trend of the $C_{d_1}(Re_D)$ curve for $S/D = 2.8$ and the trends of the $C_{d_1}(Re_D)$ curves for a single rounded square-section prism, but with a larger non-dimensional surface roughness value of $k_s/D = 1.0 \times 10^{-3}$ or 1.4×10^{-3} , see van Hinsberg (2021a).

An increase in the spacing results in a gradual convergence of the $C_{d_1}(Re_D)$ curve towards the reference curve. At the medium spacing of $S/D = 4.0$ (Figure 4b), the drag crisis in the critical Reynolds-number regime is less severe, resulting in $C_{d_1} = 0.58$ at the $Re_{D_{cr}} = 4.1 \times 10^5$ at the end of the critical flow state. Hence, both the location of the critical Reynolds number and the corresponding drag coefficient at $S/D = 4.0$ coincide with those values of its single counterpart ($C_{d_{single}}(Re_{D_{cr}} = 4 \times 10^5) = 0.63$). The complete subsequent supercritical flow state is characterised by an almost perfect match between C_{d_1} and $C_{d_{single}}$. At $Re_D =$

1.85×10^6 a jump in C_{d_1} from a nearly constant first plateau of $C_{d_1} \approx 0.76$ to a second plateau at $C_{d_1} = 1.13 - 1.17$ takes place. The upper transition, clearly present at the smallest spacing value of $S/D = 2.8$, has thus disappeared at $S/D = 4.0$. Over the complete transcritical flow regime up to a Reynolds number of about 8 million, the drag coefficient corresponds at this intermediate spacing then again very well to the transcritical drag values obtained for the tandem configuration at $S/D = 2.8$.

At the largest spacing, $S/D = 5.6$, the appearance of the $C_{d_1}(Re_D)$ curve is not only similar to that one of the single prism, but the values of the drag coefficients for both configurations show at equal Reynolds numbers even a near to perfect match (Figure 4c). The only exception is the critical Reynolds-number regime, for which, similar to $S/D = 2.8$, somewhat smaller drag coefficients are obtained, since at $S/D = 5.6$ the drag crisis is both steeper than its single counterpart and continues up to a higher Reynolds number of $Re_{D_{cr}} = 4.5 \times 10^5$. In addition, it is noteworthy that for this tandem configuration the transcritical flow regime, still present at $S/D = 4.0$ for $Re_D \geq 1.93 \times 10^6$, has vanished as well, hence the supercritical flow state is present for all Reynolds numbers larger than the critical Reynolds number of $Re_{D_{cr}} = 4.5 \times 10^5$. At this stage, it can thus be stated, that a centre-to-centre prism spacing of $S/D = 5.6$ is large enough to prevent a clear interference of the flow around the upstream prism by the direct presence of the downstream partner in its wake. Based on its drag characteristics at a spacing $S/D = 5.6$, the aerodynamic behaviour of the upstream one in a tandem arrangement of two rounded square-section prisms with $S/D \geq 5.6$ can thus be treated as being equivalent to that one of an isolated prism in cross-flow.

The shapes of the drag curves of the downstream prism, C_{d_2} , reveal that each one of them exhibits a completely different development with increasing Reynolds number compared to their respective upstream counterparts. For the smallest spacing of $S/D = 2.8$, two jumps in C_{d_2} occur in the subcritical flow state: the first one, at $Re_D = 2 \times 10^5$, is characterised by a sharp drop from a first plateau at $C_{d_2} \approx 0.6 - 0.7$ to a second, shorter plateau at $C_{d_2} \approx 0$, whereas the second drop, at $Re_D = 2.6 \times 10^5$ near the end of the subcritical flow state, is smaller and ends at a third plateau at $C_{d_2} \approx -0.25$ (Figure 4a). A positive sign of the mean drag force acting on the downstream prism indicates that at these subcritical Reynolds numbers the state of the flow around both tandem prisms can be assigned to the *co-shedding regime (mode II)*. In contrast, the negative sign of C_{d_2} for high subcritical and low critical Reynolds numbers reveals that the state of the flow around both prisms has switched to the *reattachment regime (mode I)*, for which a vortex street is formed behind the downstream prism only. In the former case, the spacing $S/D = 2.8$ lies above the critical spacing S/D_{cr} , whereas in the latter case it lies below the critical spacing. The centre plateau at $C_{d_2} \approx 0$ for $2 \times 10^5 \leq Re_D \leq 2.6 \times 10^5$ is a special case. At these Reynolds numbers the

downstream prism experiences no net drag force; the spacing $S/D = 2.8$ corresponds exactly to the critical spacing. At $Re_D \approx 3.6 \times 10^5$ in the critical flow state a second zero-crossing of the downstream prism's mean drag force from $C_{d_2} = -0.24$ to 0.24 is seen to occur, which is directly followed by a second, smaller step in C_{d_2} to 0.43 at $Re_D = 4.0 \times 10^5$. Based on this second sign reversal of the drag force, the flow around the tandem configuration has thus changed once more, this time from *mode I* back to *mode II*. More precisely, a transition from the *reattachment regime*, in which proximity interference effects are dominant, to the *co-shedding regime*, in which the free shear layers that have separated from the upstream prism can reattach on the downstream one, has taken place. The mutual interference between both tandem prisms now becomes clear as well: the sign reversal of C_{d_2} at $Re_D \approx 3.6 \times 10^5$ is accompanied by a decrease of the upstream prism's drag coefficient by 1/3 of its value. On the contrary, only small changes in C_{d_1} were measured around the first cross-over in the subcritical flow state. In section 5.1 it is shown that these differences are caused by a different behaviour of the free shear layers that have separated from each of the two prisms. At the end of the subcritical flow state up to the critical Reynolds number of $Re_{D_{cr}} = 4.5 \times 10^5$ both prisms experience an equal positive drag force, i.e. $C_{d_1} = C_{d_2} = 0.4$. Over the complete supercritical flow state and in the first part of the upper transition up to a Reynolds number of 8.5×10^5 we are faced with the paradoxical situation that the downstream prism experiences a higher positive drag force than the upstream one. A similar observation was described by Schewe et al. (2021) for two tandem smooth cylinders with spacing values of $S/D = 1.56, 2.8$, and 4.0 at supercritical Reynolds numbers. We attributed this phenomenon to the formation of separation bubbles on the upstream cylinder's surface in the supercritical state, induced by the upstream shift of the location of the laminar/turbulent transition on the separated shear layers towards the shoulders of the upstream cylinder. The formation of the separation bubbles leads to a secondary turbulent boundary layer separation on the downstream half of the cylinder, a sharp reduction in the width of the wake behind the upstream cylinder and thus a smaller shielding of the downstream prism by the upstream one. As a result, the drag force on the downstream cylinder increases to values that are higher than for the upstream prism. In section 5.1 it is discussed that the large differences in the surface pressure distribution on both prisms are also in this case responsible for the drag inversion between the upstream and the downstream prism. For $Re_D \geq 8.5 \times 10^5$ the upper transition is marked by a gentle decrease of the drag on the downstream prism from $C_{d_2} = 0.64$ to 0 , which is directly followed by an increase towards $C_{d_2} = 0.41$ at the cross-over from the upper transition to the transcritical flow state. At $Re_D = 1.68 \times 10^6$ the downstream prism experiences once again no net drag force, meaning we scratch once more at exactly the critical spacing. Since the net mean drag force on the downstream prism does not become negative at this Reynolds number, the state of the

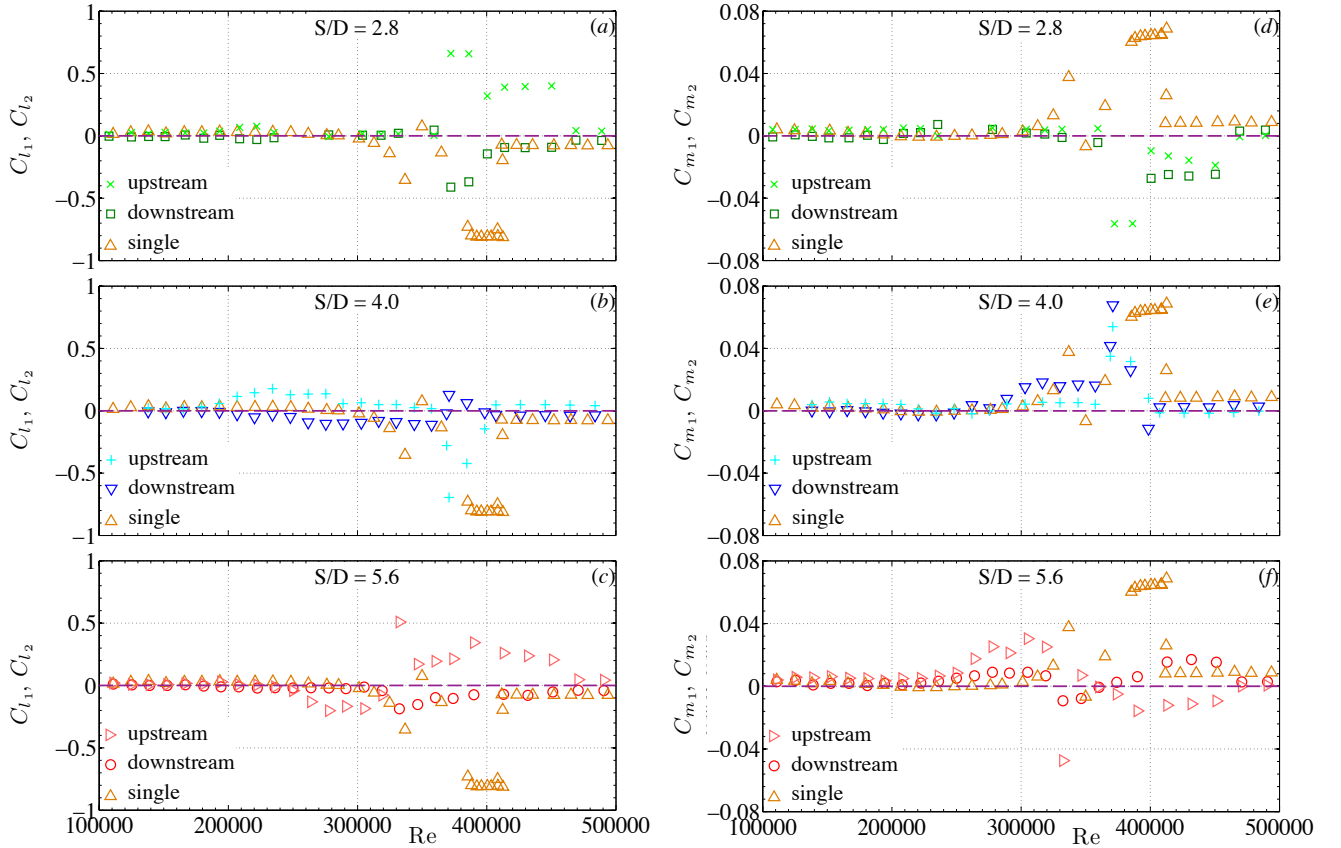


Figure 5: Dependency of the sectional mean lift (left column) and pitch moment (right column) coefficients on the Reynolds number for both tandem 2D square prisms with rounded edges of $r/D = 0.16$ at $\alpha = 0^\circ$. C_{l_1} and C_{m_1} : upstream prism; C_{l_2} and C_{m_2} : downstream prism. (a),(d): $S/D = 2.8$; (b),(e): $S/D = 4.0$; (c),(f): $S/D = 5.6$. \triangle : single isolated reference prism by van Hinsberg (2021a).

flow around the tandem configuration, i.e. *mode II*, remains unchanged. Similar to C_{d_1} , fairly constant values of C_{d_2} are obtained for transcritical Reynolds number approaching $Re_D \rightarrow 10^7$.

With regard to the medium and large prism centre-to-centre spacing values $S/D = 4.0$ and 5.6 , the trends of the $C_{d_2}(Re_D)$ curve are rather different compared to the preceding case. An increase in the spacing induces a stronger flattening of the curve; hence, the mean drag coefficient of the downstream prism shows an increased independency on the Reynolds number over the complete investigated Reynolds-number range. The most striking difference to the curve of C_{d_2} at $S/D = 2.8$, though, is the nonexistence of one or multiple zero-crossings of C_{d_2} at both larger spacing values; hence, both distances lie above the critical spacing S/D_{cr} , the state of the flow thus equals the *co-shedding regime* or *mode II* and remains unchanged with varying Reynolds number.

For the medium spacing, the decrease of C_{d_2} in the second half of the subcritical flow regime, i.e. for $Re_D \geq 2 \times 10^5$, is relatively smooth and characterised by only one distinct step in C_{d_2} at $Re_D \approx 2.8 \times 10^5$ from $C_{d_2} = 0.38$ to 0.20 (Figure 4b). This is followed by a relatively con-

stant, but short plateau of $C_{d_2} = 0.2 - 0.25$ for low critical Reynolds numbers between 2.8×10^5 and 3.6×10^5 , and a jump upwards to $C_{d_2} = 0.55$ around $Re_D = 3.6 \times 10^5$. The occurrence of this steep increase in C_{d_2} at the exact same Reynolds number at which the upstream prism's mean drag coefficient decreases sharply from $C_{d_1} = 1.12$ to 0.83 is a clear evidence for the mutual interference between both tandem prisms at this spacing. Throughout the complete supercritical and the following transcritical flow regime, C_{d_2} remains approximately constant at a value of, respectively, 0.52 and 0.61 . In contrast to the upstream prism, for which a sharp increase in the mean drag coefficient by more than 50% occurs at the cross-over from the supercritical to the transcritical flow regime, the downstream prism thus experiences a modest increase of about 17% only.

It was already mentioned that for the largest distance $S/D = 5.6$, the behaviour of the drag curve of the downstream prism is highly independent of the Reynolds number (Figure 4c). The subcritical Reynolds-number regime is characterised by a linear decrease in C_{d_2} from 0.64 at $Re_D = 1.1 \times 10^5$ to 0.49 at $Re_D = 2.9 \times 10^5$. A small bump with a local maximum of $C_{d_2} = 0.60$ at $Re_D = 3.3 \times 10^5$ appears in the subsequent critical flow regime. The supercritical plateau at $C_{d_2} = 0.55$ begins at the critical Reynolds

number of $Re_{D_{cr}} = 4.5 \times 10^5$ and continues up to Reynolds numbers approaching 10^7 .

With the exception of the critical flow regime, the measured mean sectional lift and pitch moment coefficients are for both prisms at all three spacing values practically zero. The graphs in the figures 5a to 5c (left column) and 5d to 5f (right column) present $C_{l_{1,2}}$ and $C_{m_{1,2}}$ – calculated according to equations (1a) and (1c), respectively, by using the mean surface pressure distributions – as function of the Reynolds number for $1 \times 10^5 \leq Re_D \leq 5 \times 10^5$; hence, the presented data cover the upper part of the subcritical, the complete critical, and the lower part of the supercritical flow regimes. The graphs show that clear non-zero mean lift forces and pitch moments act on both tandem prisms at most Reynolds numbers in the critical flow state. However, neither a clear dependency on the Reynolds number nor a correlation of one or both aerodynamic coefficients with the prism-to-prism spacing can be recognised. This not only applies to the trends of the $C_l(Re_D)$ and $C_m(Re_D)$ curves of both prisms, but also to the local or absolute minimum and/or maximum values and the sign of the coefficients.

In previous studies on the flow around single rounded square-section prisms with various surface roughness values (van Hinsberg et al., 2017, 2018; van Hinsberg, 2021a) it was discussed that the appearance of a recirculation bubble above only one of both side surfaces at certain Reynolds numbers in the critical flow state induces a clear imbalance between the mean pressure forces on these two prism surfaces. This results in a highly asymmetric flow pattern around the prism with strong differences between the shapes of the two large counter-rotating wake vortices, which then again induces a steady mean lift force, i.e. the asymmetric flow state. A similar behaviour of the free shear layers that have separated from each of the two prisms is also responsible for the appearance of the steady mean lift force and pitch moment on both tandem prisms within the critical Reynolds-number regime in the current study, although the influence of the proximity effects on the flow around the two tandem prisms now needs to be taken into account as well, as is explained in more detail in section 5.1.

4.1.2. Mean base pressure coefficient

Figure 6 shows the relation of the mean base pressure coefficient at the mid-section of the upstream prism, C_{pb_1} , and the downstream prism, C_{pb_2} , to the Reynolds number for all three spacing values, as well for the single reference prism, $C_{pb_{single}}$, by van Hinsberg (2021a). What probably catches the reader's eye right away are the trends of the $C_{pb}(Re_D)$ curves for both tandem prisms: independent of the value for S/D , each one of them shows a similar behaviour as the corresponding curve of the sectional drag coefficient $C_{d_{1,2}}$ in Figure 4. This also counts for the discontinuous steps in C_{pb_2} and C_{d_2} that occur in the subcritical and critical flow regimes at $S/D = 2.8$ and 4.0, as well as for both prisms at the cross-over from the supercritical

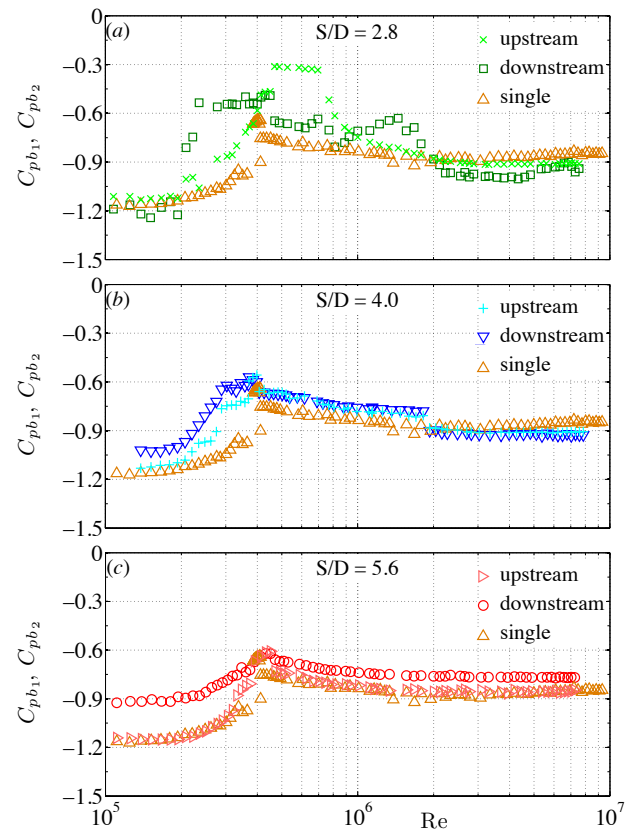


Figure 6: Mean base coefficient, C_{pb} , as function of the Reynolds number Re_D for both tandem 2D square prisms with rounded edges of $r/D = 0.16$ at $\alpha = 0^\circ$. C_{pb_1} : upstream prism; C_{pb_2} : downstream prism. (a): $S/D = 2.8$, (b): $S/D = 4.0$, and (c): $S/D = 5.6$. \triangle : single isolated reference prism by van Hinsberg (2021a).

to the transcritical regime at $S/D = 4.0$. This common behaviour of both aerodynamic coefficients is actually not that surprising, as a change in the (mean) base pressure alters the net (mean) pressure force that acts on the prism in flow direction. An increase in the absolute values of C_{pb} thus leads to a larger drag force, whereas a decrease of the absolute base pressure induces a smaller drag force on the prism. This dependency becomes particularly clear when comparing the curves of C_d and C_{pb} for each of the two tandem prisms at the smallest spacing of $S/D = 2.8$.

Small differences between the trends of C_{pb} of both tandem prisms can also be observed. An increase of S/D leads to smaller and less prominent variations in C_{pb_2} ; hence, the mean base pressure coefficient of the downstream prism shows an increased independency on the Reynolds number. At $S/D = 5.6$, there appears at the crossover from the critical to the supercritical regime for example only a kink in the curve. At the same spacing, both the appearance of the $C_{pb_1}(Re_D)$ curve and the values of C_{pb_1} coincide with those obtained for the single isolated prism. However, for smaller spacing values the absolute values of C_{pb_1} for high subcritical Reynolds numbers up to the end of the upper transition

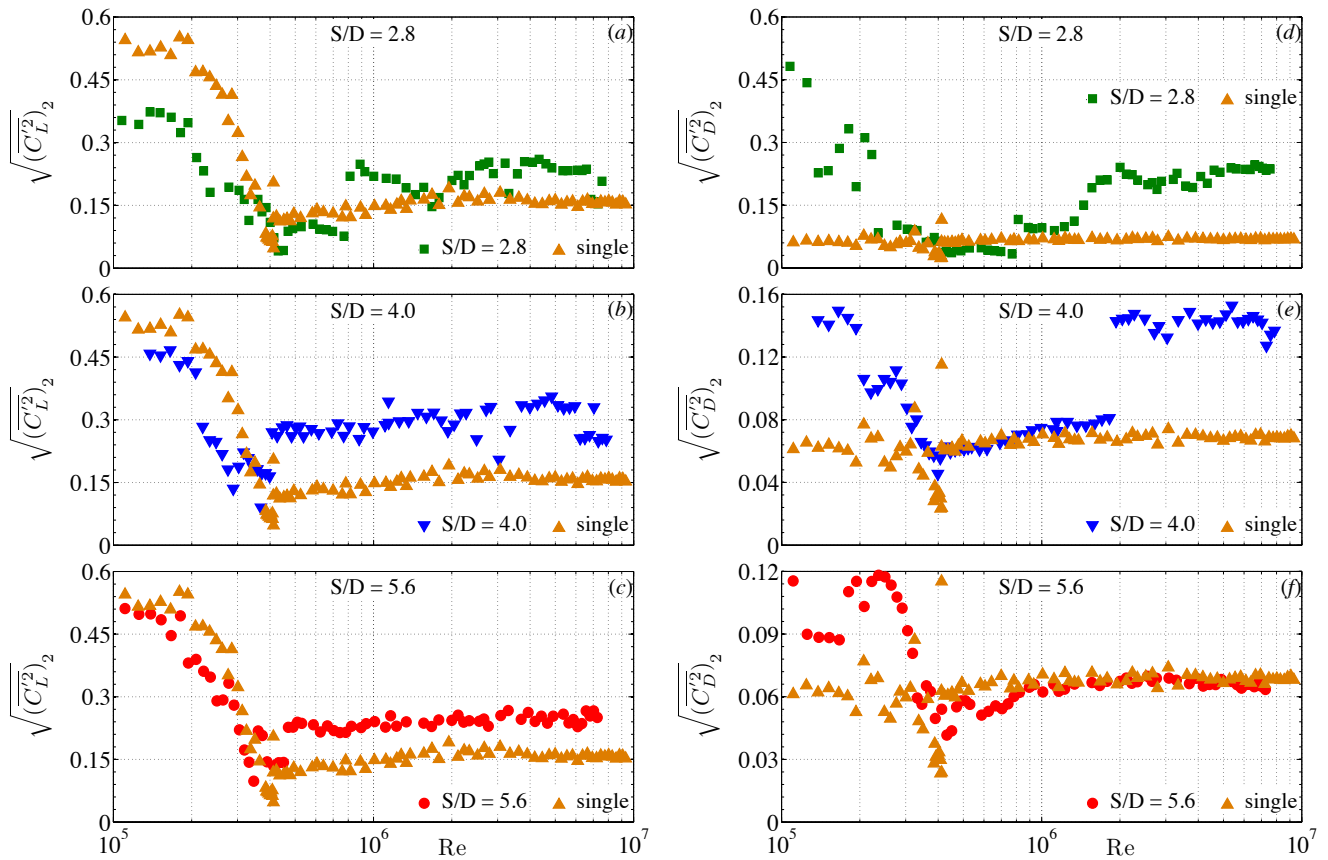


Figure 7: Dependency of the global (spanwise-integrated) fluctuating lift (left column) and drag (right column) force coefficients on the Reynolds number for the downstream 2D square prism with rounded edges of $r/D = 0.16$ at $\alpha = 0^\circ$. (a),(d): $S/D = 2.8$; (b),(e): $S/D = 4.0$; (c),(f): $S/D = 5.6$. \blacktriangle : single isolated reference prism by van Hinsberg (2021a).

at 2×10^6 are lower than those for the single isolated prism. In particular for the smallest spacing, the interference effects between both prisms at these Reynolds numbers, i.e. the occurrence of a zero net drag force and even a thrust force on the downstream prism, are reflected in a significant decrease in the mean suction pressure compared to a single prism.

4.1.3. Fluctuating aerodynamic forces

In the current study, only the fluctuating lift and drag forces on the downstream prism were measured. Their values are shown in Figure 7 as function of the Reynolds number for all three spacing values, once again together with the results for a single prism presented in van Hinsberg (2021a). Note that these data were obtained using piezoelectric platform dynamometers; hence, in contrast to the sectional lift, drag, pitch moment, and base pressure coefficients, the presented fluctuating lift and drag coefficients are spanwise-integrated values.

For low subcritical Reynolds numbers of $Re_D \leq 2 \times 10^5$ the data of the fluctuating lift force, $\sqrt{(C_L'^2)_2}$, for the smallest spacing $S/D = 2.8$ in Figure 7a are at a relatively constant plateau of $\sqrt{(C_L'^2)_2} = 0.35 - 0.37$. This is followed

by a steady decrease throughout the high subcritical and the critical flow regime, down to a minimum of $\sqrt{(C_L'^2)_2} = 0.042$ at the critical Reynolds number of $Re_D = 4.3 \times 10^5$ just prior to the cross-over from the critical to the supercritical flow regime. Whereas in the previous two flow regimes lower fluctuating lift forces on the downstream prism are obtained compared to the single prism, constant values of approximately $\sqrt{(C_L'^2)_2} = 0.09$, similar to those of its single counterpart, are observed for all supercritical Reynolds numbers. A step of $\Delta \sqrt{(C_L'^2)_2} = 0.14$ occurs at $Re_D = 8 \times 10^5$, hence, at the beginning of the upper transition. Throughout the upper transition and subsequent transcritical flow regime, the values of the fluctuating lift forces are higher than those of a single prism. A relatively broad dip in the $\sqrt{(C_L'^2)_2}(Re_D)$ curve down to $\sqrt{(C_L'^2)_2} = 0.15$ can be seen around $Re_D = 1.68 \times 10^6$, which correlates with the location in the $C_{d_2}(Re_D)$ curve at which the downstream prism experiences a net drag force of zero (i.e. $S/D = 2.8 = S/D_{cr}$), and a second smaller one down to $\sqrt{(C_L'^2)_2} = 0.18$ at $Re_D = 3.13 \times 10^6$. At very high transcritical Reynolds numbers $\rightarrow 10^7$ the downstream prism experiences once

again relatively constant fluctuating lift forces of $\sqrt{(C'_L)^2_2} = 0.24$.

For both larger spacing values, a similar trend of the fluctuating lift forces on the downstream prism to the one previously described for $S/D = 2.8$ is observed in the subcritical and critical flow regime, see Figure 7b and 7c. The difference between the values for the downstream prism and its single counterpart at equal Reynolds numbers is smaller than at $S/D = 2.8$ though, and shrinks with increasing spacing value. The same counts for the negative slope of the $\sqrt{(C'_L)^2_2}(Re_D)$ curve in both flow regimes for $S/D = 4.0$ and 5.6. A jump in $\sqrt{(C'_L)^2_2}$ at the end of the critical Reynolds-number regime occurs at both larger spacing values as well, after which constant values of the fluctuating lift force are obtained throughout the complete supercritical flow regime. In this latter flow regime, the values of $\sqrt{(C'_L)^2_2}$ are for the medium spacing about 60% higher than those of the single prism, and for the largest spacing even twice as high. At the beginning of the transcritical flow state, the $\sqrt{(C'_L)^2_2}(Re_D)$ curve for $S/D = 4.0$ dips three times before dropping to a new plateau at $\sqrt{(C'_L)^2_2} = 0.25$ for $Re_D \geq 6$ million.

The distribution of the fluctuating drag force on the downstream prism, $\sqrt{(C'_D)^2_2}$, as function of the Reynolds number in the Figures 7d to 7f displays some interesting features as well. Firstly, all three curves show to a large extent qualitatively similar trends over all four flow regimes as the mean drag coefficient of the upstream prism C_{d1} presented in Figure 4 in section 4.1.1. Hence, high values in the subcritical flow state, a strong decrease in the critical flow state, and constant low values for the supercritical flow state, as well as a gradual increase in the upper transition for $S/D = 2.8$, and nearly constant values throughout the transcritical flow state for $S/D = 2.8$ and 4.0. The same counts for the steep jump in the curves at the crossover from the supercritical to the transcritical flow regime for $S/D = 4.0$ at $Re_D = 1.85 \times 10^6$. One notable exception to this overall trend is observed for the values within the subcritical and critical flow states for the smallest spacing: at this configuration, a sharp decrease of $\sqrt{(C'_D)^2_2}$ occurs over the subcritical flow state, and relatively constant values were measured at critical Reynolds numbers. Secondly, the fluctuating drag force is within the subcritical flow state much larger than that of a single prism at equal Reynolds number; however, this difference decreases with increasing spacing. Thirdly, the values of the fluctuating drag force within the supercritical flow state lie for the smallest spacing below and for both other spacing values on top of the values for their single counterpart; hence, similar to the behaviour of C_{d1} in Figure 4. Last, but not least, it is interesting to note that for $S/D = 2.8$ the transcritical values of $\sqrt{(C'_D)^2_2}$ are

nearly half of their subcritical values, whereas for $S/D = 4.0$ equal high values are obtained in both flow regimes.

4.1.4. Strouhal number and power spectra

Figure 8 shows the behaviour of the non-dimensional frequency of the vortices shed in the wake of the downstream prism, St_{L_2} , with increasing Reynolds number. The presented Strouhal numbers are based on the main and, when applicable, also the secondary frequency peak in the PSDs of the time series of the fluctuating lift coefficient $C_{L_2}(t)$ that were measured with the piezoelectric platform dynamometers.

The trends of the three $St_{L_2}(Re_D)$ curves in Figure 8 are similar within each flow regime. For all subcritical Reynolds numbers constant Strouhal numbers of $St_{L_2} = 0.12 - 0.14$ are present. The most striking feature in the subsequent critical flow state is the occurrence of two Strouhal numbers for the downstream prism at the same Reynolds number: $St_{L_2} \approx 0.12$ and 0.22 or $St_{L_2} \approx 0.21$ and 0.25 (dependent on the exact Reynolds number) for $S/D = 2.8$,

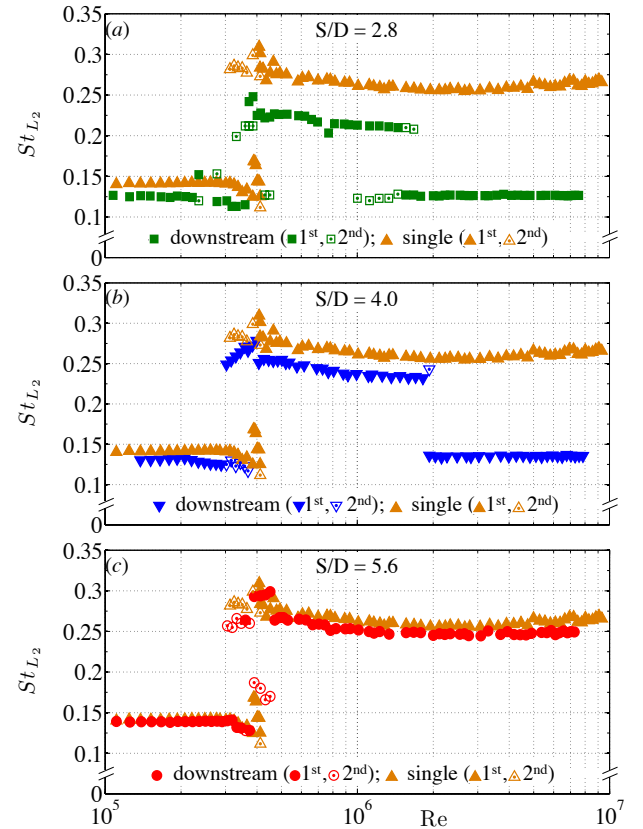


Figure 8: Strouhal numbers obtained from the fluctuating lift forces acting on the downstream prism at $\alpha = 0^\circ$ as function of the Reynolds number and the spacing. (a): $S/D = 2.8$, (b): $S/D = 4.0$, and (c): $S/D = 5.6$. \blacktriangle : single isolated reference prism by van Hinsberg (2021a). In various flow states two peaks occurred in the power spectra at the same Reynolds number. The dominant Strouhal number is indicated by a filled symbol, whereas a dot within the symbol belongs to the secondary peak.

$St_{L_2} \approx 0.13$ and 0.26 for $S/D = 4.0$, and $St_{L_2} \approx 0.13$ and 0.26 or $St_{L_2} \approx 0.17$ and 0.29 (again, dependent on the exact Reynolds number) for $S/D = 5.6$. The Strouhal number that belongs to the dominant peak in each spectrum is indicated by a filled symbol in Figure 8. Hence, the open symbols having dots inside them belong to secondary peaks. Representative examples of the power spectra of the unsteady lift forces at selected Reynolds numbers throughout the large studied range of $Re_D = 1 \times 10^5$ to 8×10^6 are presented in the Figure 9 and discussed later on in this section. Since the lower of the two occurring Strouhal numbers is linked to the subcritical flow state and the higher one to the supercritical flow state, this means that for these critical Reynolds numbers the flow around the downstream prism switches continuously back and forth between both flow states. This alternating behaviour extends up to the end of the critical flow regime, at which a permanent cross-over to the supercritical flow regime takes place and the Strouhal number settles at a relatively flat supercritical plateau of $St_{L_2} = 0.22 - 0.26$. Whereas for the largest of the three spacing values the $St_{L_2}(Re_D)$ curve remains at this high supercritical value up to $Re_D \rightarrow 10^7$, the Strouhal numbers for both smaller spacing values drop to a new plateau that corresponds to their respective subcritical level of $St_{L_2} = 0.13$ ($S/D = 2.8$) and 0.14 ($S/D = 4.0$), which prolongs up to the highest measured Reynolds number. For both spacing values, this jump in St_{L_2} is once more accompanied with the occurrence of two Strouhal numbers, hence, two peaks in the power spectra; for the smallest spacing at Reynolds numbers of $1 \times 10^6 - 1.68 \times 10^6$ within the upper transition, and at a single Reynolds number of $Re_D = 1.93 \times 10^6$ for the intermediate spacing.

A direct comparison with the Strouhal numbers obtained for the single prism leads to the conclusion that an increase in S/D induces a shift of the Strouhal number for the downstream prism towards those of the single prism. For $S/D = 2.8$, the Strouhal numbers of the downstream prism are about 14% lower in the subcritical regime and even 22% lower in the supercritical flow regime. This decreases to a difference of merely 7% in both flow states for $S/D = 4.0$, whereas for $S/D = 5.6$ both curves match almost perfectly. Purely based on the Strouhal numbers in Figure 8c, one could argue that the prisms' centre-to-centre distance of $S = 5.6D$ between both tandem prisms is large enough, such that the frequency with which the vortices are shed in the wake of the downstream prism does not seem to be affected by the presence of the upstream one. This is, however, contradicted by the different values of the mean and fluctuating aerodynamic force coefficients and of the mean base pressure coefficient of, on one hand, the downstream prism at $S/D = 5.6$ and, on the other hand, the single prism at the same Reynolds number. These differences show that proximity effects are still present at this spacing. The mean and fluctuating aerodynamic data of the upstream prism then again coincide very well with those of a single prism; it can therefore be expected that this also counts for the Strouhal numbers of this upstream prism. A

second, more likely scenario is thus that at the spacing $S/D = 5.6$ the vortex shedding process behind the downstream prism is triggered by the arrival of the vortices shed by the upstream one, which results in a synchronisation of the vortex shedding frequency of the downstream prism with that of the upstream prism. Although this second scenario is supported by the many experimental and numerical studies on two tandem cylinders or sharp-edged square-section prisms in cross-flow that have been mentioned in the introductory section, synchronised measurements of the vortex shedding frequencies behind each of the two rounded square-section prisms or PIV measurements would be required to get a definite answer.

To give an overview of how the spectra of the fluctuating lift force $C_{L_2}(t)$ that acts on the downstream prism develop from subcritical up to very high Reynolds numbers of $\mathcal{O}(10^7)$, multiple spectra, typical for the various Reynolds-number regimes, are shown in Figure 9 for each spacing value. The one or two main peaks of each spectrum, i.e., the first harmonics, resemble the frequencies of the vortex shedding process in the base region behind the downstream prism. Where applicable, the second and/or third harmonics have been marked in the spectra as well. The subscripts of the Strouhal numbers listed therein correspond to the points marked in Figure 4. For those selected Reynolds numbers, each of the aerodynamic coefficients that have been presented in the previous sections are also listed in Appendix A1 for both tandem prisms and in Appendix A2 for the single prism.

The power spectra of the points 1 and 2 in Figure 9a for the spacing of $S/D = 2.8$ were recorded at $Re = 1.5 \times 10^5$ and 2.2×10^5 , respectively, and are typical for the subcritical flow regime. The main feature is the appearance of a single dominant and relatively narrow peak in the power spectrum at $St_1 = 0.126$ (point 1) and at $St_2 = 0.124$ (point 2). The third spectrum in Figure 9a at $Re_D = 3.6 \times 10^5$ represents the critical state immediately prior to the jump into the supercritical range. The state of the flow has now changed from the *co-shedding regime* at point 1 with $C_{d_2} = 0.70$ via point 2, at which $C_{d_2} \approx 0$ and $S/D = S/D_{cr}$, to the *reattachment regime* in point 3 with $C_{d_2} = -0.24$. The spectrum shows two clear Strouhal-number peaks with nearly equal heights, the first one at $St_3 = 0.115$ corresponding to the subcritical flow state, and the second one at $St_3 = 0.212$ that belongs to the supercritical flow state. In the spectrum of point 4 in Figure 9a, which corresponds to $Re_D = 3.72 \times 10^5$, the jump into the supercritical range has just been completed. The main peak is now situated at a Strouhal number of $St_4 = 0.242$, and a secondary peak appears at the same position of the secondary peak in the power spectrum of point 3, hence, at $St_4 = 0.212$. For supercritical or low upper transition Reynolds numbers up to $Re_D = 1 \times 10^6$, each spectrum consists again of only one distinct peak at $St_L \approx 0.23$, as represented by point 5 in Figure 9a. The jump in the $St_{L_2}(Re_D)$ curve in Figure 8a from the supercritical into the transcritical flow regime, tak-

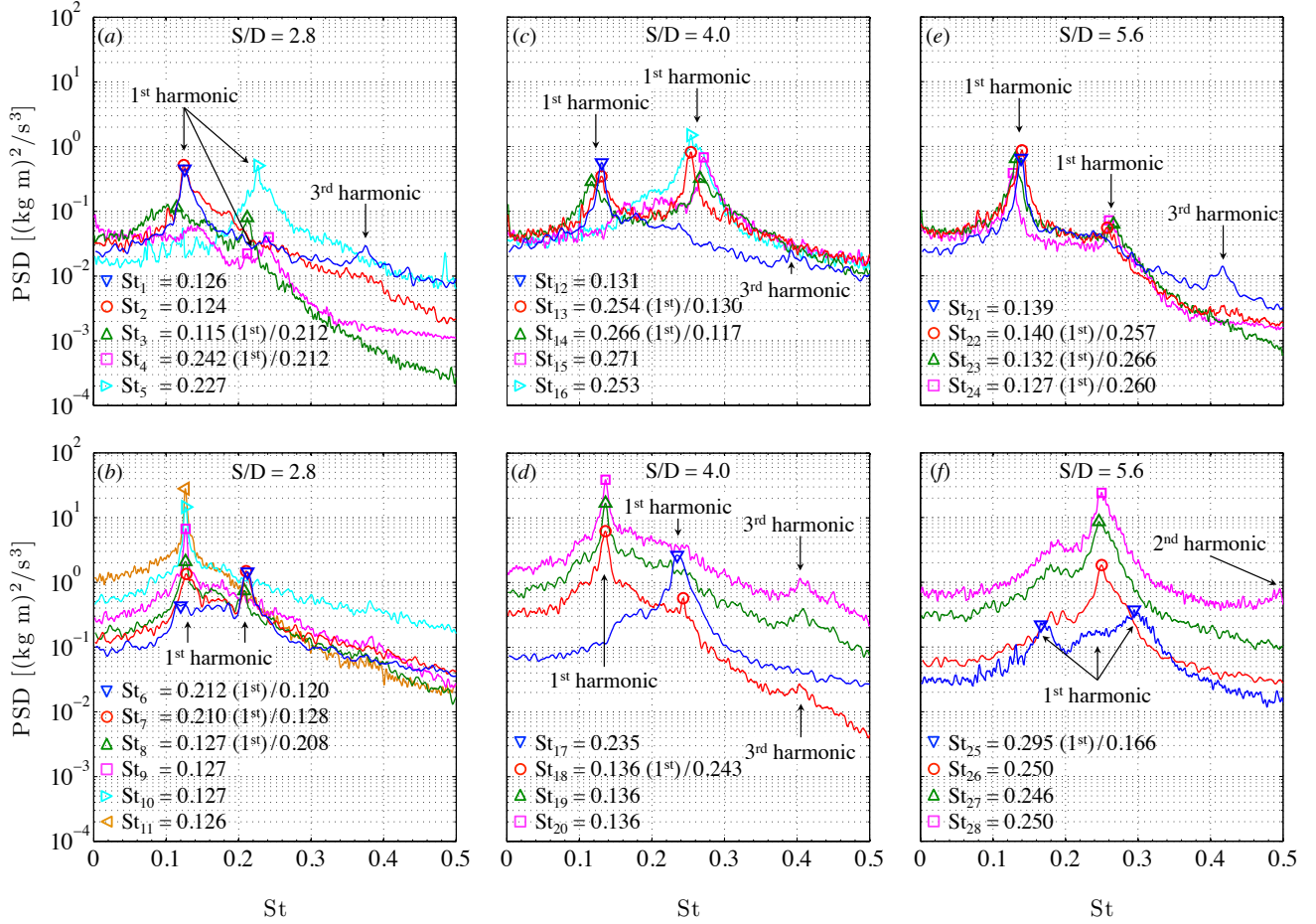


Figure 9: Power spectral density of the time series of the spanwise-integrated lift forces on the downstream prism at $\alpha = 0^\circ$ for selected Reynolds numbers. (a),(b): $S/D = 2.8$; (c),(d): $S/D = 4.0$; (e),(f): $S/D = 5.6$. The individual curves correspond to the points marked by the numbers 1 to 28 in Figure 4 and Appendix A1. In various flow states two peaks occurred in the power spectra at the same Reynolds number. The dominant Strouhal number is indicated by (1st), followed by the Strouhal number of the secondary peak.

ing place at Reynolds numbers of $1 - 1.68 \times 10^6$ within the upper transition, is once more accompanied with the simultaneous occurrence of two Strouhal numbers, see points 6 to 8 in Figure 9b. The most striking feature of these power spectra is the gradual change from the main peak to a secondary one and visa versa. It is evident that the higher frequency component, i.e., $St_{L_2} \approx 0.21$, dominates up to $Re \approx 1.5 \times 10^6$; thereafter, the lower frequency component predominates, i.e., $St_{L_2} = 0.127$. As the Reynolds number increases further up to $Re_D = 7.55 \times 10^6$, each spectrum consists once again of only a single narrow peak at $St_L = 0.127$, see points 9 to 11 in the Figure 9b. With the exception of both the broadness and height of the peaks, the shapes of these transcritical spectra resemble those at subcritical Reynolds numbers.

The centre and right column of Figure 9 show several spectra belonging to $S/D = 4.0$ and 5.6 . Most of these spectra correspond to the same Reynolds number regimes as their counterparts at $S/D = 2.8$ in the left column so that

the influence of the spacing can be seen directly. Except for the higher Strouhal number values at the larger spacing S/D , the shapes of the spectra in the various flow regimes are similar. At subcritical Reynolds numbers, the power spectra of the fluctuating lift coefficients possess a single dominant and relatively narrow peak, at $St_{12} = 0.131$ at $Re_D = 1.5 \times 10^5$ for $S/D = 4.0$ and at $St_{21} = 0.139$ at $Re_D = 1.5 \times 10^5$ for $S/D = 5.6$. Two Strouhal-number peaks appear once again in the power spectra for Reynolds number within the critical flow state. Similar to $S/D = 2.8$, the lower of the two Strouhal numbers belongs to the subcritical flow state and the higher peak corresponds to the supercritical flow state. For $S/D = 4.0$, both peaks in the power spectra that belong to the critical points 13 and 14 in Figure 9c have nearly equal heights. By contrast, for $S/D = 5.6$ the lower frequency component clearly dominates, as the peak of the higher frequency component is about one order of magnitude lower, see points 22 to 24 at $Re_D = 3.1 - 3.7 \times 10^5$ in Figure 9e. At this spacing, both peaks reach nearly equal heights only at the end of the critical flow state, as shown by the power spectrum belong-

ing to point 25 at $Re_D = 4.3 \times 10^5$. Within the supercritical flow regime, each spectrum consists once again of only one broad peak, see points 15 to 17 in the Figures 9c and 9d for $S/D = 4.0$ and points 26 to 28 in Figure 9f for $S/D = 5.6$. For the intermediate spacing, the cross-over from the supercritical into the transcritical flow regime, taking place around $Re_D = 1.9 \times 10^6$ (point 18 in Figure 9d), is characterised by the virtual complete disappearance of the peak in the power spectrum at the supercritical Strouhal number of $St_{18} = 0.243$ and the development of a new dominant peak at a significantly lower Strouhal number of $St_{18} = 0.136$ ($\approx St_{12}$). All spectra that belong to Reynolds number in the transcritical flow state consist then again of only one narrow peak at $St_L = 0.136$, see points 19 and 20 in Figure 9d.

4.2. Variation in prism-to-prism spacing for 45° angle of incidence

In the second measurement campaign the incidence angle of both tandem prisms was changed to $\alpha = 45^\circ$. The influence of the same three S/D -values between the two prisms at Reynolds numbers in the range of $Re_D = 1 \times 10^5 - 7 \times 10^6$ was investigated. In this way, the direct changes in the aerodynamic characteristics, induced solely by a change in angle of incidence, could clearly be examined and evaluated. The resultant distributions of the mean sectional drag, lift, pitch moment, and base pressure coefficients (C_d , C_l , C_m , C_{pb}) of both prisms, as well as the spanwise-integrated

fluctuating drag and lift coefficients ($\sqrt{\langle C_D'^2 \rangle}$, $\sqrt{\langle C_L'^2 \rangle}$) and the Strouhal number St_L of the downstream prism with increasing Reynolds number are presented for all three spacing values in the Figures 10 to 15. With regard to the behaviour of the flow around the two tandem prisms, drastic differences between $\alpha = 0^\circ$ and at $\alpha = 45^\circ$ are found. Independent of the spacing, the general trends are a strong increase in the sectional drag force of the upstream prism, as well as higher fluctuating lift and drag forces and lower Strouhal numbers for the downstream prism. At $S/D = 2.8$ and 4.0 , a stronger interference between both prisms occurs, mirrored by a thrust force on the downstream prism over all Reynolds-number regimes at $S/D = 2.8$ and large Reynolds-number ranges with $C_{d_2} \approx 0$ at $S/D = 4.0$. Compared to the results at $\alpha = 0^\circ$, the aerodynamic parameters of both prisms at $\alpha = 45^\circ$ show an increased Reynolds-number independency.

4.2.1. Mean and fluctuating aerodynamic loads

The curves in Figure 10 present the mean sectional drag coefficients $C_{d_{1,2}}$ experienced by each of the two prisms for Reynolds numbers from 1×10^5 up to $5.8 \times 10^6 - 7.4 \times 10^6$. Once again, the $C_d(Re_D)$ curve of a single rounded square-section prism (van Hinsberg, 2021a) has been included in each graph for comparison reasons. The letters that accompany each curve at selected Reynolds numbers are listed in the Appendices A3 and A4, together with the respective values of each of the measured aerodynamic parameters.

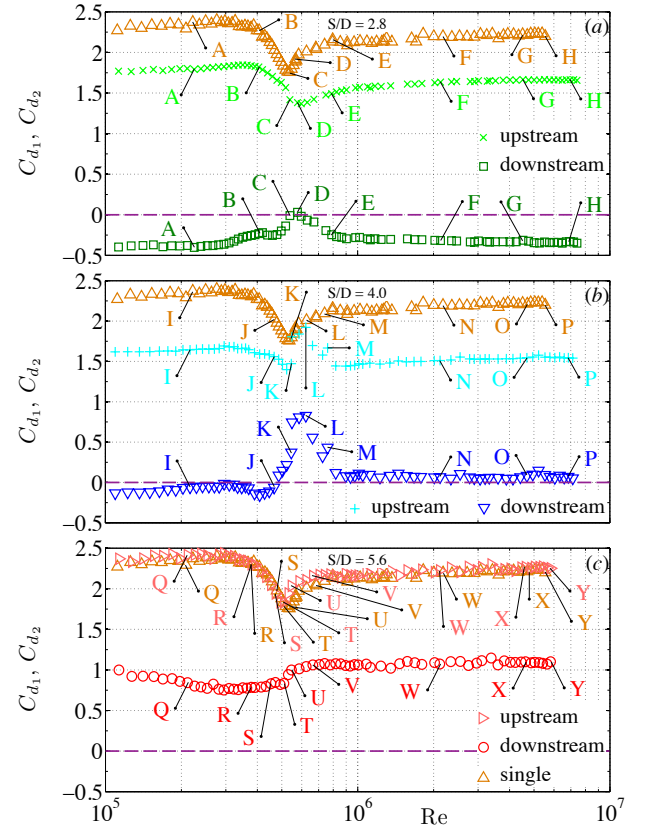


Figure 10: Sectional mean drag coefficient, C_d , as function of the Reynolds number Re_D for both tandem 2D square prisms with rounded edges of $r/D = 0.16$ at $\alpha = 45^\circ$. C_{d_1} : upstream prism; C_{d_2} : downstream prism. (a): $S/D = 2.8$, (b): $S/D = 4.0$, and (c): $S/D = 5.6$. \triangle : single isolated reference prism by van Hinsberg (2021a). The selected data points A to Y are listed in Appendices A3 and A4.

For each prism-to-prism spacing value, the appearance of the curve of the upstream prism at 45° angle of incidence, $C_{d_1}(Re_D)$, is for all flow regimes similar to the behaviour of the single prism. Hence, high constant values of C_{d_1} in the subcritical flow state, a moderate to steep decrease in the critical flow regime down to a global minimum at the critical Reynolds number at the end of this regime, a low constant value over a very short supercritical flow state, followed by a moderate recovery in the upper transition, and once again relatively constant values, lower than the subcritical ones, in the long transcritical flow regime. As can be observed in Figure 10, the only exception to this general trend of $C_{d_1}(Re_D)$ is the development of C_{d_1} in the upper transition for the intermediate spacing $S/D = 4.0$. For $S/D = 2.8$ and 5.6 , the upper transition is characterised by a smooth increase of the mean drag coefficient of the upstream prism with increasing Reynolds number and a levelling off towards a constant plateau that marks the transition into the transcritical flow regime; hence, the curves follow the trend in the upper transition known from a single smooth or (slightly) rough prism with a square cross-section and rounded edges (van Hinsberg et al., 2018; van

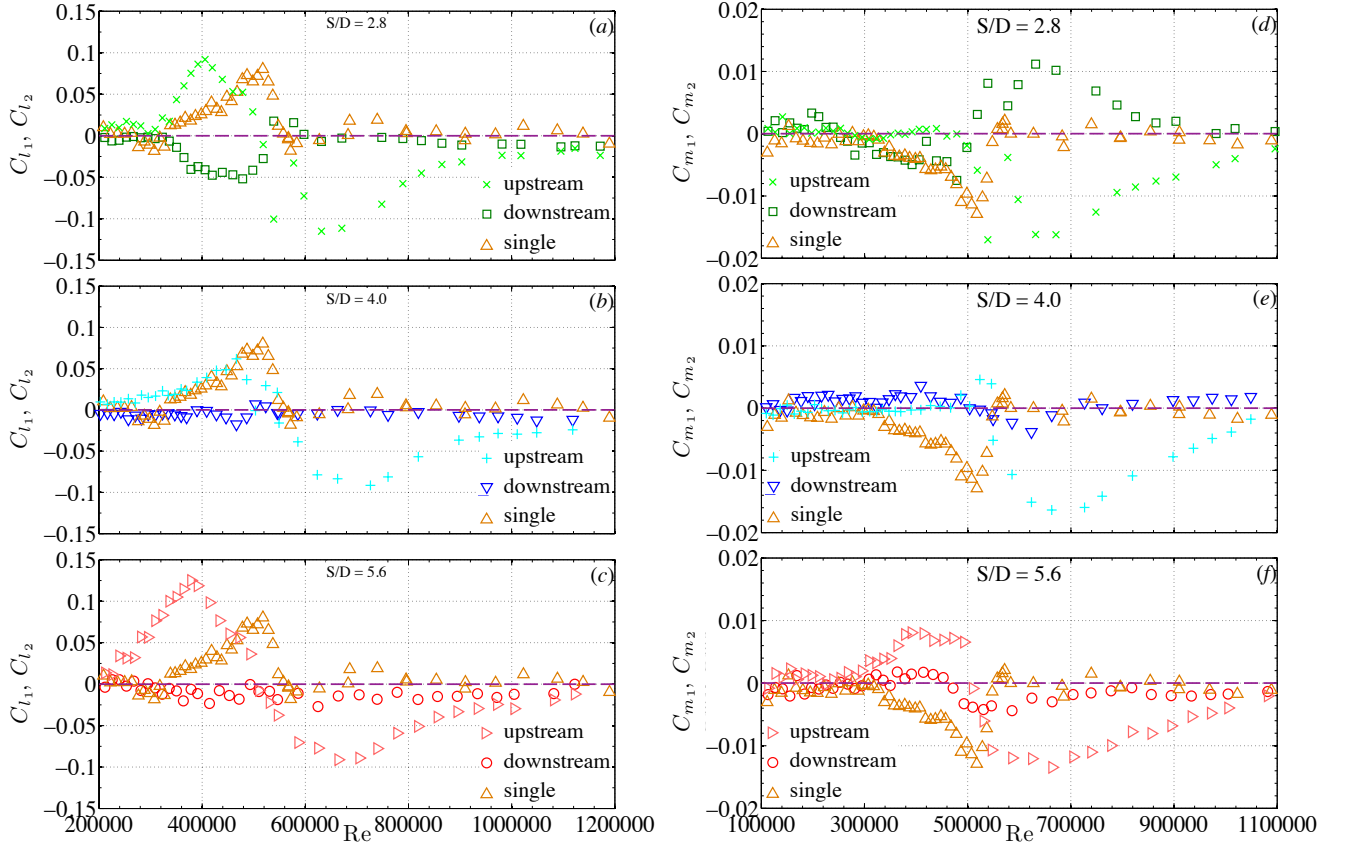


Figure 11: Dependency of the sectional mean lift (left column) and pitch moment (right column) coefficients on the Reynolds number for both tandem 2D square prisms with rounded edges of $r/D = 0.16$ at $\alpha = 45^\circ$. C_{l_1} and C_{m_1} : upstream prism; C_{l_2} and C_{m_2} : downstream prism. (a),(d): $S/D = 2.8$; (b),(e): $S/D = 4.0$; (c),(f): $S/D = 5.6$. \triangle : single isolated reference prism by van Hinsberg (2021a).

Hinsberg, 2021a). However, for $S/D = 4.0$, the upper transition begins with a step in the mean drag coefficient from $C_{d_1} = 1.47$ to $C_{d_1} = 1.81$ at $Re_D = 5.47 \times 10^5$, followed by a local maximum of $C_{d_1} = 1.92$ at $Re_D = 6.2 \times 10^5$ and a steady decrease down to $C_{d_1} = 1.44$ towards the end of the upper transition. Whereas for $S/D = 5.6$ the values of C_{d_1} and $C_{d_{single}}$ in the individual flow regimes match very well, lower mean drag forces than those of the single prism are experienced by the upstream prism for $S/D = 2.8$ and 4.0 . Solely based on its mean drag values, the upstream prism at $S/D = 5.6$ could thus be treated as being equivalent to a single prism in cross-flow, a similar conclusion that was also drawn from Figure 4 at the same spacing, but at an angle of incidence of $\alpha = 0^\circ$.

The curves of the mean sectional lift and pitch moment coefficients of the upstream prism then again show quite a different behaviour with increasing Reynolds number compared to the results for a single prism at all three spacing values in Figure 11. This illustrates that the flow around the upstream prism at 45° incidence angle is clearly modified by the presence of an equal prism further downstream. Both aerodynamic coefficients are zero or near zero at subcritical and transcritical Reynolds numbers. Between these two extreme flow states, the three $C_{l_1}(Re_D)$ curves in the

Figures 11a to 11c show equal characteristics: a gentle hill that covers the complete critical flow state with a global maximum at $C_{l_1} = 0.06 - 0.13$, its exact value dependent on the spacing S/D , and a broad valley in the upper transition, whose lowest point lies around $C_{l_1} \approx -0.1$. These two flow regimes are divided by a single supercritical point with $C_{l_1} \approx 0$ at $Re_D = 5.78 \times 10^5$ for $S/D = 2.8$, at $Re_D = 5.46 \times 10^5$ for $S/D = 4.0$, and at $Re_D = 5.10 \times 10^5$ for $S/D = 5.6$. At all three S/D -values, the mean pitch moment coefficient of the upstream prism C_{m_1} , presented in the right column of Figure 11, shows in the upper transition a very similar development with increasing Reynolds number as obtained for C_{l_1} ; the same counts for the part of the $C_{m_1}(Re_D)$ curve that belongs to the critical flow state at the largest spacing $S/D = 5.6$. For both smaller spacing values, the pitch moment coefficient remains close to zero at low to medium critical Reynolds numbers and experiences near the end of this flow regime either a relatively small bump with a local maximum of $C_{m_1} = 0.005$ ($S/D = 4.0$) or a steep decrease towards a global absolute negative maximum of $C_{m_1} = -0.017$ ($S/D = 2.8$).

For all three tandem prism configurations, the appearance of the $C_{d_2}(Re_D)$ curve for the downstream prism at

45° angle of incidence, presented in Figure 10, strongly differs from the behaviour of both C_{d_1} and $C_{d_{single}}$, as well as of its counterpart at $\alpha = 0^\circ$ in Figure 4. The development of C_{d_2} is for the smallest spacing the inverse to that of the upstream one. The downstream prism experiences a thrust force at almost all Reynolds numbers. Nearly constant negative values for C_{d_2} are obtained at subcritical Reynolds numbers of $Re_D \leq 3 \times 10^5$ and in the complete transcritical flow state for $Re_D \geq 9.8 \times 10^5$. In between those two outer ranges, C_{d_2} clearly depends on the Reynolds number. Only at the supercritical Reynolds number and in its direct vicinity a net mean drag force of about zero is obtained; hence, at these Reynolds numbers the spacing $S/D = 2.8$ is equivalent to the critical spacing S/D_{cr} . The corresponding mean sectional lift and pitch moment coefficients in the Figures 11a and 11d are approximately zero over large ranges of the Reynolds number. Small negative values of C_{l_2} up to a maximum of $C_{l_2} = -0.05$ appear in the critical flow state only. The downstream prism experiences a steady non-zero pitch moment in exactly the same Reynolds-number range for which a variation in the mean drag coefficient C_{d_2} with increasing Reynolds number was observed as well. Within this range, a sign inversion of C_{m_2} from negative to positive occurs at approximately $Re_D = 5 \times 10^5$.

An increase of the spacing induces a shift of the $C_{d_2}(Re_D)$ curve towards positive values. Whereas a change from S/D from 2.8 to 4.0 has hardly any influence on the general trend of the curve, a further increase to $S/D = 5.6$ leads to a strong flattening of the curve and in particular in the critical, supercritical, and upper transition flow regimes an increased independency of C_{d_2} on the Reynolds number is obtained. For the tandem configuration with the intermediate spacing $S/D = 4.0$, the complete subcritical and the first part of the critical flow state are characterised by low negative mean drag coefficients. At these Reynolds numbers, the state of the flow around both prisms belongs to the *reattachment regime (mode I)*, for which proximity interference effects are dominant, a vortex street is formed behind the downstream prism only, and the spacing $S/D = 4.0$ thus lies below the critical spacing S/D_{cr} . At approximately $Re_D = 4.7 \times 10^5$ the sign of C_{d_2} switches from negative to positive and the flow state changes from *mode I* to *mode II*, hence, the *co-shedding regime* with $S/D > S/D_{cr}$, and remains in this flow state up to the highest measured Reynolds number of $Re_D = 7.13 \times 10^6$. Up to the end of the upper transition at $Re_D = 9.0 \times 10^5$, the mean drag force on the downstream prism experiences a sharp increase to $C_{d_2} = 0.83$ at $Re_D = 6.2 \times 10^5$ - combined with a jump in C_{d_2} of $\Delta C_{d_2} = 0.37$ at the supercritical Reynolds number $Re_D = 5.46 \times 10^5$ - followed by a steady decrease down to $C_{d_2} = 0.08$ at $Re_D = 9.0 \times 10^5$. Approximately constant values of the mean drag coefficient of $C_{d_2} = 0.05$ - 0.11 are obtained for all transcritical Reynolds numbers. As mentioned previously, the development of C_{d_2} is at the largest spacing $S/D = 5.6$ only weakly dependent on the Reynolds number and the state of the flow equals the *co-*

shedding regime in all Reynolds-number flow regimes. After a mild decrease in the subcritical flow regime from $C_{d_2} = 1.00$ at $Re_D = 1.1 \times 10^5$ to $C_{d_2} = 0.80$ at 2.3×10^5 , the mean drag coefficient remains at a plateau of $C_{d_2} \approx 0.78$ in the critical flow regime. In the supercritical flow regime, which is represented by a single point at $Re_D = 5.1 \times 10^5$, a step with a height of $\Delta C_{d_2} = 0.11$ occurs. The $C_{d_2}(Re_D)$ curve levels off in the upper transition to a new plateau at $C_{d_2} = 1.10$ that lasts up to high transcritical Reynolds numbers.

The mean lift and pitch moment coefficients of the downstream prism at $S/D = 4.0$ and 5.6 are practically zero at most Reynolds-number flow regimes. The respective graphs of C_{m_2} in the Figures 11e and 11f show only small variations with the Reynolds number in the critical, supercritical, and upper transition flow regimes; these fluctuations correlate well with the behaviour of the mean pitch moment coefficient of the upstream prism C_{m_1} presented in the same graphs.

The fluctuating lift and drag forces on the downstream prism, $\sqrt{(C'_L)^2}_2$ and $\sqrt{(C'_D)^2}_2$, are presented in Figure 12, together with the values by van Hinsberg (2021a) for a single rounded, square-section prism. We recall once more, that these data were obtained using piezoelectric platform dynamometers; hence, they result from spanwise-integrated force measurements on the entire downstream prism.

Both parameters show an inverse trend with increasing prism-to-prism spacing: whereas for larger S/D -values the RMS values of the fluctuating drag on the downstream prism converge to those of the single prism, an increasing deviation is observed for the RMS values of the fluctuating lift force. At a spacing of $S/D = 2.8$, both the trend of the $\sqrt{(C'_L)^2}_2(Re_D)$ curve and the individual RMS values of the fluctuating lift force in Figure 12a coincide very well with the single prism data. In contrast, for the same spacing, a relatively good agreement between the RMS values of the fluctuating drag force of the downstream prism and those of the single prism only exists over a small part within the critical flow state and at the supercritical Reynolds number of $Re_D = 5.78 \times 10^5$ (Figure 12d). At all other flow regimes, lower fluctuating drag values are obtained for the downstream prism. Since those values show only small variations with the Reynolds number, deviations as large as 90% and 35% occur at subcritical and transcritical Reynolds numbers, respectively, with respect to the single prism data. Interestingly, at the largest spacing $S/D = 5.6$, the exact opposite situation is observed: a relatively good match between the RMS values of the fluctuating drag force of the downstream prism and those of its single counterpart in Figure 12f, and RMS values of the fluctuating lift force on the downstream prism that are approximately twice as high as those for the single prism (Figure 12c). Similar to $S/D = 2.8$, the RMS values of the fluctuating drag force are largely Reynolds-number independent over all flow regimes at $S/D = 5.6$ as well. Interestingly, the same counts for

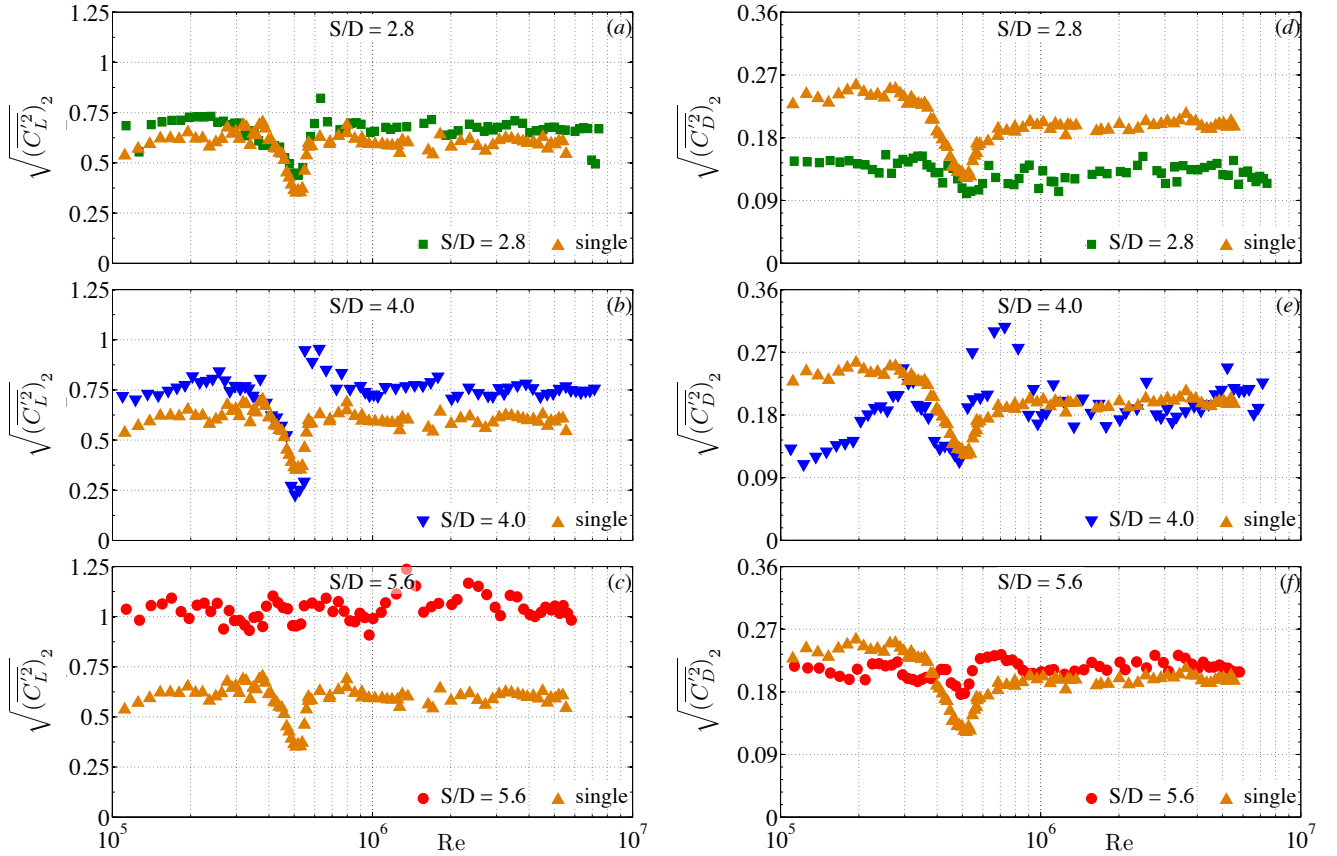


Figure 12: Global (spanwise-integrated) fluctuating lift (left column) and drag (right column) coefficients as function of the Reynolds number for the downstream 2D square prism with rounded edges of $r/D = 0.16$ at $\alpha = 45^\circ$. (a),(d): $S/D = 2.8$; (b),(e): $S/D = 4.0$; (c),(f): $S/D = 5.6$. \blacktriangle : single isolated reference prism by van Hinsberg (2021a).

the fluctuating lift force at $S/D = 5.6$. At the intermediate spacing $S/D = 4.0$, the development of both the $\sqrt{(C_L')_2}(Re_D)$ curve and the $\sqrt{(C_D')_2}(Re_D)$ curve possess characteristics of the curves for the other two spacing values. Hence, the curve of the fluctuating lift force in Figure 12b follows relatively well the curve of the single prism; the actual values for the downstream prism are about 30% higher though. An exception is the critical flow state, for which then again a very good match between both curves is obtained. Furthermore, at $Re_D = 4.7 \times 10^5$ in the critical flow state and at the supercritical Reynolds number of $Re_D = 5.46$, the data reveal a large step of $\Delta\sqrt{(C_L')_2} = -0.27$ and $\Delta\sqrt{(C_L')_2} = +0.66$, respectively. A fairly good agreement between the RMS values of the fluctuating drag force on the downstream prism at $S/D = 4.0$ and those on the single prism appear at most critical and transcritical Reynolds numbers, whereas moderate to large deviations between both curves occur in the other three flow regimes (Figure 12e). In addition, the curve is characterised by sudden jumps in $\sqrt{(C_D')_2}$ with various heights at multiple Reynolds numbers in the various flow regimes.

4.2.2. Mean base pressure coefficient

The development of the mean sectional base pressure coefficient of the two tandem prisms, $C_{pb_{1,2}}$, with increasing Reynolds number is shown in Figure 13 for each spacing, together with the data for the single prism, $C_{pb_{single}}$, by van Hinsberg (2021a).

As expected, each $C_{pb_{1,2}}(Re_D)$ curve shows a similar behaviour as the corresponding mean sectional drag curve $C_{d_{1,2}}(Re_D)$ in Figure 10. This correlation between both coefficients is somewhat more pronounced for the upstream prism. In particular at the smallest spacing, the dip in the mean base pressure curve of the downstream prism in the Reynolds-number range that covers the critical up to the upper transition flow regime is much weaker compared to the dip in the corresponding $C_{d_2}(Re_D)$ curve that appears in the same range of Reynolds numbers in Figure 10a. Hence, for this spacing the downstream prism experiences an almost constant base pressure of $C_{pb_2} = -0.68$ throughout the various flow regimes. The absolute values of C_{pb_2} are for $S/D = 2.8$ and 4.0 significantly lower than the values of the single prism at equal Reynolds number (Figures 13a and 13b). The interference effects between both prisms for those two spacing values, i.e. the occurrence of an inverse (hence, thrust) or near-zero net drag force on the down-

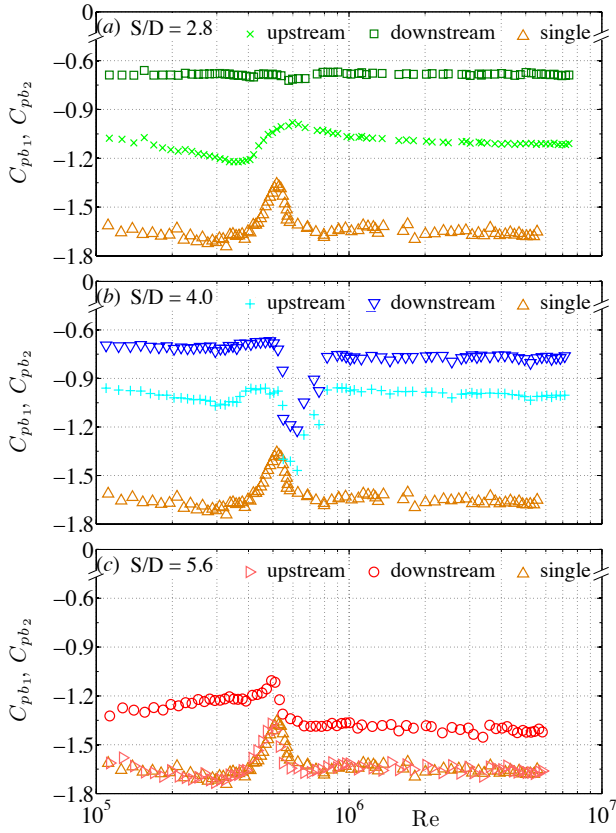


Figure 13: Mean base coefficient, C_{pb} , as function of the Reynolds number Re_D for both tandem 2D square prisms with rounded edges of $r/D = 0.16$ at $\alpha = 45^\circ$. C_{pb_1} : upstream prism; C_{pb_2} : downstream prism. (a): $S/D = 2.8$, (b): $S/D = 4.0$, and (c): $S/D = 5.6$. \triangle : single isolated reference prism by van Hinsberg (2021a).

stream prism, is reflected in a distinct decrease in the mean suction pressure at the base of the upstream prism compared to the single prism. The nearly perfect match between C_{pb_1} and $C_{pb_{single}}$ in combination with an approach of the $C_{pb_2}(Re_D)$ curve towards both other curves for $S/D = 5.6$ in Figure 13c reveals a strong reduction of the mutual interference between both tandem prisms at this spacing.

4.2.3. Power spectra and Strouhal numbers

Figure 14 presents multiple power spectra of the fluctuating lift coefficient $C_{L_2}(t)$ that acts on the downstream one of both tandem prisms at all three S/D -values. The letters A to Y in Figure 10 assign each power spectrum to their respective Reynolds number and corresponding flow regime.

With the exception of point K, all spectra of the lift fluctuations are characterised by one sharp peak at the non-dimensional fundamental frequency, hence, first harmonic, that represents the main vortex-shedding frequency. Where applicable, the peaks of the second and/or third harmonics – with heights that are at least one order of magnitude lower than those of the first harmonic – have been tagged as well. Four interesting features can be deduced from

these graphs. First of all, an increase in the spacing between the centres of both prisms from $S/D = 2.8$ to 4.0 does not lead to any significant change in the positions of the first and third harmonics. Exceptions are the secondary peak in the curve K at the supercritical Reynolds number $Re_D = 5.5 \times 10^5$ in Figure 14c and the peaks of the first and third harmonics in the curves L and M that belong to Reynolds numbers in the upper transition (Figures 14c and 14d). In both flow regimes, the peaks for $S/D = 4.0$ wander to somewhat higher non-dimensional frequencies compared to the values in the same flow regimes, but for the smallest spacing of $S/D = 2.8$. A further increase in spacing to $S/D = 5.6$ results then again in an overall shift of the fundamental frequency towards higher values at all Reynolds numbers. Second, for both the smallest and the largest spacing, the position of the peak of the fundamental frequency remains practically unchanged, regardless of the Reynolds number. As mentioned previously, for the intermediate spacing $S/D = 4.0$ a wandering of the peaks in the power spectrum occurs in a small range of Reynolds numbers that covers the supercritical flow state and the upper transition. Similar to $S/D = 2.8$ and 5.6, an increase in the Reynolds number in the other flow regimes at $S/D = 4.0$ does not lead to a significant change in the non-dimensional frequency of the first and third harmonics. Third, the data in Figure 14 show that only within one single spectrum, at the supercritical point K for $S/D = 4.0$, two Strouhal number peaks with slightly different heights appear, at $St_K = 0.112$ and 0.144. Last, but not least, it is interesting to note that the transformation of the two last spectra at $S/D = 4.0$ (hence, points O and P at $Re_D = 4.69 \times 10^6$ and $Re_D = 6.85 \times 10^6$, respectively) in Figure 14d does not seem to have completed yet. Besides the peak characteristics that belong to the transcritical Reynolds-number regime, a new peak at approximately $St_L = 0.13$ is probably just about to be formed at those high Reynolds numbers.

The Strouhal numbers that are based on the main frequency in the PSDs are presented in Figure 15 as function of the Reynolds number. At each spacing, the appearance of the curve coincides well with the Strouhal-number curve that belongs to the single prism. However, large differences in the actual values of the Strouhal numbers between the downstream and the single prism can be observed for $S/D = 2.8$ and 4.0. They appear in exactly those Reynolds-number regimes, in which the mean sectional drag coefficient on the downstream prism, C_{d_2} , is negative or near-zero, see the Figures 10a and 10b in section 4.2.1. In contrast, for Reynolds numbers that lie inside the range spanned from the upper critical regime up to the end of the upper transition, relatively large positive values of C_{d_2} were obtained for the intermediate spacing. The graph in Figure 15b shows that exactly at those Reynolds numbers a fairly good match between St_{L_2} and $St_{L_{single}}$ is present. For the largest of the three spacing values, an almost perfect agreement between the Strouhal numbers of the downstream prism and those of the single prism is found.

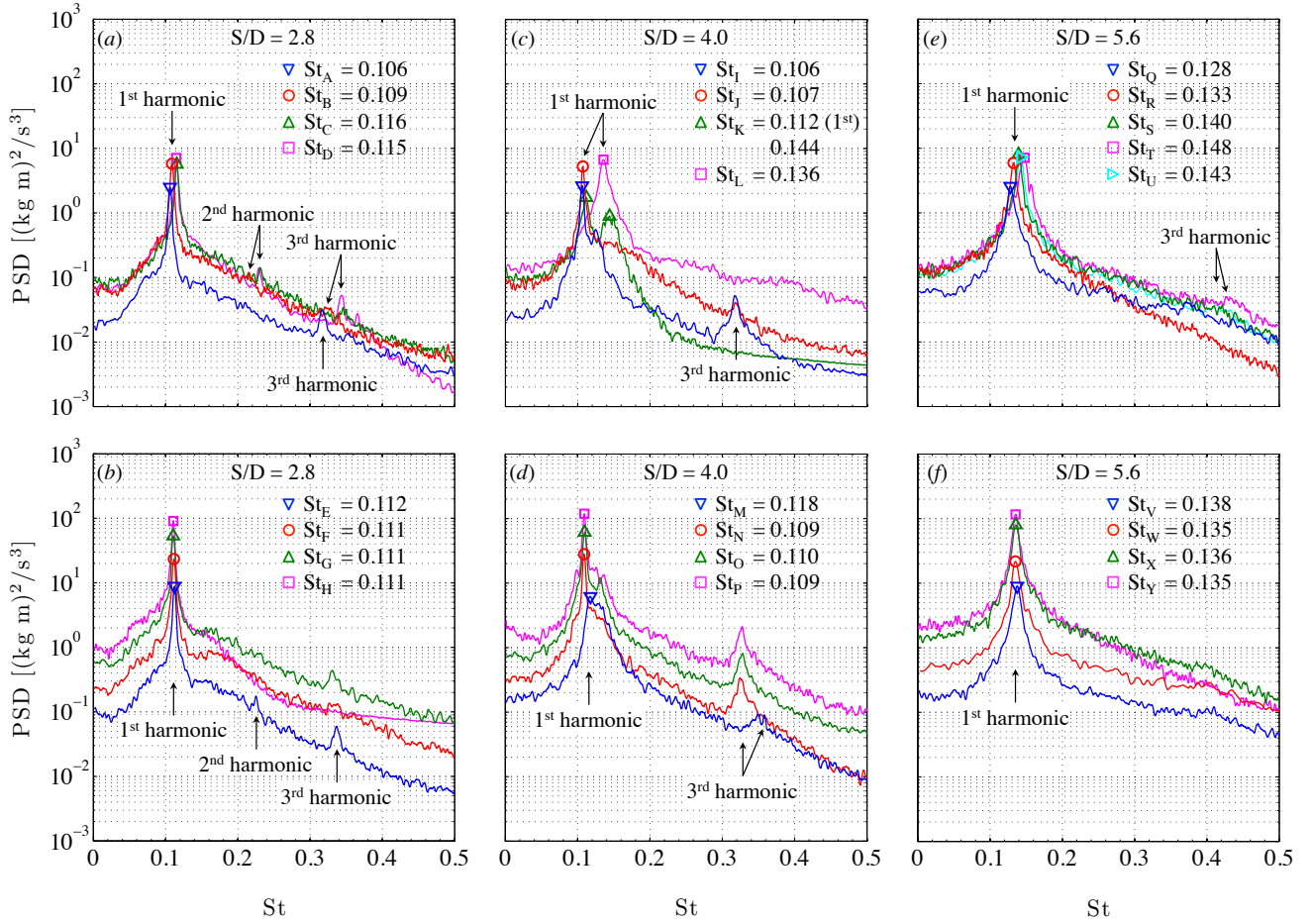


Figure 14: Power spectral density of the time series of the spanwise-integrated lift forces on the downstream prism at $\alpha = 45^\circ$ for selected Reynolds numbers. (a),(b): $S/D = 2.8$; (c),(d): $S/D = 4.0$; (e),(f): $S/D = 5.6$. The individual curves correspond to the points marked by the numbers A to Y in Figure 10 and Appendix A3. At point K ($S/D = 4.0$) two peaks occurred in the power spectrum. The dominant Strouhal number is indicated by (1^{st}), followed by the Strouhal number of the secondary peak.

5. Discussion

The results that were presented in the preceding section have shown that the centre-to-centre spacing between the two tandem prisms, the Reynolds number, and the angle of incidence of both prisms each induce distinct and partly completely different effects on the mean and fluctuating loads on the two tandem square prisms with rounded edges of $r/D = 0.16$.

Both for $\alpha = 0^\circ$ and 45° , a larger spacing between the two tandem prisms leads to a reduction of the interference effects. The results in Figure 4 for $\alpha = 0^\circ$ showed that a negative drag force on the downstream prism, i.e., *mode I*, appears only in a small Reynolds-number range within the subcritical and critical flow regime for $S/D = 2.8$. For the two other spacing values, the drag force on each prism is positive at all Reynolds numbers; the flow state belongs in those two cases thus to *mode II*. On the contrary, at an angle of incidence of 45° a thrust force is experienced by the downstream prism over all Reynolds-number regimes at $S/D = 2.8$ (Figure 10). At equal angle of incidence, even for the spacing $S/D = 4.0$ there exists a large Reynolds-

number range with small negative or near-zero values of C_{d2} . The mean drag (Figure 10) and base pressure (Figure 13) coefficients of both prisms, as well as the sectional mean lift and pitch moment coefficients in Figure 11, the fluctuations in lift and drag (Figure 12) and the Strouhal number (Figure 15) of the downstream prism all become increasingly independent of the Reynolds number for larger spacing values at $\alpha = 45^\circ$. This behaviour then again stands in strong contrast to the trends of the curves of the same aerodynamic parameters at $\alpha = 0^\circ$, as at this latter angle of incidence a large variation in the values with the Reynolds number is obtained for all three spacing values.

Since no flow visualisation was performed in the current study, we have no detailed information on the wake structures around and behind both prisms, particularly for the critical up to the transcritical Reynolds number ranges. Nevertheless, we present hereafter ideas on how the flow field could look like, based on the behaviour of the surface pressure distributions on both prisms, the values of the various aerodynamic coefficients, and the non-dimensional frequency and strength of the vortices shed in the wake of

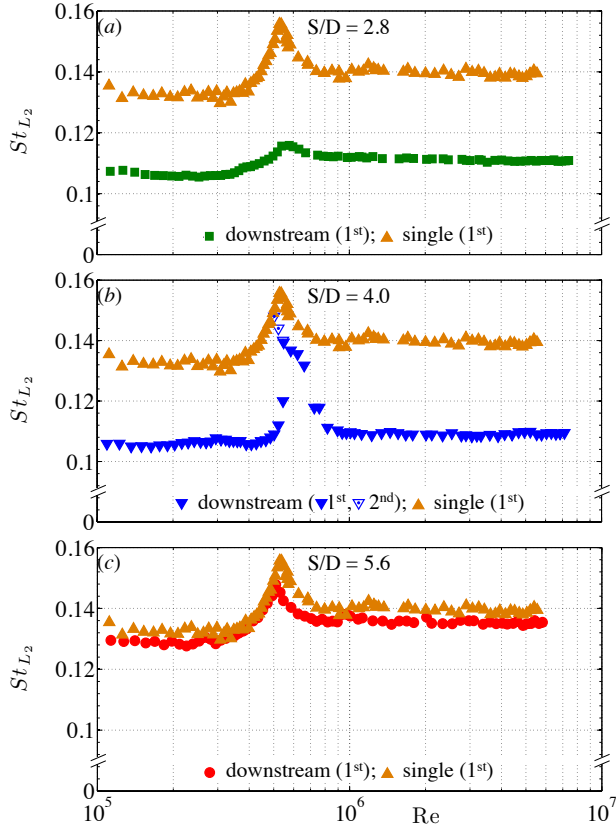


Figure 15: Strouhal numbers obtained from the fluctuating lift forces acting on the downstream prism at $\alpha = 45^\circ$ as function of the Reynolds number and the spacing. (a): $S/D = 2.8$, (b): $S/D = 4.0$, and (c): $S/D = 5.6$. \blacktriangle : single isolated reference prism by van Hinsberg (2021a). At $S/D = 4.0$ two peaks occurred in the power spectrum at the same supercritical Reynolds number. The dominant Strouhal number is indicated by a filled symbol, whereas a dot within the symbol belongs to the secondary peak.

the downstream prism.

In general, the changes in the flow phenomena around the tandem configuration with varying Reynolds number and spacing at both angles of incidence are induced by the behaviour of both the boundary layer on the surface of the two prisms, the free shear layers that separate from each prism, and the interaction of the free shear layer from the upstream prism with the boundary layer on the surface of the downstream prism. A very prominent role play in particular the locations of the transition from laminar to turbulent, either occurring on the surface of each prism or on the free shear layers, and the locations of the boundary layer primary separations from the surface. Depending on the Reynolds number, a reattachment of the free shear layers onto one or both side surfaces of the prism can take place as well; hence, the reattachment location(s), i.e. the length(s) of the separation bubble(s), and the secondary separation point(s) of the attached turbulent boundary layer are for that case remarkable influencing parameters as well. Details on the development of the laminar/turbulent transition loca-

tions and separation bubbles on the surface of the single rounded square-section prism in the subcritical up to transcritical flow regimes were already presented by the author in van Hinsberg (2021a).

5.1. Effects of Reynolds number and spacing on the pressure distribution at 0° incidence angle

The Figures 16 and 17 give an overview of the mean surface pressure distributions on both tandem prisms at selective Reynolds numbers that belong to the various flow states. The first of these two figures presents the quantitative distribution of the mean surface pressure coefficient $C_{p,cyl}$ as function of the non-dimensional circumferential distance s/D along the peripheral of each of the two tandem prisms (see Figure 3) for the Reynolds numbers that correspond to the numbers 1 to 28 in Figure 4 and in the Appendix A1. Hence, it allows a direct comparison between $C_{p,cyl}(s/D)$ of the upstream (left column) and of the downstream (centre column) prism at equal Reynolds numbers for all three spacing values. To get the complete picture of the mutual interference between both tandem prisms as a result of proximity effects, the surface pressures on the single prism with equal non-dimensional surface roughness values are shown at approximately the same Reynolds numbers in the right column of this figure (see Appendix A2 for a complete listing). Figure 17 gives an additional qualitative impression of the mean surface pressure distribution on both tandem prisms by means of a scaled vectorial representation. In contrast to Figure 16, only the pressure distributions for those Reynolds numbers are shown that give a clear impression of the changes in the surface pressure between the various flow regimes. The numbers inside the prisms correspond to those in the Figures 4 and 16. In addition, the values of the mean drag, lift, and pitch moment coefficients at those Reynolds numbers are also listed inside the individual graphs.

5.1.1. Subcritical flow state

Starting with the smallest prism-to-prism distance of $S/D = 2.8$ at $\alpha_{1,2} = 0^\circ$ in the left column of Figure 16, the attached boundary layer on the front surface of the upstream prism is laminar at point 1 ($Re_D = 1.5 \times 10^5$, hence, low subcritical) and separates at the forward directed rounded edges between the surfaces I and II and the surfaces I and IV of the prism. As a consequence, a relatively strong deflection of the streamlines and a distinct downstream spreading of the free shear layers in lateral direction occur. Both side surfaces II and IV, as well as the base surface III of the upstream prism, experience relatively constant negative mean pressures of $C_{p,cyl} = -1.31$ and $C_{pb_1} = -1.13$, respectively, see the Figures 16a and 17a. The large mean suction pressure on the rear surface, in combination with a symmetric mean pressure distribution with respect to the virtual horizontal line through $s/D = 0.47$ and 2.33, results in a high mean drag coefficient of $C_{d_1} = 1.47$, as well as a near-zero mean lift and pitch moment coefficient of

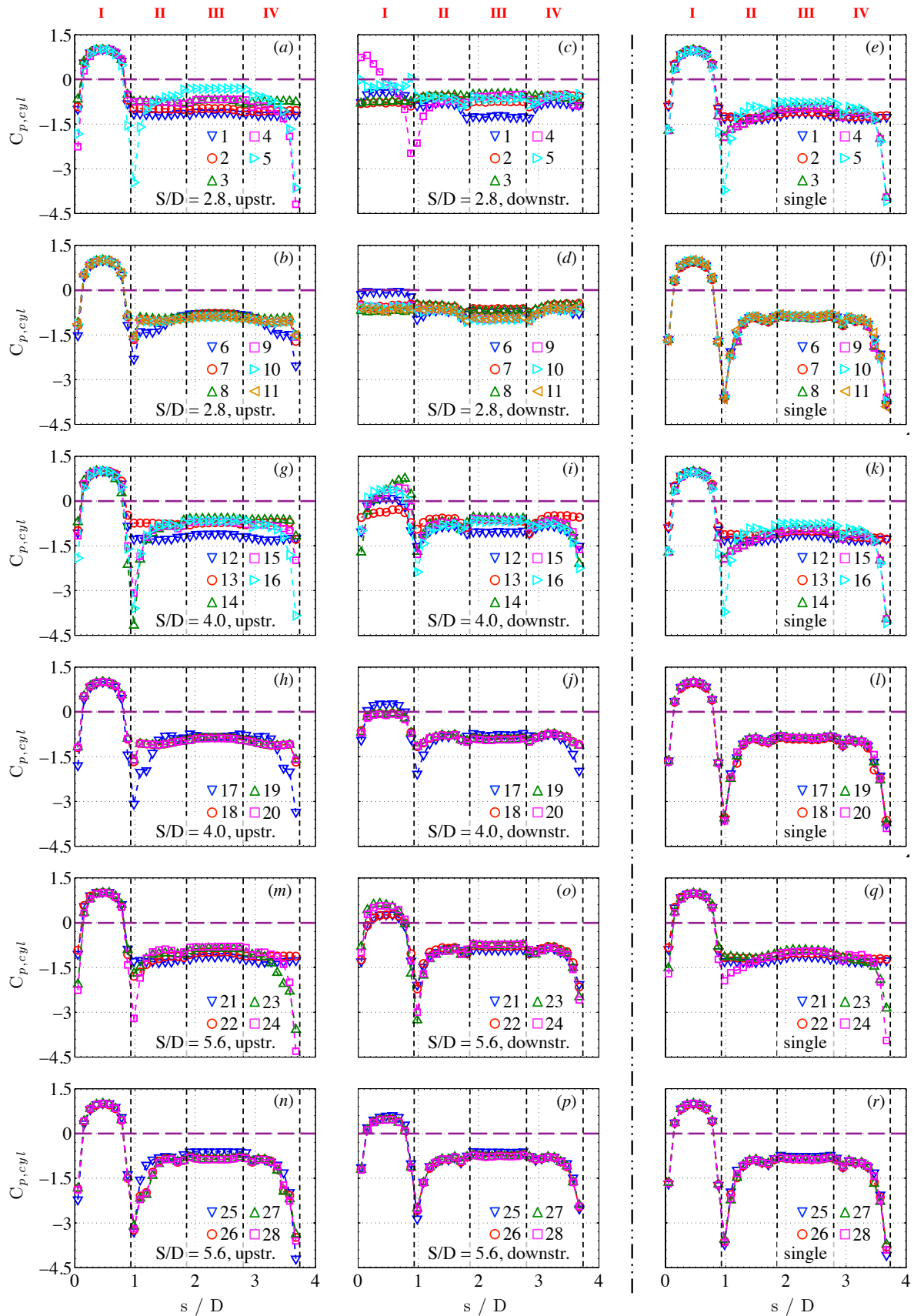


Figure 16: Quantitative representation of the mean circumferential surface pressure distributions at mid-span of the upstream (left column) and downstream (right column) tandem prism, as well as of the single prism (right column) by van Hinsberg (2021a), at $\alpha = 0^\circ$. (a)-(d): $S/D = 2.8$; (g)-(j): $S/D = 4.0$; (m)-(p): $S/D = 5.6$. The individual curves correspond to the points marked by the numbers 1 to 28 in Figure 4 and in the Appendices A1 and A2.

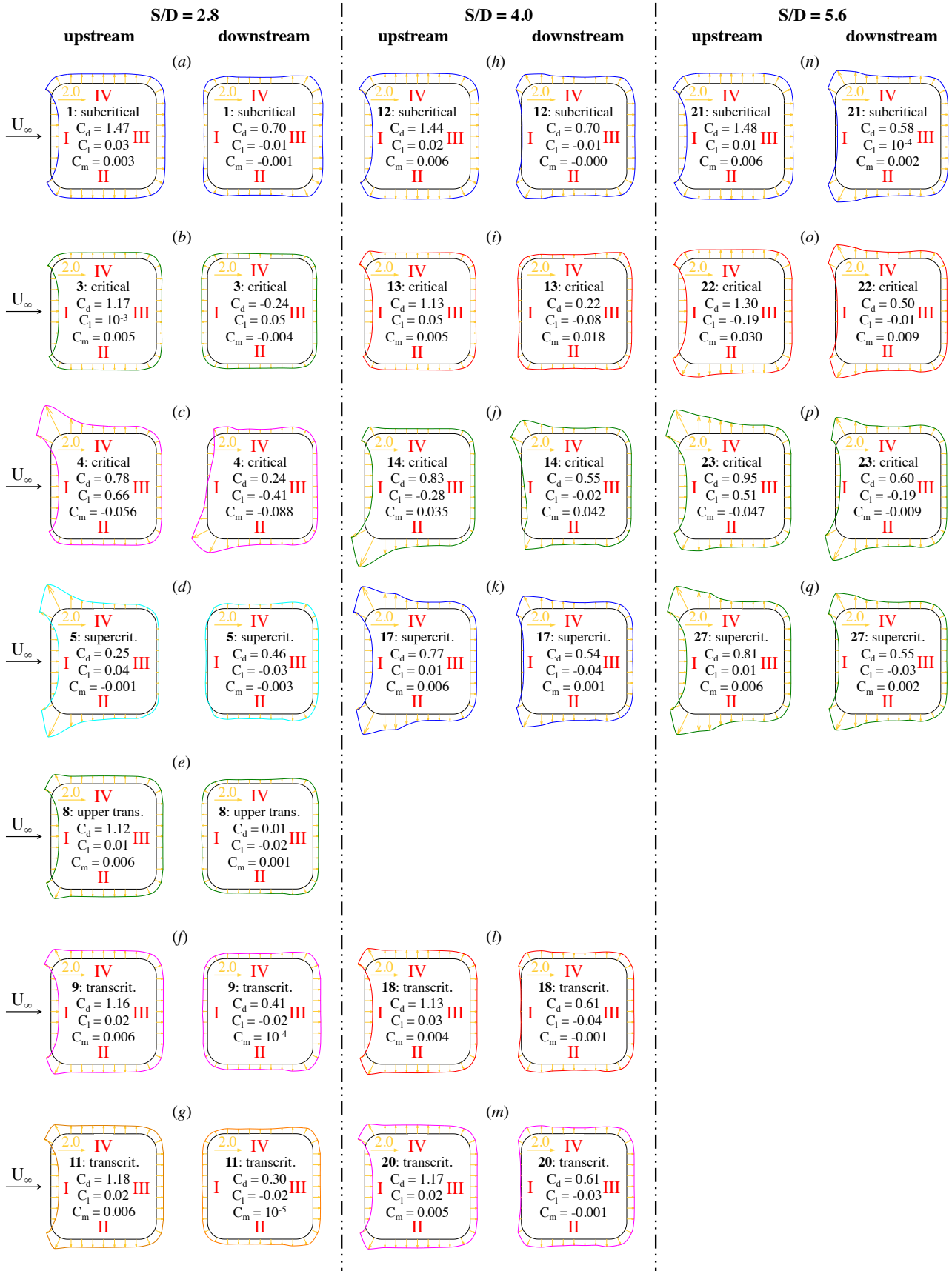


Figure 17: Qualitative scaled vectorial representation of the mean circumferential surface pressure distributions at mid-span of both tandem prisms at $\alpha = 0^\circ$. Left column: $S/D = 2.8$; centre column: $S/D = 4.0$; right column: $S/D = 5.6$. The numbers inside the individual graphs correspond to the points marked in Figure 4 and 16 and in the Appendices A1 and A2.

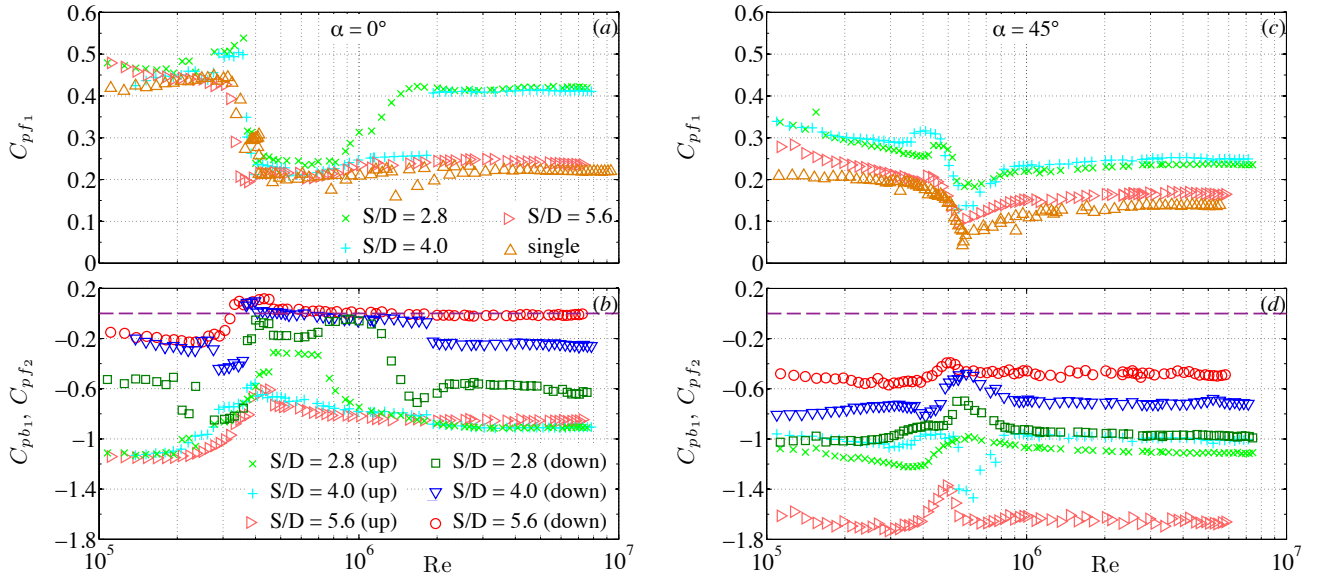


Figure 18: Average surface pressure coefficient on the forward directed surface I for $\alpha = 0^\circ$ and the surfaces I and II for $\alpha = 45^\circ$ of the upstream and downstream tandem prism and the mean base pressure coefficient of the upstream prism as function of the Reynolds number and spacing. C_{p,f_1} and C_{p,b_1} : upstream prism; C_{p,f_2} : downstream prism. (a),(b): $\alpha = 0^\circ$; (c),(d): $\alpha = 45^\circ$. \triangle : single reference prism by van Hinsberg (2021a).

$C_{l_1} = 0.03$ and $C_{m_1} = -0.003$. These values match well with those obtained for the single prism, see Figure 16a and 16c. For $Re_D \leq 2.0 \times 10^5$ the free shear layers that have separated from the upstream prism interact with the downstream prism, the flow around both tandem prisms at this spacing can hence be assigned to the *co-shedding regime (mode II)*. This process of free shear interaction is supported by the Figures 18a and 18b, which present the variation of the average surface pressure coefficient on the front surface I of both the upstream and downstream prism, C_{p,f_1} and C_{p,f_2} , and C_{p,b_1} as function of the Reynolds number at 0° angle of incidence. The coefficients C_{p,f_1} and C_{p,f_2} were calculated by averaging the pressures at all nine tap locations on surface I , i.e. between $s/D = 0.05$ and $s/D = 0.88$. Whereas for $Re_D \leq 2.0 \times 10^5$ the values of C_{p,f_1} are positive, i.e., $C_{p,f_1} = 0.45$ to 0.48 , the downstream prism experiences negative values of $C_{p,f_2} = -0.51$ to -0.57 . This latter suction pressure suggests a clear interaction between the downstream prism and the free shear layers coming from the upstream prism. Additional optical measurements techniques, like PIV or smoke visualisation, would be required to give more detailed information on the exact manner of interaction taking place. The resultant mean drag force of $C_{d_2} \approx 0.7$ is still positive, but clearly lower than for the upstream prism, whereas C_{l_2} and C_{m_2} both obtain near-zero values.

For the two larger centre-to-centre spacing values, the overall situation within the subcritical Reynolds flow state (points 12 and 21 at $Re_D = 1.5 \times 10^5$) is similar. In both cases, the surface pressure distribution on the upstream prism has now perfectly converged to that one of the single prism (Figures 16g and 17h, as well as Figures 16m and 17n).

Compared to the previous case, i.e., point I at $S/D = 2.8$, the larger spacing now leads to a reduced shielding of the downstream prism by the upstream one and thus a diminished mean suction on the front surface of the downstream prism of $C_{p,f_2} = -0.23$ ($S/D = 4.0$) and $C_{p,f_2} = -0.18$ ($S/D = 5.6$) in Figure 18b. Simultaneously, local regions with high negative pressure values appear at both forward-directed rounded edges of the downstream prism, their suction effect increasing with growing S/D . The simplified process is conjectured as follows: for all three spacing values, the state of the flow at the subcritical Reynolds numbers of $Re_D = 1 - 2 \times 10^5$ is part of the *co-shedding regime (mode II)*. However, only at the two largest spacing values the gap between the two prisms is sufficiently large for the separated shear layers, coming from the upstream prism, to produce vortical structures, which can then impinge on the front surface of the downstream prism. The turbulent boundary layer on the downstream prism separates at the two forward directed rounded edges, but this time, both turbulent free shear layers have enough energy to be able to reattach to the side surfaces II and IV of the prism. They thereby form a shallow recirculation region above these side surfaces, in combination with a strong suction peak at both leading edges. A re-separation of the reattached turbulent boundary layer then occurs at both leeward-directed upper edges of the downstream prism, induced by the strong pressure increase inside the surface boundary layer over those rounded edges. Furthermore, this secondary boundary layer separation induces a lower mean suction pressure at the base of the downstream prism of $C_{p,b_2} = -1.02$ ($S/D = 4.0$) and -0.90 ($S/D = 5.6$) compared to $C_{p,b_2} = -1.24$ at $S/D = 2.8$. The combination of the forward-directed high suction peaks at both upstream edges, and the lower

negative mean base pressure results in a mean positive drag force on the downstream prism of $C_{d_2} = 0.70$ at $S/D = 4.0$, a value that is surprisingly equal to the mean drag coefficient at $S/D = 2.8$, whereas at $S/D = 5.6$ a lower mean drag coefficient of $C_{d_2} = 0.58$ is obtained. Interestingly, the changes in the mean surface pressures on the downstream prism have hardly any effect on the frequency with which the vortices are shed from this prism at $Re_D = 1 - 2 \times 10^5$, see Figure 8.

5.1.2. Critical flow state

Returning to the smallest prism-to-prism distance $S/D = 2.8$, an increase in the Reynolds number towards $Re_D = 3.6 \times 10^5$ (point 3) within the first half of the critical flow state induces only a small decrease of the absolute negative pressure coefficients on both side surfaces and at the base (Figures 16a and 17b). This leads to a decrease of the mean drag force on the upstream prism (Figure 4a), whereas both the lift and pitch moment coefficient remain constant due to symmetry of $C_{p,cyl}$. In Figure 18b it is shown, that at point 2 ($Re_D = 2.2 \times 10^5$, i.e. high subcritical), the difference between C_{pb_1} and C_{pf_2} has decreased, most probably as a result of the weaker interaction of the free shear layers from the upstream prism with the downstream prism. On the latter one, the values of the suction pressures on opposite surfaces are in perfect harmony. This explains, why the downstream prism experiences at point 2 neither a net drag (Figure 4a) nor a net lift force (Figure 5a). Hence, for Reynolds numbers that lie inside the range of $Re_D = 2 - 2.6 \times 10^5$, the smallest spacing $S/D = 2.8$ corresponds exactly to the critical spacing S/D_{cr} . The data in the Figures 16a, 16c, and 18b tell us, that for $Re_D = 2.6 - 3.6 \times 10^5$ - hence, including point 3 - the values of C_{pf_2} and those of C_{pb_1} match almost perfectly. It can therefore be reasonably assumed, that the free shear layers coming from the upstream prism reattach on the side surfaces of the downstream prism before even having the opportunity of rolling up into distinct vortices. At these Reynolds numbers, the flow around the tandem prism constellation with $S/D = 2.8$ has thus switched from *mode II* to *mode I*. Because of the presence of a stagnant fluid in the gap between both prisms, a suction effect is created on the downstream prism, resulting in an overall negative mean drag of $C_{d_2} = -0.24$ that acts on this prism at point 3. Surprisingly, the power spectral density of the lift fluctuations on the downstream prism at $Re_D = 3.6 \times 10^5$ (point 3 in Figure 9a) shows two clear peaks: one at approximately $f_L = 42$ Hz, corresponding to $St_L = 0.115$ (subcritical), the other at $f_L = 92$ Hz, which corresponds to $St_L = 0.212$ (supercritical). Since both peaks have similar height, it can be argued that the flow around this prism switches continuously back and forth between these two flow regimes. Although the instantaneous flow around the downstream prism is thus highly dynamic, the time-averaged surface pressure distribution is then again clearly symmetric, as is shown in the Figures 16c and 17b.

At point 4 ($Re_D = 3.7 \times 10^5$, within the second half of

the critical flow state), the mean surface pressure distributions on both prisms become highly asymmetric, see the Figures 16a, 16c, and 17c. Regarding the upstream prism, the increase in Reynolds number has led to a change of the location of the laminar-turbulent transition along the free shear layers to a position further upstream and has now reached the side surfaces of the prism. Consequently, a shallow recirculation bubble is formed on the upstream portion of the side surface *IV* with the laminar/turbulent transition occurring over the bubble, in combination with the appearance of a strong suction peak at the upper windward-directed rounded edge. Downstream of this separation bubble, the turbulent reattached boundary layer on surface *IV* remains attached to this face until the downstream upper edge of the prism has been reached, at which point it re-separates. In contrast, the lower free shear layer remains separated up to the base region, as the kinetic energy of the flow is not yet sufficiently large enough to force a reattachment on surface *II* and thus the formation of a separation bubble at this side face as well. This asymmetric flow around the upstream prism induces a smaller near wake directly behind the upstream prism that is reflected in a step in the mean drag force between the point 3 and 4 down to $C_{d_1} = 0.78$. Although it is expected that the side surface on which the shear-layer reattachment occurs, switches at this critical Reynolds number back and forth between the surfaces *II* and *IV*, the mean surface pressure distributions in Figure 16a and 17c show, that a reattachment of the upper free shear layer is clearly favoured. This results in a distinct positive average lift coefficient of $C_{l_1} = 0.66$, and a negative mean pitch moment coefficient of $C_{m_1} = -0.056$ on the upstream prism. Owing to proximity effects between both tandem prisms, the downstream prism experiences a strong asymmetric surface pressure distribution as well. Compared to the upstream one, this pressure distribution seems to be mirrored with respect to the virtual horizontal line through $s/D = 0.47$ and 2.33: a shallow separation bubble and the accompanying strong suction peak now both appear on the lower windward-directed rounded edge, whereas the upper free shear layer remains separated up to the base region. The resultant mean lift force is now negative instead, i.e. $C_{l_2} = -0.41$. Moreover, a positive pressure is present on the upper half of the front surface *I* of the downstream prism, which leads - in comparison to point 3 - to a lower average suction force of $C_{pf_2} = -0.22$ on this surface. Since the mean pressure at the base of the downstream prism remains at a relatively constant level, an increase in Reynolds number from $Re_D = 3.6 \times 10^5$ (point 3) to $Re_D = 3.7 \times 10^5$ (point 4) is thus accompanied by a sign reversal of C_{d_2} to a positive value of 0.24, i.e. the state of the flow around both prisms returns to *mode II*.

Regarding the mean surface pressure distribution on the upstream prism at the other two spacing values, an increase in the Reynolds number within the critical flow state towards $Re_D \approx 4 \times 10^5$ (i.e. points 13 \rightarrow 15 and points 22 \rightarrow 25 for, respectively, $S/D = 4.0$ and 5.6) leads also for those

two configurations to a distinct asymmetry in the pressure distribution due to the appearance of a one-sided separation bubble and the associated strong suction peak at its leading edge. The simultaneous occurrence of two peaks in the PSDs of the lift fluctuations at the points 13 and 14 ($S/D = 4.0$ in Figure 9c) and at the points 22 to 25 ($S/D = 5.6$ in Figure 9e and 9f) demonstrates, that also at these two spacing values the flow around the downstream prism switches continuously back and forth between the sub- and supercritical flow states. Despite this highly dynamic flow behaviour at all three spacing values, a fascinating point is the variation of the favoured surface at which the shear layer reattaches: whereas at $S/D = 2.8$ and 5.6 it preferably occurs on the upper side surface *IV* of the downstream prism, its lower side surface *II* is favoured at $S/D = 4.0$. Once the mean flow has selected its preferable side surface at which the laminar–turbulent transition and free shear layer reattachment take place, it sticks to that surface throughout the remaining part of the critical flow state. Interestingly, this latter behaviour is then again independent of S/D .

The downstream prism experiences quite a significant change in surface pressure with increasing prism-to-prism spacing. At low critical Reynolds numbers, a clear resemblance between the surface pressure distribution at $S/D = 4.0$ (point 13 in Figure 17i) and at $S/D = 2.8$ (point 3 in Figure 17b) is found. In contrast, at a similar Reynolds number at $S/D = 5.6$ (point 22 in Figure 17o), positive pressures are obtained on the mid-section of the front surface *I*. Due to the appearance of a suction peak at both upstream rounded edges at this latter spacing, the shape of the overall pressure distribution of the downstream prism shows clear parallels with the pressure distribution of the single prism at super- to transcritical Reynolds numbers (van Hinsberg (2021a)). Hence, although the Reynolds number based on the undisturbed free-stream velocity is classified as within the critical flow regime, the downstream prism experiences a highly modified oncoming flow. The larger gap between both prisms allows the free shear layers that have separated from the upstream prism to roll up into isolated vortices prior to their impingement onto the downstream prism. The downstream prism thus experiences a more turbulent oncoming flow that results in a triggering of the laminar/turbulent transition of the surface boundary layer on this prism at lower free-stream Reynolds numbers compared to the upstream prism. This is confirmed by Figure 18b, which shows that an increase in S/D leads to less negative values of C_{pf_2} and thus an increased deviation from C_{pb_1} . At $S/D = 5.6$, the absolute values of C_{pf_2} at subcritical and low critical Reynolds numbers (e.g. points 21 and 22) coincide very well with those of the single prism at super- to transcritical Reynolds numbers in Figure 18a. The resultant mean drag force on the downstream prism at $S/D = 4.0$ and 5.6 is positive; hence, both spacing values thus lie above the critical spacing S/D_{cr} and the state of the flow around the tandem configuration equals in both cases *mode II*. A further interesting note is the fact that, similar to $S/D = 2.8$, the higher of both suction peaks on

both prisms appears at the exact opposite forward-directed rounded edge. This results in opposite directions of the mean lift force on both tandem prisms, see Figure 5b and 5c.

5.1.3. Supercritical flow state

At the Reynolds number that marks the cross-over from the critical to the supercritical flow state the asymmetry in the surface pressure distribution on both prisms disappears completely. At all three S/D -values, a separation bubble is present on the upstream half of each side surface of the upstream prism and a secondary separation of the attached turbulent boundary layer occurs at the two downstream edges. Whereas at $S/D = 2.8$ the values of the suction pressures decline steadily in downstream direction along both side surfaces, a small intermediate plateau in the suction pressure decrease is observed at both larger spacing values on the first half of the surfaces *II* and *IV* at the points 17 ($S/D = 4.0$) and 26 to 28 ($S/D = 5.6$). Based on the current available measurement data, unfortunately no satisfactory answer can be given on the question of the exact physical phenomenon that leads to the appearance of this limited plateau. At this stage, it is nonetheless interesting to note that this plateau is present only within the supercritical flow state; at $S/D = 4.0$ it disappears as soon as the cross-over from the supercritical to the transcritical flow state has been reached.

The data in Figure 18b show that for $S/D = 2.8$ C_{pf_2} is nearly equal to C_{pb_1} at all supercritical Reynolds numbers. Because the turbulent boundary layer now separates at the two downstream edges of the upstream prism, the downstream lateral spreading of the free shear layers in the gap between both prisms is weaker. It can thus be argued, that the fluid in the gap between the two prisms is near to enclosed by those free shear layers. Interestingly, the overall pressure distribution on the downstream prism is similar to that one measured at subcritical Reynolds numbers, the actual values of the suction forces on each of the four surfaces are lower though. A comparison between the mean base pressure coefficient at sub- and supercritical Reynolds numbers in Figure 6a shows a reduction by a factor two. However, since C_{pf_2} is three times lower in the supercritical flow state, the resultant mean drag force on the downstream prism is lower in that flow state. The paradoxical situation, in which the mean drag on the downstream prism is higher than that on the upstream one in the complete supercritical flow state and in the first part of the upper transition (Figure 4a), can now also be explained quite easily by looking at the surfaces pressures on both prisms at point 5 in the Figures 16a and 16c, as well as in Figure 17d. The combination of a low mean base pressure for the upstream prism and the large suction peaks at both upstream edges – the latter resulting from the appearance of a two-sided separation bubble – results in a low mean drag force that acts on this prism. Even though the pressures on the front surface of the downstream prism are – depending on the exact Reynolds

number – either slightly negative or close to zero (see Figures 16c and 16d, points 5 and 6, as well as Figure 18b), the suction force at the base of the prism is much larger, owing to which the mean drag force on the downstream prism is larger than on the upstream one.

The higher the spacing value, the more the distribution of the surface pressures on the downstream prism approaches that of the upstream one, see for example Figure 17k and 17q. The influence of the proximity to the upstream prism can nevertheless still be noticed even at $S/D = 5.6$: both the pressure values on the front surface I and the heights of the suction peaks at both forward-directed edges are still lower than those for a single prism. As noted in Figure 18b, C_{pf_2} is for $S/D = 4.0$ and 5.6 even practically zero throughout the complete supercritical flow state, whereas values of $C_{pf_1} = 0.2 - 0.25$ are obtained for the upstream prism (Figure 18a). Proximity effects can even be seen in the surface pressure distribution on the upstream prism, although the differences in absolute pressure with respect to the single prism are in this case much smaller.

5.1.4. Upper transition and transcritical flow state

At a Reynolds number of about $Re_D = 7 \times 10^5$ the spacing value induces a divergence of the flow behaviour around the tandem prism constellation. At the largest spacing of $S/D = 5.6$, the state of the flow remains supercritical up to the highest investigated Reynolds number of $Re_D = 6$ million. Variations in the pressure distributions only occur on a small scale with increasing Reynolds number, see for example the points 26 to 28 in Figure 16n and 16p. This leads to largely constant values of all mean and fluctuating aerodynamic coefficients and the Strouhal number, as presented and discussed in detail in section 4.1. In contrast, at $S/D = 2.8$ and 4.0 the supercritical flow state is finite and continues up to about $Re_D = 7 \times 10^5$ and 1.85×10^6 , respectively. Similar to $S/D = 5.6$, also at these two smaller spacing values both tandem prisms possess relatively constant pressure distributions throughout the supercritical flow state. Whereas at $S/D = 4.0$ a jump from the supercritical directly into the transcritical flow state takes place at $Re_D = 1.85 \times 10^6$, the upper transition regime appears in-between $Re_D = 7 \times 10^5$ and 2.23×10^6 for $S/D = 2.8$. As has been presented in Figure 4a, this latter Reynolds-number regime is characterised by a steady rise of the mean drag force that acts on the upstream prism with increasing Reynolds number, its increase levelling off towards the end of this flow state, in combination with significant variations of the mean drag coefficient of the downstream prism. The former behaviour is induced by various changes in the surface pressures that take place all at once: i) a doubling of C_{pf_1} (see Figure 18a), ii) an increase of the negative absolute value of C_{pb_1} by a factor three (see Figure 18ab, and iii) a reduction of both the height and width of the suction peaks on the rounded edges, as indicated by the surface pressure distributions in the points 6 to 8 in Figure 16b. Regarding the downstream prism, we notice a completely different aerodynamic behaviour in the upper tran-

sition. Whereas the light increase of C_{pb_2} up to lower negative values occurs over the complete flow regime (Figure 6a), a strong decrease of C_{pf_2} takes place only in the second part of the upper transition, i.e. in between the points 6 ($Re_D = 1.12 \times 10^6$) and 8 ($Re_D = 1.68 \times 10^6$), despite the close proximity of the downstream prism to the upstream one. Since these two pressure coefficients slowly converge towards the same negative value and the overall pressure distribution flattens (see Figure 16d), the decrease of the mean drag coefficient of the downstream prism is obvious. At point 8 we have the special situation that C_{pf_2} and C_{pb_2} are in perfect equilibrium, as a result of which the downstream prism experiences at this Reynolds number no net drag force (Figure 4a) and the spacing $S/D = 2.8$ corresponds once more exactly to the critical spacing S/D_{cr} . Because the value of C_{pf_2} is furthermore nearly equal to C_{pb_1} , it can once more be argued, that the gap between the two prisms is near to enclosed by the two free shear layers and the flow in the gap is thus near to stagnant. The shielding of the downstream prism by the upstream one has hence increased significantly in the range of $Re_D = 1.12 - 1.68 \times 10^6$.

In the final transcritical flow regime, the upstream prism experiences a mean surface pressure distribution – and thus a flow structure and aerodynamic coefficients – that seem to be independent of both the Reynolds number and the spacing value, see the points 9 to 11 and 18 to 20 for $S/D = 2.8$ and 4.0 , respectively. Because the separation bubbles are either very small or have even disappeared completely, only a weak suction peak appears at the rounded edges. That explains why the transcritical values of C_{pf_1} in Figure 18a are about twice as high as in the supercritical flow state. Proximity and shielding have then again a clear noticeable effect on the pressure distribution of the downstream prism, in particular on the average pressure value on surface I . According to Figure 18b, C_{pf_2} is at the smallest spacing about 2.5 times larger than at the intermediate spacing and thus lies much closer to C_{pb_1} . Hence, the shielding of the downstream prism by the upstream one is at the smaller of these two spacing values much more pronounced. This also explains why, in contrast to $S/D = 4.0$, small areas with higher suction forces at both forward-directed edges of the downstream prism do not appear in the mean pressure distribution at $S/D = 2.8$. It is this difference in C_{pf_2} between the smallest and medium spacing, in combination with similar constant values of C_{pb_2} , that results in mean drag forces on the downstream prism that are about 50% - 100% higher at $S/D = 4.0$. Surprisingly, the transcritical PSDs of the fluctuating lift forces on the downstream prism in Figure 9b and 9d not only have nearly equal shapes at both spacing values, but - at equal transcritical Reynolds number - the single dominant and relatively narrow peak in each power spectrum appears at similar non-dimensional shedding frequencies and has a similar height. In both cases, approximately equal Strouhal numbers are thus obtained in the transcritical flow state. These Strouhal numbers further-

more equal those at subcritical Reynolds numbers (points *I* and *2* at $S/D = 2.8$ and point *12* at $S/D = 4.0$). However, the dominant peaks in the latter flow state are much broader and one to two orders of magnitude lower.

5.2. Effects of Reynolds number and spacing on the pressure distribution at the second symmetric angle of incidence of 45°

The mean surface pressure distribution at mid-span on both prisms at an angle of incidence of 45° are presented in Figure 19 and 20. The former figure has the same matrix structure as Figure 16, whereby the letters *A* to *Y* correspond to the marked Reynolds numbers in Figure 10. Figure 20 then again gives an additional qualitative impression of the mean surface pressure distribution on both prisms by means of a scaled vectorial representation. For each prism-to-prism spacing value one distribution is shown per Reynolds-number flow regime. The letters inside the prisms correspond to those in the Figures 10 and 19. Similar to Figure 17, the values of the mean drag, mean lift, and mean pitch moment coefficients are listed inside the sketches and in Appendix A3 to facilitate a comparison of the impact of a change in the surface pressures on the mean aerodynamics.

At the intermediate spacing of $S/D = 4.0$, the pressure distributions on the two prisms show in the various Reynolds-number regimes characteristics of the distributions measured at both other spacing values. The following discussion will therefore mainly focus on the results obtained at this intermediate spacing, as the trends of the aerodynamic coefficients with increasing Reynolds number at $S/D = 2.8$ and 5.6 can be deduced quite easily from the underlying pressure distributions and are thus self-explaining.

5.2.1. Upstream tandem prism at $S/D = 4.0$

Focussing at first on the upstream one of the two tandem prisms, it is noted in Figure 19 that the pressures on the two windward-directed surfaces *I* and *II* are for each Reynolds number near to equal to those of the single prism. Deviations in the negative peak pressure coefficients at both shoulder edges do occur in the critical up to the transcritical flow state and result in differences in C_{pf_1} as shown in Figure 18c. These differences in peak pressure are, however, relatively small when compared to the absolute peak pressure values. A clear different behaviour of the surface pressure with respect to the single prism only occurs at the base of the upstream prism. Whereas the mean pressure distribution on the surfaces *III* and *IV* of the single prism possesses a more or less distinct V-shape at each Reynolds number, this pressure distribution on the upstream prism is relatively flat. Exactly this flatness of $C_{p,cyl}(S/D)$ is a clear indication for the mutual interference between both tandem prisms in the sense of a modification of the flow field, induced by the presence of the downstream prism, that is fed back to the upstream one. The resultant lower

mean suction force at the base of the upstream prism with respect to that one of the single prism (figure 13) leads to a lower mean drag force that acts on this upstream prism in the *reattachment flow regime* (Figure 10).

Interestingly, at the points *L* (Figure 19g) and *M* (Figure 19h) within the upper transition flow regimes a clear V-shaped pressure distribution is present on the two base surfaces *III* and *IV* of the upstream prism, which results in a near to perfect match of the overall pressure distribution with that of the single prism. This explains the occurrence of an almost perfect agreement between C_{d_1} and $C_{d_{single}}$ in a small region at the beginning of the upper transition – including point *L* at $Re_D = 6.2 \times 10^5$ – at $S/D = 4.0$ in Figure 10b.

A closer look at the values of the mean lift and pitch moment coefficients of the upstream prism in Figure 11 leads to the direct conclusion that within the portrayed Reynolds-number range both aerodynamic coefficients show a completely different behaviour with increasing Reynolds number than their counterparts belonging to the single prism. This counts in particular for the supercritical, the complete upper transition, and the first part of the transcritical flow state up to approximately $Re_D = 1.1 - 1.2 \times 10^6$, for which – in contrast to the single prism – clear non-zero values for C_{l_1} and C_{m_1} are obtained. In case of the single prism, a shallow recirculation bubble is present above both shoulders from the supercritical flow regime onwards, hence, for $Re_D \geq 5.6 \times 10^5$ (van Hinsberg, 2021a). The same counts for the current tandem configuration for Reynolds numbers above the supercritical point *K* at $Re_D = 5.5 \times 10^5$. For the single prism, the pressure distributions on the upper and lower surfaces are highly symmetric and the values of both C_l and C_m are therefore close to zero. Although a "symmetric" bubble occurrence would suggest a reappearance of the symmetric surface pressure distribution on the upstream prism as well, the values of C_{l_1} and C_{m_1} in Figure 11b both show that it still takes much longer, i.e. until the beginning of the transcritical flow state, before a nearly symmetric flow field with $C_{l_1} = C_{m_1} \approx 0$ has firmly settled around the upstream prism. The explanation for these deviations is found in the height of the local negative pressure peaks at both shoulders of the upstream prism. Whereas for the single prism both shoulders experience a rather equal suction force, a difference in negative peak pressure between the upper and lower shoulder is experienced by the upstream prism in those particular flow regimes, see Figure 19 (left column) and 20. The latter induces a slight asymmetric mean pressure force between the upper and lower prism surfaces, which results in a non-zero mean lift force and pitch moment that act on the upstream prism. Interestingly, the occurrence of this asymmetric pressure distribution is apparently not that obvious when looking solely at the mean drag force in Figure 10.

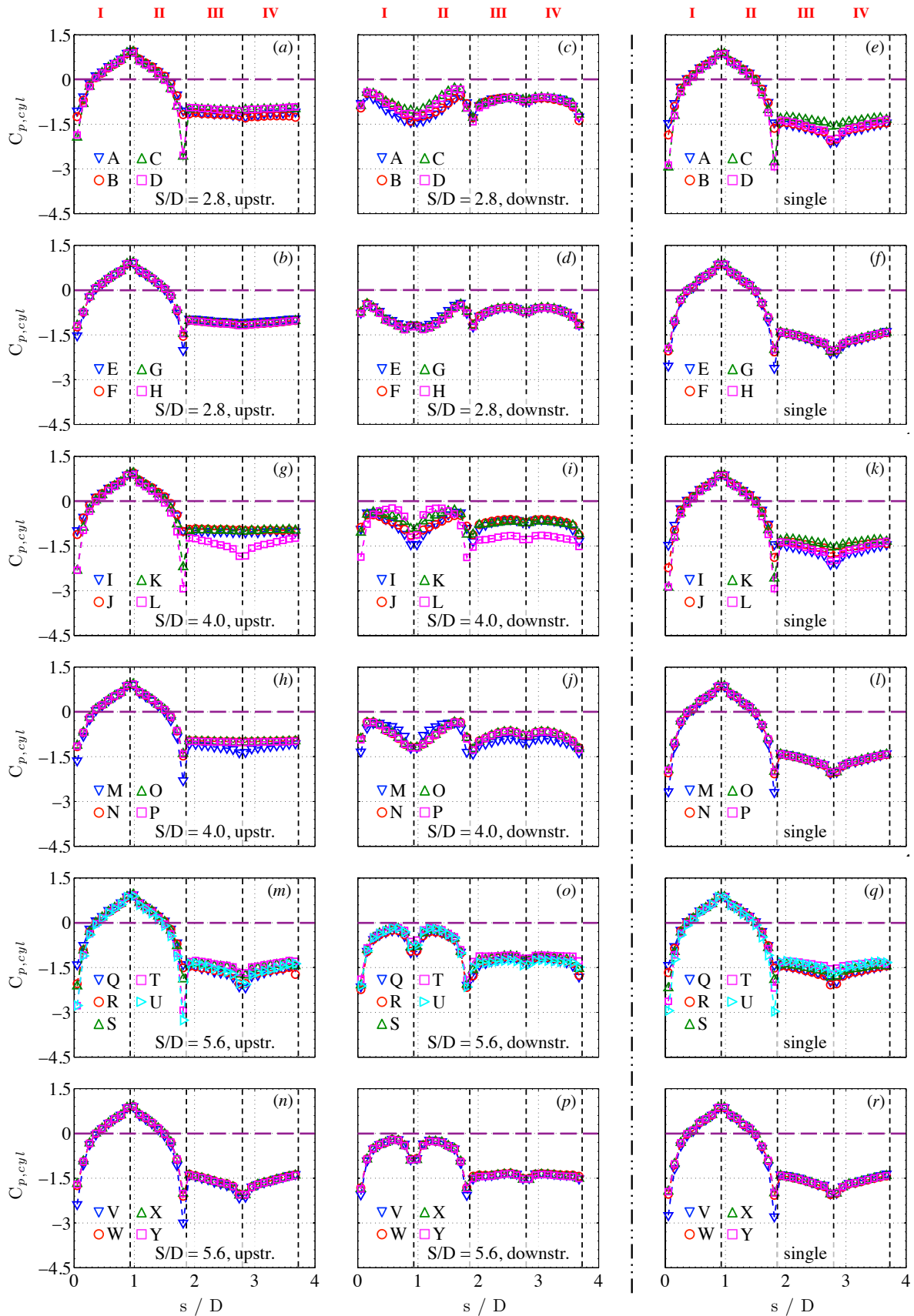


Figure 19: Quantitative representation of the mean circumferential surface pressure distributions at mid-span of the upstream (left column) and downstream (right column) tandem prism, as well as of the single prism (right column) by van Hinsberg (2021a), at $\alpha = 45^\circ$. (a)-(d): $S/D = 2.8$; (g)-(j): $S/D = 4.0$; (m)-(p): $S/D = 5.6$. The individual curves correspond to the points marked by the numbers A to Y in Figure 10 and in the Appendices A3 and A4.

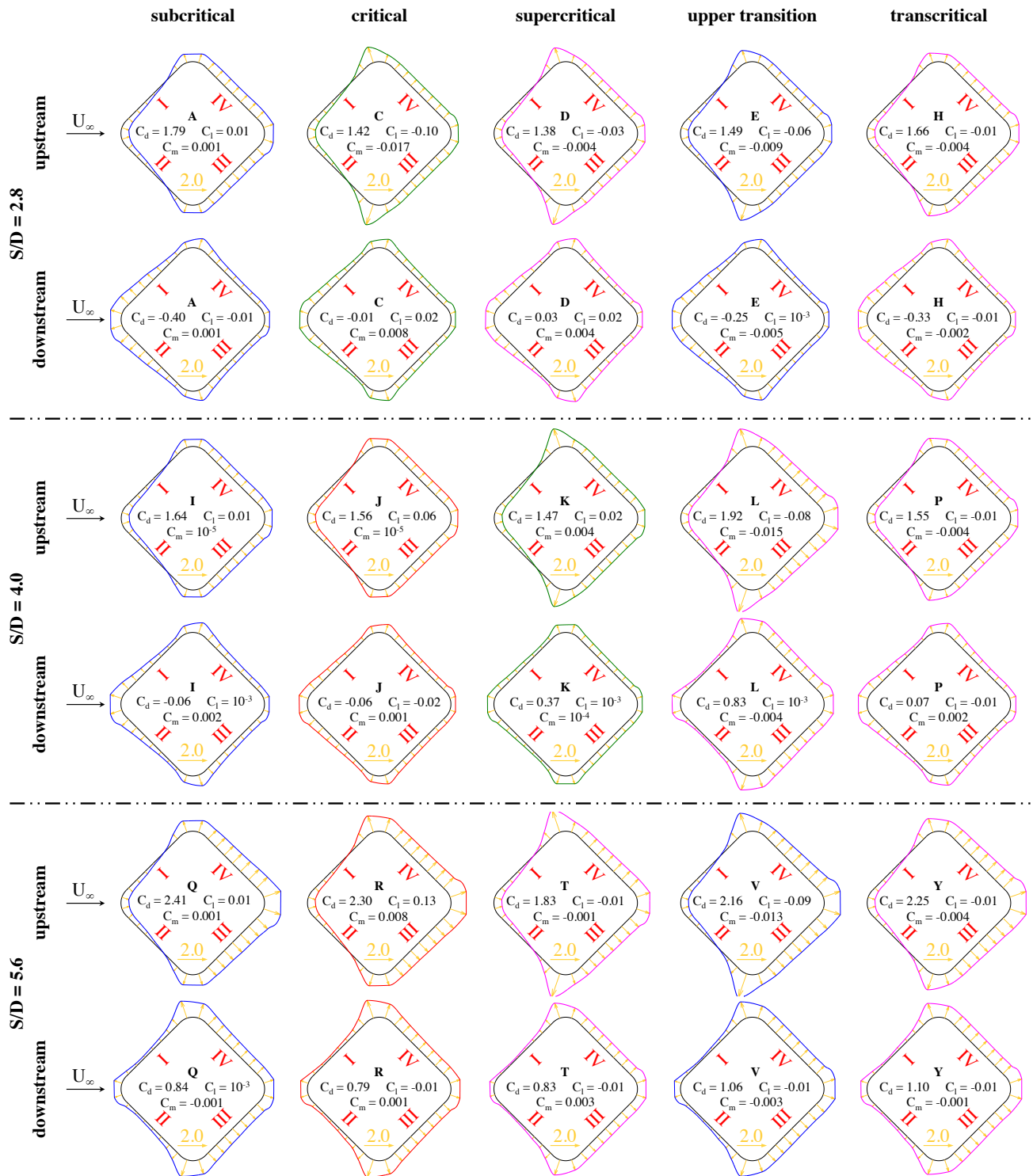


Figure 20: Qualitative scaled vectorial representation of the mean circumferential surface pressure distributions at mid-span of both tandem prisms at $\alpha = 45^\circ$. Two upper rows: $S/D = 2.8$; two centre rows: $S/D = 4.0$; two lower rows: $S/D = 5.6$. The numbers inside the individual graphs correspond to the points marked in Figure 6 and 19 and in the Appendices A3 and A4.

5.2.2. Downstream tandem prism at $S/D = 4.0$

The surface pressure distributions on the downstream prism at $S/D = 4.0$ in Figure 19i and 19j demonstrate the influence on the prism's aerodynamic behaviour as a result of an angle change of both tandem prisms from $\alpha = 0^\circ$ to

45° . Independent of the Reynolds number, each pressure tap in the mid-section of the downstream prism experiences at this latter angle of incidence a mean suction. Starting from the upstream-directed rounded edge and wandering in downstream direction along both windward-directed sur-

faces *I* and *II*, a pressure increase is first of all experienced up to a minimum negative pressure value, which is then followed by a steep mean pressure rise towards large negative pressure values at both shoulders. The actual shape of the pressure distribution on these two surfaces is then again clearly Reynolds-number dependent.

Figure 10b shows that for subcritical and low critical Reynolds numbers the net drag force on the downstream prism is slightly negative, which implies that the gap size is still too small to prevent a reattachment of the free shear layers on the downstream prism. At this intermediate spacing, this reattachment is most likely to occur at $s/d = 0.15 - 0.26$ (surface *I*) and $s/d = 1.61 - 1.71$ (surface *II*) in the subcritical (point *I*) and low critical (point *J*) flow regimes, as at these surface locations $C_{p,cyl}$ reaches its largest negative value, see Figure 19i. The partial shielding of the downstream prism by the upstream one induces a V-shaped pressure distribution in between both reattachment points on both forward-directed surfaces of the downstream prism. That the shielding is only partial is confirmed by the clear difference between C_{pb_1} and C_{pf_2} in Figure 18d as well, since in case of a full shielding a near-to perfect match between their values would have been measured. The rough balance between the negative values of C_{pf_2} and C_{pb_2} explains the occurrence of a near to zero mean drag force on this prism (Figure 10b). In the subsequent upper part of the critical flow state, the value of C_{pf_2} gets less negative (see Figure 18d), indicating that the amount of shielding diminishes as a result of the decreasing width of the near wake behind the upstream prism. This results in a steady decrease of the thrust force on the downstream prism towards a positive drag force at the cross-over from the critical to the supercritical flow regime at point *K* (Figure 10b). The switch of the sign of C_{d_2} at $Re_D = 4.7 \times 10^5$ - corresponding to point *J* - signals the change in the flow state from *mode I* to *mode II*. From this point on, the flow around the tandem prism configuration with $S/D = 4.0$ remains in this state up to high transcritical Reynolds numbers. After separation from the upstream prism at a surface location just downstream of its shoulder edge, the free shear layers can now roll up into distinct vortices in the gap before impinging on the downstream prism. The downstream prism therefore experiences a periodic vortex impingement. This produces a transformation of the mean pressure distribution on the surfaces *I* and *II* of the downstream prism from a V-shape into a clear "double bump"-shape at the supercritical point *K*.

In Figure 18, it is noted that for $Re_D > 5.5 \times 10^5$, i.e. right after point *K*, both C_{pf_1} and C_{pb_1} drop towards significantly lower values that lie close to those obtained for the single prism. Despite the moderate distance between both prisms, this sudden decrease in C_{pb_1} at those Reynolds numbers has a negligible influence on C_{pf_2} though, and the behaviour of C_{pf_2} is at this stage actually the opposite to what one would expect. In general, the sudden increase of the suction at the base - and thus of the mean drag force - of the upstream prism would be a strong indicator for a

large increase in the width of its near wake due to the higher lateral spacing of the separated shear layers in this area. Owing to the moderate gap size between both prisms, the reattachment points of those free shear layers would therefore most probably shift to a location further downstream on the surfaces *I* and *II* of the downstream prism. Hence, an increased shielding of the downstream prism by the upstream one would occur, as a result of which the value of C_{pf_2} would plunge as well and thus approach C_{pb_1} . The downstream prism would then experience a much lower mean drag coefficient C_{d_2} as has currently been measured. However, Figure 10b and 18d clearly show that neither C_{d_2} nor C_{pf_2} do follow this hypothetical trend. As expected, an actual change in shape of the surface pressure distribution on the downstream prism between the points *K* (supercritical) and *L* (lower upper transition) in Figure 19i does occur. However, the resultant "double bump"-shaped pressure distribution at point *L* suddenly closely resembles those ones belonging to the points *U* and *V* in the upper transition at the largest spacing of $S/D = 5.6$ in Figure 19o and 19p. The same counts for the values of the derived coefficients C_{pf_2} and C_{pb_2} , as well as of the mean and fluctuating force coefficients. The shielding of the downstream prism is thus expected to have decreased, which is confirmed in Figure 18d by the slight increase of C_{pf_2} in the corresponding range of Reynolds numbers. The sudden change in the flow around the upstream prism at point *L* does induce a steep rise of the suction force at the base of the downstream prism though, as the Figures 19i and 20 make clear. This results in the occurrence of the highest mean drag force on the downstream prism for $S/D = 4.0$. The second half of the upper transition, e.g. point *M*, is then characterised by a gradual recovery of both C_{pf_1} and C_{pb_1} , which results in a steady decrease of C_{d_1} in Figure 10b. This reduction of the mean drag force on the upstream prism means, that - although the flow state still belongs to the *co-shedding regime* - the mutual influence of both prisms increases again. As a consequence of the increased shielding in the upper transition, the "double bump"-shape of the pressure distribution on the surfaces *I* and *II* slowly re-migrates into a concave V-shape, meaning that the surface pressure distribution approaches that one present at low subcritical Reynolds numbers. Interestingly, this change in shape induces a slight repositioning of the locations of the suction peaks on the surface, while the actual pressure values remain at a constant level. Whereas C_{pf_2} shows only a light increase in magnitude, C_{pb_2} decreases sharply with increasing Reynolds number, see Figure 13b and point *M* in Figure 19j. In particular this strong change of C_{pb_2} is responsible for the decrease of the mean drag on the downstream prism towards nearly zero, but still positive transcritical values that remain constant throughout this latter flow regime.

Although at the intermediate spacing the flow state switches at point *J* from *mode I* to *mode II*, the frequency of the vortices shed into the wake of the downstream prism is only slightly affected and remains at a lower level than that of

the single prism. The upstream prism sheds vortices as well at Reynolds numbers above 4.7×10^5 , which then impinge onto the sides of the downstream prism. However, the actual shedding process behind the downstream prism is not altered by the arrival of those vortices. A similar conclusion can be drawn for the intensity with which the vortices

are shed by the downstream prism, i.e. $\sqrt{(C_L')^2}_2$, from Figure 12b. It shows that the values of the fluctuations of the lift force lie relatively close to those of the single prism. In the first part of the critical flow state, we even see a near to perfect match between them. The only exception forms once again the first part of the upper transition, at which the values of both the Strouhal number St_{L_2} and the fluctua-

tions of the lift force $\sqrt{(C_L')^2}_2$ approach those of the single prism. As described earlier, at these Reynolds numbers the aerodynamics of the upstream prism closely resembles that one of the single prism. Hence, with a high probability it can thus also be assumed, that the upstream prism sheds its vortices at an equal frequency. Because the downstream prism experiences a periodic impingement of those vortices, their arrival triggers the vortex shedding process of the downstream prism. This then results in a shedding synchronisation between both tandem prisms, which explains the relatively close match between St_{L_2} and $St_{L_{single}}$ in Figure 15b. Interestingly, the fluctuations of the lift force then again show a larger deviation between the downstream and the single prism in this specific flow regime, see Figure 12b. At this spacing, the $St_{L_2}(Re_D)$ curve in Figure 15c follows nearly perfectly that one of the single prism throughout the complete studied Reynolds-number range.

At the same time, $\sqrt{(C_L')^2}_2$ is relatively Reynolds-number independent with values that are, depending on the exact Reynolds number, about 1.5 to 3 times higher than those of the single prism. These high values are most probably caused by a combination of vortex impingement on the downstream prism and an elevated turbulence intensity of and streamwise structures in the approaching flow.

6. Conclusions

The current experimental study focussed on the combined influence of the Reynolds number and the centre-to-centre spacing on the cross-flow around two 2D square-section prisms at two angles of incidence. For that purpose, experimental investigations in the High-Pressure Wind Tunnel in Göttingen were performed, thereby focusing in particular on the mid-section surface pressure distributions and their derived sectional coefficients (base pressure, lift, drag, and pitch moment) of both prisms, as well as on the spanwise-integrated mean and fluctuating fluid loads on the downstream prism and the frequency of the vortices shed in its wake. The two equal prisms had rounded edges of $r/D = 0.16$ and a slightly rough surface to simulate a light coverage by hard marine fouling. They were arranged inline at three centre-to-centre distances of $S/D = 2.8, 4,$ and 5.6 and at an incidence angle of either $\alpha = 0^\circ$ or 45° . For

each possible combination of α and S/D the effect of the Reynolds number on the aerodynamic characteristics of the tandem prism configuration was studied for $1 \times 10^5 \leq Re_D \leq 7 \cdot 8 \times 10^6$. Based on these measurements, the main conclusions can be summarised as follows:

1. For both angles of incidence, the appearance of the mean sectional drag curve for the upstream prism $C_{d_1}(Re_D)$ is only at the largest spacing value of $S/D = 5.6$ similar to the behaviour of a single rounded square-section prism with equal surface roughness. The same counts for the mean base pressure coefficient, as both coefficients are directly linked to one another. At the other two spacing values, equivalent values for C_{d_1} and $C_{d_{single}}$ on the one hand and C_{pb_1} and $C_{pb_{single}}$ on the other are either obtained in certain flow states only ($\alpha = 0^\circ$) or do not occur at all ($\alpha = 45^\circ$). This demonstrates the mutual interference between both tandem prisms at $S/D = 2.8$ and 4.0 in the sense of a modification of the flow field, induced by the direct presence of the downstream prism, that is fed back to the upstream one. A change in S/D from 2.8 to 4.0 at $\alpha = 0^\circ$ furthermore results in the cancellation of the upper transition, whereas a further increase in spacing to $S/D = 5.6$ leads to the additional disappearance of the transcritical flow regime.
2. The behaviour of the mean sectional drag curve $C_{d_2}(Re_D)$ of the downstream prism strongly depends on both the spacing S/D and the angle of incidence α . The only common results at both angles of incidence are an overall increasing drag and a flattening of the curve for a larger spacing value. At $\alpha = 0^\circ$, the largest variations in the values of both aerodynamic coefficients are obtained at $S/D = 2.8$. Only at this spacing does the downstream prism even experience a thrust force at high subcritical and low to medium critical Reynolds numbers. The drag inversion indicates that the critical spacing S/D_{cr} decreases sharply in the former and increases sharply in the latter Reynolds-number range. The state of the flow around the two tandem prisms thus switches twice between the *co-shedding regime (mode II)* and the *reattachment regime (mode I)*. At $\alpha = 45^\circ$, the curves of the mean drag on the downstream prism then again exhibit the inverse development of that of the upstream one. At $S/D = 2.8$ and 4.0 , the lowest drag forces are even obtained for subcritical and transcritical Reynolds numbers. Whereas at $S/D = 2.8$ C_{d_2} remains negative throughout the various flow regimes and only touches a slightly positive value at the supercritical Reynolds number, the downstream prism experiences at $S/D = 4.0$ no net drag force over the complete subcritical and transcritical flow states and a clear positive drag force in the other flow states.
3. The RMS values of the fluctuating lift on the downstream prism, being a measure of the intensity of the

vortex shedding process in its wake, possess an opposite trend with increasing S/D between both angles of incidence. Whereas at $\alpha = 0^\circ$ and $S/D = 2.8$ the values for $\sqrt{(C_L')^2}_2$ are either lower (subcritical and critical flow states), equal (supercritical flow state), or higher (upper transition and transcritical flow states) than those of the single prism, a near to perfect match between the RMS values of the fluctuating lift on the downstream and on the single prism appears at $\alpha = 45^\circ$. An increase in spacing induces at $\alpha = 0^\circ$ an approach of the values for $\sqrt{(C_L')^2}_2$ towards those of the single prism for subcritical and critical Reynolds numbers only, whereas at $\alpha = 45^\circ$ not only an increasingly divergence between both values occurs in all flow regimes, but the values for $\sqrt{(C_L')^2}_2$ also become increasingly Reynolds-number independent. The trend of the curve of the Strouhal number $St_{L_2}(Re_D)$ of the downstream prism is for each spacing at both incidence angles close to that of the single prism. For both incidence angles, the differences between St_{L_2} and $St_{L_{single}}$ are in all flow states the largest for $S/D = 2.8$, decrease with increasing S/D , and have disappeared at $S/D = 5.6$. Furthermore, at $\alpha = 0^\circ$ two peaks occur in the power spectra of the lift fluctuations at several Reynolds numbers in both the critical flow state and the upper transition.

4. The behaviour of the mean aerodynamic force and pitch moment coefficients with Reynolds number of the upstream prism are for both angles of incidence mainly caused by simultaneous changes in the locations of the laminar-to-turbulent transition points either on the free shear layers or on the prism surface and of the locations of the boundary layer separation from the surface. Moreover, for critical up to transcritical Reynolds numbers, the reattachment of the turbulent free shear layers and the secondary turbulent boundary layer separation from the surface further downstream play a distinct role as well. Proximity effects, like the impingement on the downstream prism of either the free shear layers from the upstream prism at $S/D = 2.8$ (and 4.0 at $\alpha = 45^\circ$) or the distinct vortices formed in the gap between both prisms at larger S/D , are then again the main parameters that determine the behaviour of the boundary layer on the downstream prism and thus its aerodynamics.

All in all, the present results show that – at realistic maritime Reynolds numbers of $\mathcal{O}(10^6)$ to $\mathcal{O}(10^7)$ – the combined mean drag force on the two tandem structural foundation elements of floating offshore structures is lower at an angle of 45° with respect to the oncoming flow. This only counts for $S/D = 2.8$ ($\Delta C_{d_{1+2}} = -19\%$) and $S/D = 4.0$ ($\Delta C_{d_{1+2}} = -11\%$) though, as for $S/D = 5.6$ the overall mean drag force is an amazing 250% higher compared to $\alpha = 0^\circ$. The periodically fluctuating lift forces on the

downstream prism, and thus the strength of the shed vortices in its wake, are then again at $\alpha = 45^\circ$ for all three spacing values about 2 to 3 times higher compared to $\alpha = 0^\circ$. This latter behaviour coincides well with the observations by Gonçalves et al. (2015) and Liu et al. (2017). Regarding the vortex shedding frequencies, a difference between both angles of incidence occurs for $S/D = 5.6$ only. At that spacing, the Strouhal numbers at 0° angle of incidence are about twice as high. Since the amplitudes and frequencies of the possible pitch, sway, and/or yaw motions of deep-draft, multi-column floating offshore constructions are the result of an interplay of mainly the mean drag, the fluctuating lift, and the vortex shedding frequency, the current results show that a selection of the more preferable angle of incidence of the columns to the oncoming flow is always based on a compromise.

Acknowledgments

This research did not receive any specific grant from funding agencies in the public, commercial, or not-for-profit sectors. Technical assistance of Markus Löhner and Karsten Steiner of DNW (German Dutch Wind Tunnels) is gratefully acknowledged. Systemhaus Technik and Deharde GmbH are recognised for the construction and manufacturing of the wind tunnel models, respectively. Finally, the author would like to thank the reviewers for their fruitful comments and suggestions.

References

- Adams, T., Grant, C., Watson, H., 2012. A simple algorithm to relate measured surface roughness to equivalent sand-grain roughness. *Int. J. Mech. Mechatron. Eng.* 1, 66–71.
- Adeeb, E., Haider, B.A., Sohn, C.H., 2018. Influence of rounded corners on flow interference between two tandem cylinders using FVM and IB-LBM. *Int. J. Num. Meth. Heat Fluid Flow* 28, 1648–1663.
- Adeeb, E., Sohn, C.H., 2021. Flow and heat transfer characteristics of cylindrical structures with corner radius variation: Tandem, SIDE-BY-SIDE, and Flow-induced vibration. *Heat Transf. Eng.* 42, 251–269.
- Alam, M.M., 2014. The aerodynamics of a cylinder submerged in the wake of another. *J. Fluid Struct.* 51, 393–400.
- Alam, M.M., 2016. Lift forces induced by the phase lag between the vortex sheddings from two tandem bluff bodies. *J. Fluid Struct.* 65, 217–237.
- Alam, M.M., Bai, H., Zhou, Y., 2016b. The wake of two staggered square cylinders. *J. Fluid Mech.* 801, 475–507.
- Alam, M.M., Elhimer, M., Wang, L., Jacono, D.L., Wong, C.W., 2018. Vortex shedding from tandem cylinders. *Exp. Fluids* 59, 1–17.
- Alam, M.M., Meyer, J.P., 2011. Two interacting cylinders in cross flow. *Phys. Rev. E* 84, 056304–1–16.
- Alam, M.M., Moriya, M., Takai, K., Sakamoto, H., 2002. Suppression of fluid forces acting on two square prisms in a tandem arrangement by passive control of flow. *J. Fluid Struct.* 16, 1073–1092.
- Alam, M.M., Moriya, M., Takai, K., Sakamoto, H., 2003. Fluctuating fluid forces acting on two circular cylinders in a tandem arrangement at a subcritical Reynolds number. *J. Wind Eng. Ind. Aerodyn.* 91, 139–154.
- Alam, M.M., Zhou, Y., 2007. Phase lag between vortex shedding from two tandem bluff bodies. *J. Fluid Struct.* 23, 339–347.
- Arie, M., Kiyama, M., Moriya, M., Mori, H., 1983. Pressure fluctuations on the surface of two circular cylinders in tandem arrangement. *J. Fluids Eng.* 105, 161–166.

- Blevins, R.D., 2006. Flow-induced vibration. Second Edition Reprint. Krieger Publishing Company, Malabar, Florida, USA.
- Bokaian, A.R., Geoola, F., 1984. Hydroelastic instabilities of square cylinders. *J. Sound Vib.* 92, 117–141.
- Carassale, L., Freda, A., Marrè-Brunenghi, M., 2013. Effects of free-stream turbulence and corner shape on the galloping instability of square cylinders. *J. Wind Eng. Ind. Aerodyn.* 123, 274–280.
- Carassale, L., Freda, A., Marrè-Brunenghi, M., 2014. Experimental investigation on the aerodynamic behavior of square cylinders with rounded corners. *J. Fluid Struct.* 44, 195–204.
- Carmo, B.S., Meneghini, J.R., Sherwin, S.J., 2010. Secondary instabilities in the flow around two circular cylinders in tandem. *J. Fluid Mech.* 644, 395–431.
- Chen, C.R., Chen, H.C., 2016. Simulation of vortex-induced motions of a deep-draft semi-submersible in current. *Ocean Eng.* 118, 107–116.
- Cheng, J., Cao, P., Xiang, S., 2011. Wet tree semi-submersible with SCRs for 4000 ft water depth in the Gulf of Mexico, in: *Proc. 30th ASME-OMAE Conf.*, pp. 675–683.
- Choi, C.B., Jang, Y.J., Yang, K.S., 2012. Secondary instability in the near-wake past two tandem square cylinders. *Phys. Fluids* 24, 024102.
- Dalton, C., Zheng, W., 2003. Numerical solutions of a viscous uniform approach flow past square and diamond cylinders. *J. Fluid Struct.* 18, 455–465.
- Datta, B., Dey, P., Das, A.K., Debbarma, D., 2019. Numerical analysis of fluid forces and heat transfer characteristics around tandem rounded corners square cylinders. *J. Eng. Res. Appl.* 9, 40–51.
- Delany, N.K., Sorensen, N.E., 1953. Low speed drag of cylinders of various shapes. Technical Report 3038. Nat. Adv. Comm. Aero. Technical Note.
- Du, X., Chen, R., Dong, H., Ma, W., Xu, H., Zhao, Y., 2021. Aerodynamic characteristics of two closely spaced square cylinders in different arrangements. *J. Wind Eng. Ind. Aerodyn.* 208, 104462–1–9.
- Du, X., Chen, R., Xu, H., Ma, W., 2019a. Experimental study on aerodynamic characteristics of two tandem square cylinders. *Fluid Dynam. Res.* 51, 055508.
- Du, X., Xu, H., Ma, W., Dai, C., Liu, Q., 2019b. Experimental study on aerodynamic characteristics of two square cylinders at various incidence angles. *J. Wind Eng. Ind. Aerodyn.* 191, 154–169.
- Duchaine, F., Boileau, M., Sommerer, Y., Poinot, T., 2014. Large eddy simulation of flow and heat transfer around two square cylinders in a tandem arrangement. *J. Heat Transf.* 136, 101702–1–10.
- Etminan, A., Moosavi, M., Ghaedsharafi, N., 2011. Determination of flow configurations and fluid forces acting on two tandem square cylinders in cross-flow and its wake patterns. *Int. J. Mech.* 5, 63–74.
- Gonçalves, R.T., Fajarra, A.L.C., Rosetti, G.F., Kogishi, A.M., 2015. Effects of column designs on the VIM response of deep-draft semi-submersible platforms, in: *Proc. 25th ISOPE Conf.*, pp. 1063–1070.
- Gonçalves, R.T., Rosetti, G.F., Fajarra, A.L.C., Nishimoto, K., Oliveira, A.C., 2011. Experimental study on vortex-induced motions (VIM) of a large-volume semi-submersible platform, in: *Proc. 30th ASME-OMAE Conf.*, pp. 1–9.
- Gonçalves, R.T., Rosetti, G.F., Fajarra, A.L.C., Nishimoto, K., Oliveira, A.C., 2012c. Wave effects on vortex-induced motion (VIM) of a large-volume semi-submersible platform, in: *Proc. 31st ASME-OMAE Conf.*, pp. 471–482.
- Gonçalves, R.T., Rosetti, G.F., Fajarra, A.L.C., Oliveira, A.C., 2012b. Experimental study on vortex-induced motions of a semi-submersible platform with four square columns, Part I: Effects of current incidence angle and hull appendages. *Ocean Eng.* 54, 150–169.
- Gonçalves, R.T., Rosetti, G.F., Fajarra, A.L.C., Oliveira, A.C., 2013. Experimental study on vortex-induced motions of a semi-submersible platform with four square columns, Part II: Effects of surface waves, external damping and draft condition. *Ocean Eng.* 62, 10–24.
- Griffith, M.D., Lo Jacono, D., Sheridan, J., Leontini, J.S., 2017. Flow-induced vibration of two cylinders in tandem and staggered arrangements. *J. Fluid Mech.* 833, 98–130.
- Hangan, H., Vickery, B.J., 1999. Buffeting of two-dimensional bluff bodies. *J. Wind Eng. Ind. Aerodyn.* 82, 173–187.
- van Hinsberg, N.P., 2021a. Mean and unsteady loading on square prisms with rounded edges: hard marine growth, incidence, and Reynolds number effects. *Mar. Struct.* 75, 102886–1–20.
- van Hinsberg, N.P., 2021b. Aerodynamics of smooth and rough square-section prisms at incidence in very high Reynolds-number cross-flows. *Exp. Fluids* 62, 1–17.
- van Hinsberg, N.P., Schewe, G., Jacobs, M., 2017. Experiments on the aerodynamic behaviour of square cylinders with rounded corners at Reynolds numbers up to 12 million. *J. Fluids Struct.* 74, 214–233.
- van Hinsberg, N.P., Schewe, G., Jacobs, M., 2018. Experimental investigation on the combined effects of surface roughness and corner radius for square cylinders at high Reynolds numbers up to 10^7 . *J. Wind Eng. Ind. Aerodyn.* 173, 14–27.
- Hosseini, N., Griffith, M.D., Leontini, J.S., 2021. Flow states and transitions in flow past arrays of tandem cylinders. *J. Fluid Mech.* 910, 1–21.
- Hu, J.C., Zhou, Y., Dalton, C., 2006. Effects of corner radius on the near wake of a square prism. *Exp. Fluids* 40, 106–118.
- Huang, K., Chen, X., Kwan, C.T., 2003. The impact of vortex-induced motions on mooring system design for spar-based installations, in: *Proc. OTC*.
- Igarashi, T., 1981. Characteristics of the Flow around Two Circular Cylinders Arranged in Tandem : 1st Report. *Bulletin of the JSME* 24, 323–331.
- Igarashi, T., 1984. Characteristics of the Flow around Two Circular Cylinders Arranged in Tandem : 2nd Report, Unique Phenomenon at Small Spacing. *Bulletin of the JSME* 27, 2380–2387.
- Kareem, A., 1987. The effect of aerodynamic interference on the dynamic response of prismatic structures. *J. Wind Eng. Ind. Aerodyn.* 25, 365–372.
- Kim, M.K., Kim, D.K., Yoon, S.H., Lee, D.H., 2008. Measurements of the flow fields around two square cylinders in a tandem arrangement. *J. Mech. Sci. Tech.* 22, 397–407.
- Li, S., Zhao, W., Wan, D., 2018. Numerical study of column rounded corner effects on vortex-induced motions of semi-submersibles, in: *Proc. 13th ISOPE Conf.*
- Liu, C.H., Chen, J.M., 2002. Observations of hysteresis in flow around two square cylinders in a tandem arrangement. *J. Wind Eng. Ind. Aerodyn.* 90, 1019–1050.
- Liu, M., Xiao, L., Yang, J., Tian, X., 2017. Parametric study on the vortex-induced motions of semi-submersibles: Effect of rounded ratios of the column and pontoon. *Phys. Fluids* 29, 055101–1–18.
- Luo, S.C., 1989. Fluctuating aerodynamic forces acting on a square cylinder that is downstream of an identical one. *Eng. J. Singapore* 16, 14–25.
- Luo, S.C., Li, L.L., Shah, D.A., 1999. Aerodynamic stability of the downstream of two tandem square section cylinders. *J. Wind Eng. Ind. Aerodyn.* 79, 79–103.
- Luo, S.C., Teng, T.C., 1990. Aerodynamic forces on a square section cylinder that is downstream to an identical cylinder. *J. Aeronaut.* 94, 203–212.
- Ma, W., Wu, G., Thompson, H., Prislun, I., Maroju, S., 2013. Vortex induced motions of a column stabilized floater, in: *Proc. DOT Conf.*
- Meneghini, J.R., Saltara, F., Siqueira, C.L.R., Ferrari Jr., J.A., 2001. Numerical simulation of flow interference between two circular cylinders in tandem and side-by-side arrangements. *J. Fluid Struct.* 15, 327–350.
- Moe, G., Henriksen, M.O., 1999. Flow induced vibrations of line-like structures, in: *Proc. 3rd Int. Symp. Cable Dyn.*
- Ohya, Y., Okajima, A., Hayashi, M., 1989. Wake interference and vortex shedding. *Encyclopedia Fluid Mech.* 8, 323–389.
- Okajima, A., 1979. Flows around two tandem circular cylinders at very high Reynolds numbers. *Bulletin of the JSME* 22, 504–511.
- Pearcy, H.H., Cash, R.F., Salter, I.J., Boribond, A., 1982. Interference effects on the drag loading for groups of cylinders in uni-directional flow. Technical Report R130. Nat. Maritime Inst. Rep.
- Pesce, C.P., Alosa do Amaral, G., Mendes, B., Lins de Oliveira, E., Franzini, G.R., 2021. A model to assess the susceptibility of a multicolumn FOWT platform to vortex-induced motions in early design stages, in: *Proc. 40th ASME-OMAE Conf.*

- Polhamus, E.C., 1958. Effect of flow incidence and Reynolds number on low-speed aerodynamic characteristics of several noncircular cylinders with applications to directional stability and spinning. Technical Report 4176. Nat. Adv. Comm. Aero. Technical Note.
- Reinholds, T.A., Tieleman, H.W., Maher, F.J., 1977. Interaction of square prisms in two flow fields. *J. Wind Eng. Ind. Aerodyn.* 2, 223–241.
- Rijken, O., 2014. Examining the effects of scale, mass ratios and column shapes on the vortex induced motion response of a semi-submersible through CFD analysis, in: Proc. 33rd ASME-OMAE Conf., pp. 263–276.
- Rijken, O., Leverette, S., 2009. Field measurements of vortex induced motions of a deep draft semisubmersible, in: Proc. 28th ASME-OMAE Conf. th ASME-OMAE Conf., pp. 739–746.
- Sakamoto, H., Haniu, H., 1988. Effect of free-stream turbulence on characteristics of fluctuating forces acting on two square prisms in tandem arrangement. *J. Fluids Eng.* 110, 140–146.
- Sakamoto, H., Haniu, H., Obata, Y., 1987. Fluctuating forces acting on two square prisms in a tandem arrangement. *J. Wind Eng. Ind. Aerodyn.* 26, 85–103.
- Schewe, G., van Hinsberg, N.P., Jacobs, M., 2021. Investigation of the steady and unsteady forces acting on a pair of circular cylinders in crossflow up to ultra-high Reynolds numbers. *Exp. Fluids* 62, 1–18.
- Schewe, G., Jacobs, M., 2019. Experiments on the flow around two tandem circular cylinders from sub- up to transcritical Reynolds numbers. *J. Fluid Struct.* 88, 148–166.
- Shang, J., Zhou, Q., Alam, M.M., Liao, H., Cao, S., 2019. Numerical studies of the flow structure and aerodynamic forces on two tandem square cylinders with different chamfered-corner ratios. *Phys. Fluids* 31, 075102–1–15.
- Shiraishi, N., Matsumoto, M., Shirato, H., 1986. On aerodynamic instabilities of tandem structures. *J. Wind Eng. Ind. Aerodyn.* 23, 437–447.
- Sohankar, A., 2012. A numerical investigation of the flow over a pair of identical square cylinders in a tandem arrangement. *Int. J. Numer. Methods Fluids* 70, 1244–1257.
- Sohankar, A., 2014. A LES study of the flow interference between tandem square cylinder pairs. *Theor. Comput. Fluid Dyn.* 28, 531–548.
- Sohankar, A., Ertman, A., 2009. Forced-convection heat transfer from tandem square cylinders in cross flow at low Reynolds numbers. *Int. J. Numer. Methods Fluids* 60, 733–751.
- Sumner, D., 2010. Two circular cylinders in cross-flow: a review. *J. Fluid Struct.* 26, 849–899.
- Takeuchi, T., Matsumoto, M., 1992. Aerodynamic response characteristics of rectangular cylinders in tandem arrangement. *J. Wind Eng. Ind. Aerodyn.* 41, 565–576.
- Tamura, T., Miyagi, T., 1999. The effect of turbulence on aerodynamic forces on a square cylinder with various corner shapes. *J. Wind Eng. Ind. Aerodyn.* 83, 135–145.
- Tamura, T., Miyagi, T., Kitagishi, T., 1998. Numerical prediction of unsteady pressures on a square cylinder with various corner shapes. *J. Wind Eng. Ind. Aerodyn.* 74–76, 531–542.
- Tatsutani, K., Devarakonda, R., Humphrey, J.A.C., 1993. Unsteady flow and heat transfer for cylinder pairs in a channel. *Int. J. Heat Mass Transf.* 13, 3311–3328.
- Theophanatos, A., 1988. Marine growth and the hydrodynamic loading of offshore structures. Ph.D. thesis. Strathclyde University, Glasgow, United Kingdom.
- Uffinger, T., Ali, I., Becker, S., 2013. Experimental and numerical investigations of the flow around three different wall-mounted cylinder geometries of finite length. *J. Wind Eng. Ind. Aerodyn.* 119, 13–27.
- Virkam, C.K., Ravindra, H.V., Krishne Gowda, Y.T., 2020. Visualisation of flow past square cylinders with corner modification. *J. Mech. Energy Eng.* 4(44), 285–294.
- Waals, O.J., Phadke, A.C., Bultema, S., 2007. Flow induced motions of multi column floaters, in: Proc. 26th ASME-OMAE Conf., pp. 669–678.
- Wang, L.J., Alam, M.M., Zhou, Y., 2017. Two tandem cylinders of different diameters in crossflow: effect of an upstream cylinder on wake dynamics. *J. Fluid Mech.* 836, 5–42.
- Wu, J., Welch, L.W., Wels, M.C., Sheridan, J., Walker, G.J., 1994. Spanwise wake structures of a circular cylinder and two circular cylinders in tandem. *Exp. Therm. Fluid Sci.* 9, 299–308.
- Xu, G., Zhou, Y., 2004. Strouhal numbers in the wake of two inline cylinders. *Exp. Fluids* 37, 248–256.
- Yen, S.C., San, K.C., Chuang, T.H., 2008. Interactions of tandem square cylinders at low Reynolds numbers. *Exp. Therm. Fluid Sci.* 32, 927–938.
- Zdravkovich, M.M., 1977. Review of flow interference between two circular cylinders in various arrangements. *ASME J. Fluids Eng.* 99, 618–633.
- Zdravkovich, M.M., 1985. Flow induced oscillations of two interfering circular cylinders. *J. Sound Vib.* 101, 511–521.
- Zdravkovich, M.M., 1987. The effects of interference between circular cylinders in cross flow. *J. Fluid Struct.* 1, 239–261.
- Zhang, W., Chen, X., Yang, H., Liang, H., Wei, Y., 2019. Forced convection for flow across two tandem cylinders with rounded corners in a channel. *Int. J. Heat Mass Transf.* 130, 1053–1069.
- Zhou, Y., Yiu, M.W., 2006. Flow structure, momentum and heat transport in a two-tandem-cylinder wake. *J. Fluid Mech.* 548, 17–48.

A. Appendix

Table A1: Aerodynamic coefficients for selected points in the various flow regimes from subcritical to transcritical at three spacing values ($S/D = 2.8, 4.0,$ and 5.6) of two tandem 2D square-section prisms ($r/D = 0.16, k_s/D = 4.5 \times 10^{-4}$) at 0° angle of incidence.

α	S/D	N_θ	Flow regime [†]	Re_D^\ddagger	C_{d1}	C_{d2}	C_{D2}	$\sqrt{(C_D^2)}$	C_{I1}	C_{I2}	C_{L2}	$\sqrt{(C_L^2)}$	C_{m1}	C_{m2}	C_{pb1}	C_{pb2}	St_{L2} (1^{st})	St_{L2} (2^{nd})	
0°	2.8	1	subcritical	1.51×10^5	1.47	0.70	0.59	0.23	0.03	-0.01	0.02	0.37	0.003	-0.001	-1.13	-1.24	0.13	-	
		2	subcritical	2.22×10^5	1.37	-0.02	0.06	0.27	0.08	-0.03	0.02	0.02	0.23	0.005	0.002	-0.99	-0.75	0.12	-
		3	critical	3.59×10^5	1.17	-0.24	0.27	0.06	$\mathcal{O}(10^{-3})$	0.05	-0.03	-0.03	0.16	0.005	-0.004	-0.72	-0.50	0.21	0.12
		4	critical	3.72×10^5	0.78	0.24	0.29	0.06	0.66	-0.41	0.01	0.01	0.13	-0.056	-0.088	-0.68	-0.54	0.24	0.21
		5	supercritical	4.69×10^5	0.25	0.46	0.38	0.04	0.04	-0.03	-0.03	-0.01	0.09	-0.001	0.003	-0.31	-0.65	0.23	-
		6	upper transition	1.118×10^6	0.88	0.56	0.36	0.09	0.09	-0.06	-0.06	-0.01	0.21	-0.001	0.004	-0.78	-0.71	0.21	0.12
		7	upper transition	1.449×10^6	1.06	0.12	0.19	0.15	0.04	-0.02	-0.02	$\mathcal{O}(10^{-3})$	0.18	0.003	0.004	-0.81	-0.63	0.21	0.13
		8	upper transition	1.676×10^6	1.12	0.01	0.13	0.21	0.01	-0.02	-0.02	$\mathcal{O}(10^{-3})$	0.15	0.006	0.001	-0.85	-0.69	0.13	0.21
		9	transcritical	2.227×10^6	1.16	0.41	0.28	0.22	0.02	-0.02	-0.02	$\mathcal{O}(10^{-4})$	0.20	0.006	$\mathcal{O}(10^{-4})$	-0.90	-0.97	0.13	-
		10	transcritical	4.083×10^6	1.18	0.42	0.34	0.22	0.02	-0.02	-0.02	$\mathcal{O}(10^{-4})$	0.25	0.006	0.001	-0.91	-0.99	0.13	-
		11	transcritical	7.055×10^6	1.18	0.30	0.27	0.24	0.02	-0.02	-0.02	$\mathcal{O}(10^{-3})$	0.16	0.006	$\mathcal{O}(10^{-5})$	-0.91	-0.93	0.13	-
4.0	2.8	12	subcritical	1.52×10^5	1.44	0.70	0.66	0.14	0.02	-0.01	-0.02	0.45	0.006	$\mathcal{O}(10^{-4})$	-1.12	-1.03	0.13	-	
		13	critical	3.16×10^5	1.13	0.22	0.41	0.08	0.05	-0.08	-0.02	-0.02	0.22	0.005	0.018	-0.74	-0.64	0.25	0.13
		14	critical	3.69×10^5	0.83	0.55	0.48	0.06	-0.28	-0.02	-0.02	0.01	0.09	0.035	0.042	-0.70	-0.62	0.12	0.27
		15	critical	3.71×10^5	0.66	0.51	0.46	0.06	-0.70	0.13	0.06	0.06	0.17	0.054	0.068	-0.59	-0.57	0.27	-
		16	supercritical	4.65×10^5	0.57	0.50	0.50	0.06	0.05	-0.04	-0.04	-0.01	0.29	-0.001	0.004	-0.67	-0.67	0.25	-
		17	supercritical	1.141×10^6	0.77	0.54	0.51	0.08	0.01	-0.04	-0.04	-0.01	0.34	0.006	0.001	-0.79	-0.76	0.24	-
		18	transcritical	1.931×10^6	1.13	0.61	0.61	0.14	0.03	-0.04	-0.04	$\mathcal{O}(10^{-3})$	0.27	0.004	-0.001	-0.88	-0.90	0.14	0.24
		19	transcritical	4.271×10^6	1.17	0.62	0.63	0.14	0.02	-0.02	-0.02	$\mathcal{O}(10^{-3})$	0.34	0.005	-0.001	-0.91	-0.92	0.14	-
		20	transcritical	7.035×10^6	1.17	0.61	0.63	0.14	0.02	-0.03	-0.03	0.01	0.33	0.005	-0.001	-0.91	-0.93	0.14	-
		5.6	2.8	21	subcritical	1.53×10^5	1.48	0.58	0.62	0.09	0.01	$\mathcal{O}(10^{-4})$	-0.01	0.48	0.006	0.002	-1.15	-0.90	0.14
22	critical			3.05×10^5	1.30	0.50	0.52	0.09	-0.19	-0.01	-0.01	-0.01	0.22	0.030	0.009	-1.01	-0.78	0.14	0.26
23	critical			3.32×10^5	0.95	0.60	0.51	0.06	0.51	-0.19	-0.03	-0.03	0.14	-0.047	-0.009	-0.88	-0.75	0.13	0.27
24	critical			3.74×10^5	0.69	0.58	0.51	0.06	0.21	-0.10	-0.03	-0.03	0.21	-0.005	0.002	-0.81	-0.72	0.26	0.13
25	critical			4.32×10^5	0.51	0.52	0.498	0.04	0.24	-0.08	-0.04	-0.04	0.14	-0.011	0.017	-0.61	-0.62	0.30	0.17
26	supercritical			1.112×10^6	0.77	0.55	0.53	0.07	0.02	-0.04	-0.04	-0.01	0.23	0.006	0.002	-0.83	-0.74	0.25	-
27	supercritical			4.177×10^6	0.81	0.55	0.53	0.07	0.01	-0.03	-0.03	$\mathcal{O}(10^{-3})$	0.24	0.006	0.002	-0.85	-0.76	0.25	-
28	supercritical			7.019×10^6	0.80	0.55	0.53	0.06	$\mathcal{O}(10^{-3})$	-0.02	-0.02	$\mathcal{O}(10^{-3})$	0.27	0.008	0.002	-0.86	-0.77	0.25	-

[†] based on the upstream prism.

[‡] based on the undisturbed free stream velocity.

Table A2: Aerodynamic coefficients for selected points in the various flow regimes from subcritical to supercritical to a single 2D square-section prism ($r/D = 0.16, k_s/D = 4.5 \times 10^{-4}$) at 0° angle of incidence.

α	Re_D	Flow regime	$C_{d, \text{single}}$	$C_{D, \text{single}}$	$\sqrt{(C_D^2)_{\text{single}}}$	$C_{L, \text{single}}$	$\sqrt{(C_L^2)_{\text{single}}}$	$C_{m, \text{single}}$	$C_{ph, \text{single}}$	$\text{St}_{L, \text{single}} (1^{\text{st}})$	$\text{St}_{L, \text{single}} (2^{\text{nd}})$
0°											
1	1.52×10^5	subcritical	1.46	1.43	0.06	0.02	0.53	0.003	-1.16	0.14	-
2	2.21×10^5	subcritical	1.43	1.39	0.07	0.03	0.47	-0.001	-1.12	0.14	-
3	3.65×10^5	critical	1.00	0.95	0.06	-0.13	0.15	0.019	-0.97	0.13	0.28
4	3.65×10^5	critical	1.00	0.95	0.06	-0.13	0.15	0.019	-0.97	0.13	0.28
5	4.65×10^5	supercritical	0.62	0.63	0.06	-0.07	0.12	0.009	-0.77	0.29	-
6	1.116×10^6	supercritical	0.74	0.70	0.07	-0.07	0.15	0.005	-0.85	0.26	-
7	1.384×10^6	supercritical	0.75	0.73	0.07	-0.07	0.16	0.004	-0.91	0.26	-
8	1.678×10^6	supercritical	0.80	0.74	0.07	-0.07	0.18	0.004	-0.92	0.26	-
9	2.231×10^6	supercritical	0.79	0.75	0.07	-0.06	0.17	0.004	-0.88	0.26	-
10	4.168×10^6	supercritical	0.77	0.75	0.07	-0.07	0.15	0.005	-0.86	0.26	-
11	6.942×10^6	supercritical	0.74	0.73	0.07	-0.06	0.15	0.004	-0.85	0.27	-
12	1.52×10^5	subcritical	1.45	1.43	0.06	0.02	0.53	0.003	-1.16	0.14	-
13	3.13×10^5	critical	1.34	1.19	0.06	-0.06	0.27	0.006	-1.02	0.14	0.28
14	3.65×10^5	critical	1.00	0.95	0.06	-0.13	0.15	0.019	-0.97	0.13	0.28
15	3.65×10^5	critical	1.00	0.95	0.06	-0.13	0.15	0.019	-0.97	0.13	0.28
16	4.65×10^5	supercritical	0.62	0.63	0.06	-0.07	0.12	0.009	-0.77	0.29	-
17	1.162×10^6	supercritical	0.75	0.72	0.07	-0.06	0.15	0.005	-0.84	0.26	-
18	1.948×10^6	supercritical	0.79	0.75	0.07	-0.06	0.19	0.004	-0.90	0.26	-
19	4.168×10^6	supercritical	0.77	0.75	0.07	-0.07	0.15	0.005	-0.86	0.26	-
20	6.942×10^6	supercritical	0.74	0.73	0.07	-0.06	0.15	0.004	-0.85	0.27	-
21	1.52×10^5	subcritical	1.45	1.43	0.06	0.02	0.53	0.003	-1.16	0.14	-
22	3.01×10^5	critical	1.37	1.23	0.06	-0.02	0.32	0.003	-1.05	0.14	-
23	3.37×10^5	critical	1.13	0.99	0.05	-0.35	0.17	0.038	-0.95	0.14	0.28
24	3.65×10^5	critical	1.00	0.95	0.06	-0.13	0.15	0.019	-0.97	0.13	0.28
25	4.36×10^5	critical	0.63	0.60	0.06	-0.08	0.11	0.008	-0.75	0.27	-
26	1.116×10^6	supercritical	0.75	0.70	0.07	-0.07	0.15	0.005	-0.85	0.26	-
27	4.168×10^6	supercritical	0.77	0.75	0.07	-0.07	0.15	0.005	-0.86	0.26	-
28	6.942×10^6	supercritical	0.74	0.73	0.07	-0.06	0.15	0.004	-0.85	0.27	-

Table A3: Aerodynamic coefficients for selected points in the various flow regimes from subcritical to transcritical at three spacing values ($S/D = 2.8, 4.0,$ and 5.6) of two tandem 2D square-section prisms ($r/D = 0.16, k_s/D = 4.5 \times 10^{-4}$) at 45° angle of incidence.

α	S/D	\dot{M}	Flow regime [†]	Re_D^{\ddagger}	C_{d1}	C_{d2}	C_{D2}	$\sqrt{(C_D^2)_2}$	C_{l1}	C_{l2}	C_{L2}	$\sqrt{(C_L^2)_2}$	C_{m1}	C_{m2}	$C_{\mu b1}$	$C_{\mu b2}$	$St_{L2} (1^{st})$	$St_{L2} (2^{nd})$	
45°	2.8	A	subcritical	2.25×10^5	1.79	-0.40	-0.38	0.13	0.01	-0.01	$\mathcal{O}(10^{-4})$	0.73	0.001	0.001	-1.15	-0.68	0.11	-	
		B	critical	4.06×10^5	1.86	-0.23	-0.28	0.13	0.09	-0.04	-0.04	$\mathcal{O}(10^{-3})$	0.59	0.001	-0.004	-1.21	-0.70	0.11	-
		C	critical	5.39×10^5	1.42	-0.01	-0.06	0.10	-0.10	0.02	0.02	0.02	0.48	-0.017	0.008	-1.01	-0.69	0.12	-
		D	supercritical	5.78×10^5	1.38	0.03	-0.03	0.11	-0.03	0.02	0.02	$\mathcal{O}(10^{-3})$	0.63	-0.004	0.004	-1.00	-0.72	0.12	-
		E	upper transition	7.89×10^5	1.49	-0.25	-0.20	0.11	-0.06	$\mathcal{O}(10^{-3})$	0.01	$\mathcal{O}(10^{-3})$	0.67	-0.009	0.005	-1.03	-0.67	0.11	-
		F	transcritical	2.133×10^6	1.63	-0.32	-0.31	0.13	-0.01	-0.01	-0.01	$\mathcal{O}(10^{-3})$	0.66	-0.005	-0.001	-1.10	-0.68	0.11	-
		G	transcritical	4.526×10^6	1.67	-0.31	-0.32	0.14	-0.01	-0.01	-0.01	0.01	0.67	-0.004	0.002	-1.12	-0.69	0.11	-
		H	transcritical	6.951×10^6	1.66	-0.33	-0.32	0.12	-0.01	-0.01	-0.01	0.01	0.51	-0.004	0.002	-1.12	-0.69	0.11	-
4.0	4.0	I	subcritical	2.17×10^5	1.64	-0.06	0.04	0.18	0.01	$\mathcal{O}(10^{-3})$	0.01	0.79	$\mathcal{O}(10^{-5})$	0.002	-1.02	-0.71	0.11	-	
		J	critical	4.67×10^5	1.56	-0.06	0.10	0.12	0.06	-0.02	-0.02	$\mathcal{O}(10^{-4})$	0.52	$\mathcal{O}(10^{-5})$	0.001	-0.96	-0.67	0.11	-
		K	supercritical	5.46×10^5	1.47	0.37	0.44	0.27	0.02	$\mathcal{O}(10^{-3})$	0.01	$\mathcal{O}(10^{-3})$	0.29	0.004	$\mathcal{O}(10^{-4})$	-1.07	-0.85	0.12	0.14
		L	upper transition	6.24×10^5	1.92	0.83	0.78	0.21	-0.08	$\mathcal{O}(10^{-3})$	0.01	$\mathcal{O}(10^{-3})$	0.95	-0.015	-0.004	-1.47	-1.22	0.14	-
		M	upper transition	7.61×10^5	1.67	0.43	0.47	0.33	-0.08	-0.01	-0.01	0.01	0.83	-0.014	$\mathcal{O}(10^{-4})$	-1.19	-0.98	0.12	-
		N	transcritical	2.123×10^6	1.51	0.07	0.12	0.18	-0.02	-0.01	-0.01	$\mathcal{O}(10^{-3})$	0.72	-0.005	0.002	-0.98	-0.76	0.11	-
		O	transcritical	4.689×10^6	1.55	0.08	0.12	0.21	0.21	-0.01	-0.01	$\mathcal{O}(10^{-3})$	0.73	-0.004	0.002	-1.00	-0.77	0.11	-
		P	transcritical	6.847×10^6	1.55	0.07	0.13	0.19	0.19	-0.01	-0.01	$\mathcal{O}(10^{-3})$	0.75	-0.004	0.002	-1.01	-0.77	0.11	-
5.6	5.6	Q	subcritical	2.12×10^5	2.41	0.84	0.81	0.19	0.01	$\mathcal{O}(10^{-3})$	0.01	1.06	0.001	-0.001	-1.69	-1.26	0.13	-	
		R	critical	3.78×10^5	2.30	0.79	0.77	0.20	0.13	-0.01	-0.01	$\mathcal{O}(10^{-3})$	0.95	0.008	0.001	-1.66	-1.22	0.13	-
		S	critical	4.53×10^5	2.05	0.83	0.87	0.19	0.06	-0.01	-0.01	$\mathcal{O}(10^{-3})$	1.05	0.007	0.001	-1.48	-1.18	0.14	-
		T	supercritical	5.10×10^5	1.83	0.83	0.91	0.18	-0.01	-0.01	-0.01	$\mathcal{O}(10^{-3})$	0.95	-0.001	0.003	-1.41	-1.12	0.15	-
		U	upper transition	5.46×10^5	2.04	1.00	0.90	0.21	-0.04	-0.02	-0.02	$\mathcal{O}(10^{-4})$	1.05	-0.011	-0.004	-1.61	-1.31	0.14	-
		V	upper transition	6.64×10^5	2.16	1.06	0.95	0.23	-0.09	-0.01	-0.01	-0.01	1.09	-0.013	-0.003	-1.67	-1.38	0.14	-
		W	transcritical	2.116×10^6	2.23	1.07	1.04	0.21	-0.01	-0.01	-0.01	$\mathcal{O}(10^{-3})$	1.09	-0.005	-0.002	-1.65	-1.39	0.14	-
		X	transcritical	4.628×10^6	2.27	1.10	1.04	0.22	-0.02	$\mathcal{O}(10^{-3})$	0.01	$\mathcal{O}(10^{-3})$	1.05	-0.005	-0.001	-1.67	-1.43	0.14	-
Y	transcritical	5.817×10^6	2.25	1.10	1.04	0.21	-0.01	-0.01	-0.01	$\mathcal{O}(10^{-3})$	0.98	-0.004	-0.001	-1.66	-1.42	0.14	-		

[†] based on the upstream prism.

[‡] based on the undisturbed free stream velocity.

Table A4: Aerodynamic coefficients for selected points in the various flow regimes from subcritical to transcritical of a single 2D square-section prism ($r/D = 0.16$, $k_s/D = 4.5 \times 10^{-4}$) at 45° angle of incidence.

α	N $^\circ$	Flow regime	Re_D	$C_{d, single}$	$C_{D, single}$	$\sqrt{(C_D^2)_{single}}$	$C_{L, single}$	$C_{L, single}$	$\sqrt{(C_L^2)_{single}}$	$C_{m, single}$	$C_{pb, single}$	$St_{L, single} (1^{st})$	$St_{L, single} (2^{nd})$
45°	A	subcritical	2.22×10^5	2.37	2.39	0.24	$\mathcal{O}(10^{-3})$	$\mathcal{O}(10^{-3})$	0.62	-0.001	-1.70	0.13	-
	B	critical	4.07×10^5	2.27	2.28	0.18	0.03	-0.01	0.61	-0.004	-1.66	0.14	-
	C	critical	5.37×10^5	1.76	1.77	0.12	0.05	0.01	0.37	-0.007	-1.39	0.16	-
	D	upper transition	5.72×10^5	1.90	1.88	0.17	-0.02	-0.02	0.59	0.002	-1.55	0.15	-
	E	upper transition	7.96×10^5	2.16	2.15	0.19	$\mathcal{O}(10^{-3})$	-0.03	0.69	-0.001	-1.68	0.14	-
	F	transcritical	2.180×10^6	2.20	2.20	0.19	0.01	-0.01	0.61	0.001	-1.66	0.14	-
	G	transcritical	4.511×10^6	2.22	2.25	0.19	$\mathcal{O}(10^{-3})$	$\mathcal{O}(10^{-4})$	0.63	0.001	-1.67	0.14	-
	H	transcritical	5.546×10^6	2.20	2.22	0.20	$\mathcal{O}(10^{-4})$	$\mathcal{O}(10^{-5})$	0.54	$\mathcal{O}(10^{-4})$	-1.65	0.14	-
	I	subcritical	2.22×10^5	2.37	2.39	0.24	$\mathcal{O}(10^{-3})$	$\mathcal{O}(10^{-3})$	0.62	-0.001	-1.70	0.13	-
	J	critical	4.68×10^5	2.03	2.02	0.14	0.05	0.03	0.45	-0.007	-1.50	0.14	-
	K	critical	5.48×10^5	1.80	1.81	0.15	0.01	$\mathcal{O}(10^{-3})$	0.46	-0.001	-1.43	0.15	-
	L	upper transition	6.27×10^5	2.01	2.00	0.17	-0.01	-0.03	0.63	$\mathcal{O}(10^{-5})$	-1.61	0.14	-
	M	upper transition	7.40×10^5	2.10	2.11	0.19	0.02	-0.03	0.63	0.001	-1.65	0.14	-
	N	transcritical	2.180×10^6	2.20	2.20	0.19	0.01	-0.01	0.61	0.001	-1.66	0.14	-
	O	transcritical	4.705×10^6	2.21	2.23	0.20	$\mathcal{O}(10^{-3})$	$\mathcal{O}(10^{-3})$	0.57	$\mathcal{O}(10^{-5})$	-1.66	0.14	-
	P	transcritical	5.546×10^6	2.20	2.22	0.20	$\mathcal{O}(10^{-4})$	$\mathcal{O}(10^{-5})$	0.54	$\mathcal{O}(10^{-4})$	-1.65	0.14	-
	Q	subcritical	2.09×10^5	2.29	2.36	0.25	0.01	$\mathcal{O}(10^{-3})$	0.62	-0.002	-1.63	0.13	-
	R	critical	3.78×10^5	2.31	2.33	0.21	0.02	-0.02	0.70	-0.003	-1.67	0.13	-
	S	critical	4.57×10^5	2.09	2.09	0.14	0.04	0.02	0.51	-0.006	-1.55	0.14	-
	T	critical	5.07×10^5	1.83	1.83	0.12	0.07	0.05	0.35	-0.011	-1.38	0.15	-
	U	critical	5.48×10^5	1.80	1.81	0.15	0.01	$\mathcal{O}(10^{-3})$	0.46	-0.001	-1.43	0.15	-
	V	upper transition	6.83×10^5	2.06	2.04	0.18	$\mathcal{O}(10^{-4})$	-0.03	0.59	$\mathcal{O}(10^{-4})$	-1.63	0.14	-
	W	transcritical	2.180×10^6	2.20	2.20	0.19	0.01	-0.01	0.61	0.001	-1.66	0.14	-
	X	transcritical	4.705×10^6	2.21	2.23	0.20	$\mathcal{O}(10^{-3})$	$\mathcal{O}(10^{-3})$	0.57	$\mathcal{O}(10^{-5})$	-1.66	0.14	-
Y	transcritical	5.546×10^6	2.20	2.22	0.20	$\mathcal{O}(10^{-4})$	$\mathcal{O}(10^{-5})$	0.54	$\mathcal{O}(10^{-4})$	-1.65	0.14	-	